POLITECNICO DI MILANO

Facoltà di Ingegneria dei Sistemi

Corso di Laurea in Ingegneria Fisica

PHOTONIC BANDS OF DISPERSIVE PERIODIC STRUCTURES: NUMERICAL IMPLEMENTATION OF AUXILIARY FIELD FORMULATION

Relatore Interno: **Prof. Gianluca Valentini**
Relatore Esterno: **Prof. Min Qiu**
Correlatore: **Prof. Min Yan**

Tesi di Laurea di

Andrea FERRARIO

Matr. n° 733279

Anno Accademico 2009/2010

Contents

List of Figures and Graphs

Abstract

Electromagnetic metamaterials are artificial structures, often periodic, that interact in peculiar ways with the electromagnetic radiation. The investigation of these materials often need to be carried on numerically due to complex geometries involved. A determination of the electromagnetic properties of such metamaterials requires the knowledge of their band structure. A number of methods, including the Finite-Difference Time-Domain (FDTD) method, have been developed in the past years to this purpose. However, a frequency-domain simulation of metamaterials is still a challenging task due to the metallic dispersive components. In this work, starting from the recently proposed auxiliary fields formulation, we develope two numerical methods, based respectively on the Finite-Difference Method (FDM) and the Finite-Element Method (FEM), for computing eigenfrequencies and eigenmodes of periodic structures containing metallic components described by the Drude model. This work spans all the stages of the numerical implementation, from the analytical formulation of the lossless Drude problem, through the numerical discretization using FDM or FEM, to the matrix computation techniques such as eigensolvers and preconditioning. Finally, we apply the methods developed to benchmark structures to determine their performances; the results are compared to those obtained with other numerical methods. It is found that the FDM approach tends to introduce strongly localized "fictitious" surface modes that affect the physical modes and pollute the band diagram. The FEM implementation does not present this issue. Both methods can compute a number of eigenmodes limited by the numerical resolution; the higher order surface modes always suffer from a numerical error owing to the limited spatial discretization and the element shape. The high order SPP modes populate a frequency range above the expected frequency, and we determined that this issue cannot be solved by increasing the resolution. We expect the FEM implementation of the formulation can be a versatile tool for the design and investigation of periodic structures containing metallic components with any complex geometry.

Abstract in Lingua Italiana

I Metamateriali Elettromagnetici sono strutture artificiali, spesso periodiche, che interagiscono con la radiazione elettromagnetica in modo peculiare. Lo studio di questi materiali deve essere effettuato per via numerica a causa della complessità delle geometrie in questione. Al fine di determinare le proprietà elettromagnetiche di questi materiali è necessaria la conoscenza della loro struttura a bande fotoniche; tuttavia, la simulazione nel dominio delle frequenze di tali materiali è tuttora complicata a causa dei componenti dispersivi che contengono. Nel presente lavoro, utilizzando la formulazione con campi ausiliari, vengono sviluppati due metodi numerici, basati rispettivamente sui Metodi delle Differenze Finite (FDM) e degli Elementi Finiti (FEM), in grado di calcolare le autofrequenze ed i modi del campo elettromagnetico di strutture periodiche contenenti metalli descritti dal modello di Drude. Nel corso di questo lavoro vengono seguite tutte le fasi dell'implementazione numerica, a partire dalla formulazione analitica del problema per il modello di Drude senza perdite, attraverso la discretizzazione usando FDM ed FEM, fino alla scelta degli algoritmi per il computo degli autovalori e per il precondizionamento. Infine, i metodi sviluppati vengono applicati a strutture di prova per determinarne le potenzialità ed i risultati sono confrontati con quelli ottenuti mediante altri metodi numerici. Dalla nostra analisi è emerso che l'approccio con FDM tende ad introdurre dei modi "fittizi" fortemente localizzati che influenzano i modi fisici ed alterano il diagramma a bande. Questo problema non è presente con l'implementazione FEM. Ambedue i metodi sono in grado di calcolare un numero di autofrequenze limitato dalla risoluzione numerica; i modi superficiali di ordine superiore sono affetti da errori dipendenti dalla discretizzazione spaziale e dalla forma degli elementi. Dalle nostre simulazioni abbiamo concluso che questo problema non può essere eliminato solo aumentando la risoluzione. In conclusione, l'implementazione FEM può essere uno strumento versatile per la progettazione e lo studio di strutture metalliche periodiche con geometrie complesse.

Estratto della Tesi

Introduzione

Il presente lavoro di tesi è stato svolto presso l'Istituto Reale di Tecnologia (Kungliga Tekniska Högskolan), Stoccolma, Svezia, in collaborazione con il gruppo di Nanofotonica diretto dal prof. Min Qiu, sotto la supervisione del prof. Min Yan. Il relatore interno al Politecnico di Milano è il prof. Gianluca Valentini. Nel corso dello svolgimento della tesi, alcuni risultati sono stati raccolti in un articolo (allegato in Appendice A), che è stato inviato alla rivista Physical Review B ed è in corso di revisione. Il lavoro svolto consiste nell'implementazione di un metodo numerico in grado di calcolare le autofrequenze (frequenze di risonanza) e i modi di vibrazione del campo elettromagnetico per una struttura periodica contenente componenti metallici. L'applicazione naturale per un metodo con queste caratteristiche è la simulazione e lo studio di metamateriali elettromagnetici, ossia strutture artificiali che interagiscono in modo non comune con la radiazione elettromagnetica. Lo studio dei metamateriali è iniziato nei tardi anni '80 con le prime proposte teoriche, e questo ramo della fotonica è cresciuto grandemente nel corso dei decenni successivi. Le motivazioni di questa crescita sono molteplici: in primo luogo, le peculiari proprietà elettromagnetiche (ad es. rifrazione negativa, guide d'onda nanoscopiche) hanno suscitato un grande interesse dal punto di vista delle applicazioni; in secondo luogo, l'avanzamento delle tecniche di fabbricazione, sia motivato dalla ricerca in sè, sia ereditato dall'industria dei semiconduttori, ha permesso la realizzazione sperimentale dei metamateriali; infine, le capacità computazionali ed il potere di calcolo sono cresciuti esponenzialmente, permettendo di progettare ed analizzare queste strutture.

L'analisi, la progettazione e lo studio di questi materiali devono essere molto spesso condotte per via numerica, in quanto le equazioni che ne descrivono la fisica (le equazioni di Maxwell prime tra tutte) non sono risolubili analiticamente se non per casi molto semplici. Tra i metodi sviluppati nel corso degli anni per questo scopo, citiamo il metodo delle differenze finite nel dominio del tempo (FDTD), il metodo dell'espansione in onde piane (PWE) ed il metodo della matrice di trasferimento. Mentre per strutture costituite da soli materiali dielettrici

sono presenti applicativi che ne permettono la simulazione in modo efficace (ad esempio, il pacchetto MPB - MIT Photonic Bands), per strutture contententi componenti metalliche la soluzione numerica nel dominio delle frequenze è tuttora complicata. I metamateriali progettati sinora sono in effetti strutture periodiche contenenti parti metalliche, e persiste un'ambiguità sul fatto che le proprietà elettromagnetiche macroscopiche siano dovute alle componenti metalliche (che forniscono accoppiamenti capacitivi ed induttivi), alla periodicità spaziale, o alla combinazione delle due.

Lo scopo del nostro lavoro è stato di implementare numericamente una formulazione teorica recentemente presentata, la formulazione con campi ausiliari, al fine di simulare strutture periodiche contenenti componenti metalliche descritte dal modello di Drude senza perdite. In primo luogo, abbiamo ricavato analiticamente le equazioni per il caso in questione, dopodichè le abbiamo discretizzate utilizzando separatamente due approcci, il Metodo delle Differenze Finite (FDM) ed il Metodo degli Elementi Finiti (FEM). Successivamente, al fine di determinare la migliore soluzione per il computo degli autovalori, abbiamo analizzato due algoritmi per questo scopo ed una tecnica di precondizionamento. Infine, abbiamo applicato i metodi sviluppati a strutture di prova e confrontato i risultati con quelli ottenuti mediante altri metodi numerici.

Nel presente Estratto sono individuati i punti salienti del nostro lavoro; in ogni sezione è proposto un riassunto in lingua italiana del contenuto del capitolo corrispondente.

Metamateriali (Cap. 2)

I Metamateriali Elettromagnetici sono una classe di materiali artificialmente realizzati allo scopo di interagire in modo particolare con la radiazione elettromagnetica. Essi sono struttrure in cui almeno una delle dimensioni caratteristiche è comparabile o inferiore alla lunghezza d'onda della radiazione interagente. Questa definizione è strettamente collegata con le proprietà di scalatura delle equazioni di Maxwell; a causa di ciò, ad esempio, un metamateriale funzionante con le microonde si comporta da oggetto macroscopico per la radiazione visibile. La definizione fornita è abbastanza ampia e pertanto comprende svariate classi di metamateriali. In seguito presenteremo alcune di esse, di particolare rilevanza per il nostro lavoro in quanto sono quelle che è possibile simulare con il nostro metodo.

I *Cristalli Fotonici* (PC) sono metamateriali in cui la periodicità spaziale influenza le relazioni di dispersione del campo elettromagnetico creando una struttura a bande fotoniche. Tra le caratteristiche di questi sistemi, la più importante è probabilmente la possibilità di ottenere un band gap fotonico, ossia una banda di frequenze la cui propagazione all'interno del metamateriale è proibita. Le proprietà ottiche di un PC monodimensionale (che consiste in una serie di strati di dielettrico) sono state investigate per oltre cent'anni, iniziando con Lord Rayleigh.

In effetti, lo studio di sistemi ottici di uso comune, come gli specchi dielettrici, può essere condotto con la teoria dei cristalli fotonici, arrivando, ad esempio, alla conclusione che l'alta riflettività di uno specchio dielettrico ad una certa frequenza è dovuta alla presenza di un band gap fotonico. L'interesse per PC bi- e tridimensionali, invece, è molto più recente, ed è iniziato nei tardi anni '80 con i lavori di Yablonovic e John. Tra le applicazioni dei PC citiamo i dispositivi fotonici, guide d'onda, risonatori, laser, filtri ottici per telecomunicazioni, fibre ottiche, rifrazione negativa, ed altre.

I *Materiali Left-Hand* sono particolari metamateriali realizzati in modo da avere sia la permettività dielettrica ϵ sia la permeabilità magnetica μ inferiori a zero per una frequenza o una banda di frequenze, una caratteristica non esistente in natura. La teoria di materiali con ϵ e μ negativi è stata sviluppata da Veselago fin dal 1967. Egli dimostrò come le equazioni di Maxwell abbiano le soluzioni convenzionali, ma con l'importante eccezione che nel computo dell'indice di rifrazione con la formula $n = \sqrt{\epsilon\mu}$ si deve considerare il valore negativo della radice quadrata. Come conseguenza di ciò i materiali con questa caratteristica presentano a tutti gli effetti una rifrazione negativa. Veselago propose il nome (in uso tuttora) di materiali *Left-Handed*, in quanto, a differenza di quanto avviene normalmente, i vettori $\boldsymbol{E}$, $\boldsymbol{H}$ e $\boldsymbol{k}$ (vettore d'onda) formano una terna sinistrorsa. In questi materiali, la velocità di fase (diretta come $\boldsymbol{k}$) ed il flusso di potenza (ossia il vettore di Poynting) sono antiparalleli, ed il comportamento della radiazione elettromagnetica in essi è in un certo senso "invertito".

Teoria (Cap. 3)

In questa sezione deriveremo il problema differenziale centrale al presente lavoro. Si consideri l'equazione del moto per un elettrone secondo il modello di Lorentz:

$$\ddot{\boldsymbol{x}} + \gamma\dot{\boldsymbol{x}} + \omega_0^2\boldsymbol{x} = \frac{e}{m}\boldsymbol{E}, \tag{1}$$

in cui $\boldsymbol{x}$ è la posizione dell'elettrone, e la carica, m la massa, $\boldsymbol{E}$ è il campo elettrico, ω_0 è una pulsazione caratteristica del materiale, e γ è un termine di smorzamento. Detta n_e la densità elettronica, è possibile definire il vettore polarizzazione come $\boldsymbol{P} = en\boldsymbol{x}$. Sostituendo nell'equazione precedente, si ottiene l'equazione differenziale che governa l'andamento di $\boldsymbol{P}$ per il modello di Lorentz,

$$\ddot{\boldsymbol{P}} + \gamma\dot{\boldsymbol{P}} + \omega_0^2\boldsymbol{P} = \omega_p^2\epsilon_0\boldsymbol{E}, \tag{2}$$

da cui è possibile ricavare la permittività dielettrica relativa del modello di Lorentz:

$$\epsilon(\omega) = 1 + \frac{\omega_p^2}{\omega_0^2 - \omega^2 - \gamma i\omega}, \tag{3}$$

dove $\omega_p^2 = \frac{e^2 n}{\epsilon_0 m}$ è la frequenza di plasma elettronica, che dipende dalle caratteristiche del materiale. Si noti che da questo modello è possibile ricavare il modello di Drude prendendo il limite $\omega_0 \to 0$.

Si considerino ora le equazioni di Maxwell in assenza di correnti e cariche libere, per un mezzo non magnetico ($\mu = 1$),

$$\begin{aligned} \nabla \times \boldsymbol{E} &= \mu_0 \frac{\partial \boldsymbol{H}}{\partial t}, \\ \nabla \times \boldsymbol{H} &= \frac{\partial \boldsymbol{D}}{\partial t}, \\ \nabla \cdot \boldsymbol{D} &= 0, \\ \nabla \cdot \boldsymbol{B} &= 0. \end{aligned} \tag{4}$$

Ricordando le relazioni costitutive

$$\boldsymbol{D} = \epsilon_0 \boldsymbol{E} + \boldsymbol{P}, \boldsymbol{B} = \mu_0 \mu \boldsymbol{H}, \tag{5}$$

ed ipotizzando un andamento temporale del tipo $\exp(-i\omega t)$, in unione con l'Eq. (2), il sistema può essere scritto come un problema agli autovalori. In forma matriciale esso è:

$$\omega \begin{bmatrix} \boldsymbol{H} \\ \boldsymbol{E} \\ \boldsymbol{P} \\ \boldsymbol{V} \end{bmatrix} = \begin{bmatrix} 0 & \frac{i}{\mu_0}\nabla\times & 0 & 0 \\ -\frac{i}{\epsilon_0}\nabla\times & 0 & 0 & \frac{i}{\epsilon_0} \\ 0 & 0 & 0 & -i \\ 0 & -i\omega_p^2 & i\omega_0^2 & i\gamma \end{bmatrix} \begin{bmatrix} \boldsymbol{H} \\ \boldsymbol{E} \\ \boldsymbol{P} \\ \boldsymbol{V} \end{bmatrix}. \tag{6}$$

Gli autovalori sono le autofrequenze del sistema, mentre le autofunzioni sono i modi di vibrazione del campo elettromagnetico per la struttura. Dal problema generale (modello di Lorentz con perdite) è possibile ottenere il caso particolare di nostro interesse (modello di Drude senza perdite) imponendo $\gamma = 0$ ed $\omega_0 \to 0$:

$$\omega^2 \boldsymbol{E} = \frac{1}{\epsilon_0} \nabla \times \frac{1}{\mu_0} \nabla \times \boldsymbol{E} + \omega_p^2 \boldsymbol{E}. \tag{7}$$

Eq. (7) è il problema differenziale centrale al presente lavoro. Si noti che esso è stato ottenuto solo da due delle quattro equazioni di Maxwell. Per ottenere i modi di campo fisici, è necessario che le soluzioni obbediscano anche alla condizione di divergenza nulla:

$$\begin{aligned} \nabla \cdot \boldsymbol{H} &= 0, \\ \nabla \cdot (\epsilon_0 \boldsymbol{E} + \boldsymbol{P}) &= 0. \end{aligned} \tag{8}$$

Metodi Numerici (Cap. 4)

La discretizzazione del problema differenziale in Eq. (7) è stata compiuta utilizzando separatamente due approcci, descritti di seguito.

Il *Metodo delle Differenze Finite* (FDM) consiste nel sostituire alle derivate spaziali dei rapporti incrementali su una lunghezza finita, detta *lunghezza di discretizzazione*. Il problema viene trasformato quindi in un problema agli autovalori per una matrice, risolvibile con metodi computazionali. Nel limite $h \to 0$ gli autovalori della matrice tendono agli autovalori del problema differenziale. Per la discretizzazione spaziale è stata usata la griglia di Yee, molto comune nell'ambito delle simulazioni elettromagnetiche, in cui ogni componente dei vettori $\boldsymbol{E}$ ed $\boldsymbol{H}$ è valutata in punti diversi della cella unitaria, per facilitare il computo dell'operazione di rotore discretizzata. La cella unitaria per la griglia di Yee è presentata in Figura 4.1. Per l'imposizione delle condizioni al contorno abbiamo utilizzato una matrice di riduzione, che rimuove i gradi di libertà superflui (nel caso di condizione Conduttore Perfetto) o che stabilisce le corrette relazioni di fase (nel caso di condizione Periodica).

Il *Metodo degli Elementi Finiti* (FEM), secondo Galerkin, consiste nell'identificare un sottospazio finito-dimensionale V^h dello spazio delle soluzioni e trovare la funzione appartenente ad esso che minimizzi la distanza dalla soluzione vera. Ciò è equivalente a richiedere che il residuo tra la soluzione approssimata e la soluzione vera sia ortogonale a V^h. La base di V^h dev'essere scelta in modo opportuno. La nostra scelta è caduta sugli *Edge Elements* su una griglia triangolare (per problemi 2D) o tetraedrica (3D), che offrono alcuni vantaggi: ogni grado di libertà corrisponde al valore della componente del campo elettrico tangenziale ad un lato di un triangolo od un tetraedro, i modi divergenti (che non rispettano la condizione di divergenza nulla) sono confinati alla frequenza $\omega = 0$, l'imposizione delle condizioni al bordo e alle interfacce metallo-dielettrico è immediata e naturale.

Algoritmi (Cap. 5)

In questo capitolo sono stati analizzati due algoritmi per il computo degli autovalori. Il primo, `ARPACK`, è basato sul metodo di Arnoldi, o metodo delle potenze. Questo algoritmo è stato usato estensivamente nell'implementazione fornita da `MATLAB`, che tuttavia non può essere impiegata per problemi di grandi dimensioni, come ad esempio simulazioni tridimensionali. Il secondo, `LOBPCG` (*Localized Optimal Block Preconditioned Conjugate Gradient*) è basato su una minimizzazione via gradiente coniugato del quoziente di Rayleigh per il problema in questione, e di conseguenza può essere utilizzato solo per problemi Hermitiani. Quest'ultimo algoritmo richiede una matrice che discretizzi la condizione di divergenza nulla per le autofunzioni, in modo da poter calcolare unicamente i modi di vibrazione fisici del sistema. possibile inoltre fornire un precondizionatore, al fine di velocizzare la convergenza dell'algoritmo. Per il precondizionamento abbiamo utilizzato l'algoritmo `FSPAI` (*Factorized Sparse Approximated Inverse*), che è ben adatto al problema.

Simulazioni e Risultati (Cap. 6)

In questo capitolo vengono presentati i risultati di simulazioni condotte con le implementazioni FDM e FEM. Abbiamo applicato i metodi numerici a strutture comuni, al fine di confrontarne i risultati con quelli ottenuti con altri metodi numerici. Il FDM funziona correttamente nel caso particolare di strutture contenenti solo mezzi dielettrici (Fig. 6.1), ma è soggetto ad un problema critico nel caso di strutture metalliche. Dai nostri risultati è emerso come questa implementazione tenda ad introdurre modi "fittizi", fortemente localizzati alle interfacce tra metallo e dielettrico (Fig. 6.5c-d) che influenzano i modi fisici, inquinando di conseguenza il diagramma a bande.

L'implementazione FEM non presenta questo problema, ed è in grado di replicare correttamente (ed in un caso, con maggiore precisione, si veda Fig. 6.7) i risultati ottenuti con altri metodi numerici. Abbiamo applicato il metodo anche a problemi tridimensionali, prima ad un sistema di soli dielettrici (Fig. 6.8) e successivamente calcolando i modi propagantisi lungo una catena di sfere metalliche (Fig. 6.9. Il nostro metodo è stato in grado di simulare correttamente sia l'eccitazione dipolare, sia quelle di ordine superiore (Fig. 6.10).

Ambedue le formulazioni calcolano tutti i modi di vibrazione compatibili con la risoluzione spaziale scelta, ma i modi di ordine superiore sono soggetti ad un consistente errore numerico e popolano una banda di frequenze superiore alla frequenza teorica. Ulteriori simulazioni (Figg. 6.11 - 6.12) hanno evidenziato come questo errore sia dipendende in effetti dalla discretizzazione dello spazio e dalla forma degli elementi, ma anche come il problema non possa essere completamente risolto semplicemente incrementando la risoluzione, in quanto nuovi modi di ordine ancora più alto sono introdotti come conseguenza della ridotta lunghezza di discretizzazione.

Conclusioni (Cap. 7)

Le conclusioni tratte da questo lavoro sono le seguenti. La formulazione a Differenze Finite è soggetta al problema critico dei modi fittizi, e pertanto non può essere usata in modo efficace. La formulazione a Elementi Finiti non è soggetta a questo problema. Entrambe le formulazioni sono affette dal problema degli errori numerici sui modi di ordine superiore, esposto nella precedente sezione, tuttavia, la formulazione FEM ha riprodotto con successo i risultati degli altri metodi numerici, e pertanto può essere uno strumento versatile per la simulazione di strutture metalliche periodiche anche aventi geometrie complicate.

Acknowledgments - Ringraziamenti

Il primo ringraziamento va a mio nonno, Carlo Ferrario, alla cui memoria questo lavoro è dedicato, per avermi sempre supportato e accompagnato nel mio percorso di studi. Voglio ringraziare i miei genitori Claudio e Luisella per essermi sempre stati vicini ed avermi permesso di arrivare qui. Inoltre ringrazio il mio saggio fratello Lorenzo perché è lui. And, thanks to Sofia for helping me finish this work by "poking" me all the time (and for the nice pictures in this thesis!). E tutti gli altri: nonni, zii, sii, i vecchi amici in Italia, i nuovi amici in Svezia, i colleghi ingegneri, ecc.

I would like to thank Prof. Min Qiu and the KTH Nanophotonics group for their hospitality and support, and in particular Prof. Min Yan for his assistance in these months. Ringrazio il Prof. Gianluca Valentini per la disponibilità a ricoprire il ruolo di relatore interno al Politecnico.

A Carlo Ferrario

Chapter 1

Introduction

1.1 Background and Motivation

Electromagnetic metamaterials, a class of artificial materials that interact in a peculiar way with the electromagnetic radiation, have in the past twenty years become one of the prominent branches of Photonics. The reason behind this fast growth is threefold: first, such materials are capable of controlling electromagnetic fields in peculiar ways (e.g. subwavelength wave-guiding, negative refraction); second, advances in fabrication techniques, through self-assembly or inherited from the semiconductor industry, made possible the experimental realization of the metamaterials; third, refinements in numerical techniques and the exponential increase of computational power allows us to design and model these structures.

The design or understanding the properties of metamaterials is not an easy task; the underlying equations cannot be solved analytically except for very simple cases, and a numerical approach is required most of the times. The problem of discretizing and solving numerically Maxwell's Equations has been deeply investigated in the last fifty years. As new structures are proposed and designed, however, new challenges arise for the field of computational electromagnetics, such as the requirement of modeling loss or gain and the necessity of considering temporal and spatial dispersion, etc. A number of numerical methods have been developed for this purpose, such as the Finite-Difference Time-Domain method (FDTD), the Plane Wave Expansion method (PWE), the Transfer Matrix methods, and many more. For all-dielectric periodic systems numerical tools such as the MPB software exist that allow an efficient computation of the eigenfrequencies. However the simulation of periodic structures containing metallic components is still a challenging task. Many of the metamaterials designed and realized so far consist in periodic metallic structures; ambiguities persist on to what extent their macroscopic properties are

due to the metallic components (that provide, for instance, inductive couplings), or to the spatial periodicity, or a combination of both. Therefore, to correctly investigate the characteristics of these structures, a reliable numerical method is needed that can both simulate the capacitive and inductive behaviors of metallic components, and the effect of the spatial periodicity.

1.2 Outline

In this work, we present the development of a new numerical method capable of computing the photonic and structure and the eigenmodes of a periodic structure containing media whose permittivities obey the Drude or Drude-Lorentz model. We start from a recently proposed formulation of the problem, that combines Maxwell's equations and the electron dynamics into a linear eigenvalue problem. We analytically derive the equations for a lossless metal described by the Drude model and successively discretize the differential problem using, separately, a Finite-Difference Method and a Finite-Element Method. We then investigate the properties of the available eigensolver algorithms and preconditioning techniques to determine an efficient way of solving the discretized matrix problem. Finally, with the developed tools, we simulate the band diagrams of some benchmark structures in order to test the performances and characteristics of the methods.

A general introduction on electromagnetic metamaterials can be found in Chapter 2, together with a comprehensive list of references encompassing most areas of the field. Chapter 3 presents the basic theoretical concepts, and contains as well the derivation of the differential problem central to this work. The numerical methods used in the discretization of the problem are the topic of Chapter 4, while Chapter 5 presents the two eigensolver algorithms and the preconditioning technique that we used in the computation. These chapters contain all the building blocks needed for the realization of the numerical methods. Chapter 6 presents the results (photonic band diagrams and field plots) of the simulations carried on some test structures, followed by a discussion of the strengths and weaknesses of these methods. Finally, Chapter 7 collects our conclusions on this work and our judgment of this formulation.

During the course of this work, some of the most important results have been collected in a paper, presented in Appendix A, that has been submitted to the journal Physical Review B, and is currently under review.

Chapter 2

Metamaterials

2.1 Introduction

Electromagnetic metamaterials are defined as artificially structured media whose features have characteristic lengths comparable or smaller than the wavelength of the electromagnetic radiation interacting with them. This definition is quite broad, encompassing different classes of structures, and is also strictly related to the scaling properties of Maxwell's equations, as exposed in Sect. 3.2.1. Because of it, the electromagnetic properties of structures change dramatically according to the spectral range of the interacting radiation. For example, metamaterials at microwave radiation (with wavelength of tens of millimeters) are macroscopic objects at optical frequencies.

Metamaterials can have surprising features not found in normal (homogeneous) materials. As an example, we present one of the most intriguing properties that can be attained by optical metamaterials: the *Negative Refraction*, discussed later. Another suggestive application is to realize with metamaterials the structures designed with the mathematical tools of Transformation Optics [1]. Devices such as invisibility cloaks have been theoretically predicted, and recently realized, at microwaves [2] and optical [3] frequencies. A third application for metamaterials is the fabrication of enhanced absorbers [4], to be used in solar cells and detectors. In the following sections, we present some classes of metamaterials that have been theoretically and experimentally studied in the past decades and are particularly relevant to this work, being examples of the structures that can be simulated with the methods we developed.

2.2 Photonic Crystals

Photonic Crystals (PC) are structured materials in which the spatial periodicity dramatically affects the propagation of the electromagnetic radiation [5]. The presence of a periodic dielectric function creates a *photonic band structure* for the material, with peculiar dispersion relations.

The optical properties of one-dimensional PCs (a stack of dielectric layers with thickness comparable to the wavelength) have been investigated for over a hundred years, starting with Lord Rayleigh [6]. By changing the layer size, one can increase or decrease the reflectivity of the structure, forbidding or enhancing the propagation at a certain wavelength. The classical explanation given for this phenomenon relies on an analysis of the interference of plane waves reflected and transmitted from the planar interface, but this can also be regarded as a particular case of the theory of periodic dielectric media: a dielectric mirror can be considered as a 1D photonic crystal exhibiting a band gap in a certain range of frequencies, that forbids the propagation (and thus enhances reflection).

The investigation of the properties of structures with 2D or 3D spatial periodicity began in the late '80, after the works of Yablonovitch [7] and John [8], and grew exponentially in the past two decades. The interest in this kind of metamaterial is motivated by their many applications in advanced optical and optoelectronic technologies. In the following subsection we present some examples.

2.2.1 Photonic Crystal Devices

With a suitable engineering of the periodic structure, many kinds of optical devices can be realized with PCs. The efforts in the past years have been particularly directed towards devices on *Photonic Crystal Slabs* [9], two-dimensional periodic structures with a finite thickness that rely on index guiding in order to confine the light in the non-periodic direction [10]. This approach has been preferred over full three-dimensional periodic crystals because of the easier fabrication process, that in many cases can benefit from the decennal experience of the semiconductor industry.

The introduction of localized defects in the otherwise perfect periodic structure creates localized states for the electromagnetic field. High-Q resonators or cavities [11] can be obtained on the slab in this way, and can be used in all-optical chips [12], lasers [13], or filters [14].

Linear defects behaves as waveguides, carrying the light in the slab [15]. These waveguides present surprising features, such as near-zero reflections and losses in presence of to sharp bends [16] and near-zero group velocity at the band edge [17]. Coupling linear defects (waveguides) with localized defects (cavities), more complex structures can be realized, such as optical channel-drop filters [18, 19], to be used in the area of optical telecommunications.

2.2.2 Photonic Crystal Fibers

A concept dual to Photonic Crystal Slabs is at the basis of the technology of Photonic Crystal Fibers [20, 21], in which the light propagates in a non-periodic direction. Different types of fibers have been realized and studied.

The *band gap* or *hollow core fibers* [22] rely on the photonic band gap of a periodic structure to confine the light in an hollow core. The cladding must be designed to have a projected band gap for the light propagating along the fiber axis. The fabrication of these structures is challenging, requiring micro- or even nanoscale regularity along several kilometers of fiber in order to avoid unexpected variation of the band structure of the cladding in different part of the fiber that can lead to radiation losses. Such fibers have already been realized with ultra-low loss (below the 0.2 dB/km of the traditional step-index silica fiber), due to the propagation in air instead of glass [23]. Common applications for hollow-core Photonic Crystal Fibers include the realization of gas cells for nonlinear optics, quantum optics or frequency measurement [24], as well as high-power laser beam delivery [21].

The *index guiding fibers* [25] exploit the phenomenon of index-guiding as the traditional step-index fibers do in order to confine the radiation in the core, but a periodic cladding is used in order to add features to the fibers. For instance, *Endlessly single-mode fibers* [26] can be obtained, that exhibit single-mode propagation for all the frequencies (compatibly with the material properties). Engineered index-guiding fibers can be used to enhance nonlinear effects in the medium [27], for lasers [28, 29], to create birefringent behavior [30], and for mode dispersion control [31].

2.2.3 Negative Refraction

Under certain conditions, specially designed photonic crystals can behave as homogeneous dielectrics with a negative index of refraction [32–34]. A beam of light, transmitted from a conventional dielectric to such a material will experience unconventional beam steering, that obeys Snell's law with $n < 0$. To obtain this behavior, the eigenfrequency surfaces in k-space must present particular characteristics: they must be convex (in term of photonic effective mass $\partial^2\omega/\partial k_i \partial k_j$) and below the light cone. A plane wave incident onto the crystal will conserve the tangential component of the $\boldsymbol{k}$ vector, and can therefore couple only to determinate modes. If the eigenfrequency surfaces obey those conditions, the only modes available for coupling will be ones traveling in an unconventional (negative-refractionlike) direction. However, unlike left-handed materials (see Sect. 2.3), in which negative refraction is attained with an effective negative index (with negative permittivity and permeability), in this case the effective index is positive, and therefore Poynting vector and wave vector are in the same direction.

Negative-refracting materials have a number of interesting applications, first of all the possibility of constructing lenses with peculiar properties. Focusing of light can be achieved with a flat slab of negative-refracting material,

and this behavior has indeed been experimentally demonstrated [35].

2.3 Left-Handed Metamaterials

The metamaterial concept can be used to create media with properties that not exist in naturally occurring materials. Among these, the class of *left-handed materials* (LHM) is probably the most prominent. In these material, the effective relative permittivity μ_{eff} and permeability μ_{eff} are both negative. The electromagnetics of these substances has been analyzed first by Veselago, in his famous 1967 paper [36]. The solutions of Maxwell's equations for common dielectrics are valid in this case as well, with an important exception: when computing the index of refraction as seen by the wave, $n = \sqrt{\epsilon\mu}$, for ϵ and μ both negative, the minus sign of the square root must be taken. This means that the index of refraction is negative, and negative-refraction behavior must be exhibited by these material [37]. Indeed, structures possessing this property has been first proposed [1], and then, thanks to the advancement of fabrication techniques, experimentally demonstrated [38] in the past two decades, first for microwaves, and more recently, for optical frequencies [39–41]. The name "left-handed material" has been used by Veselago himself, and captures the main physical property of these systems: in a propagating plane wave, the vectors $\boldsymbol{E}$, $\boldsymbol{H}$ and $\boldsymbol{k}$ (wavevector) form a left-handed triplet, in opposition to what normally occurs in a positive dielectric. The phase velocity (directed as $\boldsymbol{k}$) and the power flow (Poynting's vector, $\boldsymbol{S} = \boldsymbol{E} \times \boldsymbol{H}$) are antiparallel, and the behavior of the light inside the material is somehow "reversed" [37].

The concept for fabricating such metamaterial is to combine a material possessing negative ϵ over a certain range of frequencies with another material exhibiting negative μ in the same frequency range. Metals naturally have negative permittivity in the visible-ultraviolet part of the spectrum, but the range of frequencies can be shifted downwards by decreasing the filling factor of the metal in the dielectric or air [42]. Negative magnetic permeability is achieved around the resonance of an LC circuit, that occurs at a frequency dependent on the values of the inductance and the capacitance. To obtain resonance at a certain frequency, those two parameters must be tuned accordingly; in particular, higher frequencies require smaller circuits. In [1], a split-cylinder geometry is proposed, in which the metallic cylindrical corona behaves as an inductor, while the split provides the capacitance. Indeed these two solutions have been combined to realize left-handed metamaterials at microwave frequencies. Recently, the research effort towards IR or visible LHM has focused on alternating layers of metal and dielectric, with particular geometries (such as the fishnet material, [41]).

Chapter 3

Theory

3.1 Introduction

In this Chapter, we recall some concepts from Classical Electromagnetics and Solid State Physics that will be used in this work, and successively derive the Auxiliary Field Formulation for the description of the electromagnetism of dispersive media, that is the main problem we aim to solve numerically. We also briefly present some basic concepts of the theories of the electromagnetism of periodic structures and the surface plasmons polaritons, in order to give a framework of reference for the interpretation of the simulation results.

3.2 Maxwell's Equations

According to the classical electromagnetic theory [43], the behavior of the electromagnetic field in a vacuum is described by Maxwell's Equations:

$$\begin{aligned} \nabla \times \boldsymbol{E} &= -\mu_0 \frac{\partial \boldsymbol{H}}{\partial t}, \\ \nabla \times \boldsymbol{H} &= \boldsymbol{J} + \epsilon_0 \frac{\partial \boldsymbol{E}}{\partial t}, \\ \nabla \cdot \boldsymbol{E} &= \frac{\rho}{\epsilon_0}, \\ \nabla \cdot \boldsymbol{H} &= 0, \end{aligned} \tag{3.1}$$

in which the charge density ρ and the current density $\boldsymbol{J}$ are the sources for the electric field $\boldsymbol{E}$ and the magnetic field $\boldsymbol{H}$.

In presence of a medium, Maxwell's Equations can be averaged over a certain spatial scale, obtaining the Maxwell's Equation for a macroscopic medium, whose sources are only the free charges and currents:

$$\begin{aligned} \nabla \times \boldsymbol{E} &= -\frac{\partial \boldsymbol{B}}{\partial t}, \\ \nabla \times \boldsymbol{H} &= \boldsymbol{J}_f + \frac{\partial \boldsymbol{D}}{\partial t}, \\ \nabla \cdot \boldsymbol{D} &= \rho_f, \\ \nabla \cdot \boldsymbol{B} &= 0. \end{aligned} \tag{3.2}$$

These equations must be accompanied by the *constitutive relations* that express the $\boldsymbol{D}$ and $\boldsymbol{B}$ fields in terms of $\boldsymbol{E}$, $\boldsymbol{H}$ and the properties of the material. In the most general case, the values of those fields at a certain point in space and at a certain time could depend on the position, the time, and on the values of the electric and magnetic fields in other points of the spacetime. If the relation is linear, one can write:

$$\begin{aligned} \boldsymbol{D}(\boldsymbol{x}, t) &= \int_{\mathbb{R}^3} \int_{-\infty}^{t} \epsilon(\boldsymbol{x}, \boldsymbol{x}', t, t') \boldsymbol{E}(\boldsymbol{x}', t') d\boldsymbol{x} dt, \\ \boldsymbol{B}(\boldsymbol{x}, t) &= \int_{\mathbb{R}^3} \int_{-\infty}^{t} \mu(\boldsymbol{x}, \boldsymbol{x}', t, t') \boldsymbol{H}(\boldsymbol{x}', t') d\boldsymbol{x} dt, \end{aligned} \tag{3.3}$$

since, of course, the $\boldsymbol{E}$ and $\boldsymbol{H}$ are linked by the linear relations (3.1). The integration over the time is carried from $-\infty$ to t because of the causality principle. From the hypothesis of homogeneity of space and time one can rewrite these relations as:

$$\begin{aligned} \boldsymbol{D}(\boldsymbol{x}, t) &= \int_{\mathbb{R}^3} \int_{-\infty}^{t} \epsilon(\boldsymbol{x} - \boldsymbol{x}', t - t') E(\boldsymbol{x}', t') d\boldsymbol{x} dt, \\ \boldsymbol{B}(\boldsymbol{x}, t) &= \int_{\mathbb{R}^3} \int_{-\infty}^{t} \mu(\boldsymbol{x} - \boldsymbol{x}', t - t') H(\boldsymbol{x}', t') d\boldsymbol{x} dt, \end{aligned} \tag{3.4}$$

in which only the relative displacement (in space and time) is important for the computation of the fields. The quantities ϵ and μ are called *permeability* and *permittivity* of the media, and define the response of the macroscopic media to the presence of an electromagnetic field. These quantities are in the general case tensors and as a particular case scalars; in the first case the media is called *anisotropic*, in the second *isotropic*. If these quantities depend on the values of the magnetic and electric fields in time instants different from t, we will say that the media is subjected to *temporal dispersion*, while if they depend on the fields in different points of space, to *spatial dispersion*. In this work we will deal mainly with *temporal dispersive* media, in which:

$$\epsilon(\boldsymbol{x}, t) = \delta(\boldsymbol{x}) \epsilon_0 \epsilon(t) \tag{3.5}$$

and *non-magnetic* media, in which $\mu = \mu_0$. ϵ_0 and μ_0 are constants called *vacuum permittivity* and *vacuum permeability*.

Using Fourier analysis, the relations (3.4) for a non-magnetic linear medium with temporal dispersion could be rewritten in the frequency domain:

$$\begin{aligned} \boldsymbol{D}(\boldsymbol{x},\omega) &= \epsilon_0\epsilon(\boldsymbol{x},\omega)\boldsymbol{E}(\boldsymbol{x},\omega), \\ \boldsymbol{B}(\boldsymbol{x},\omega) &= \mu_0\boldsymbol{H}(\boldsymbol{x},\omega), \end{aligned} \tag{3.6}$$

in which $\epsilon(\boldsymbol{x},\omega)$ is a function of the position and the frequency. By applying the same Fourier transform we can recast Maxwell's equations as an eigenvalue problem:

$$\nabla \times \frac{1}{\epsilon}\nabla \times \boldsymbol{H} = \frac{\omega^2}{c^2}\boldsymbol{H}, \tag{3.7}$$

with the transversality constraint $\nabla \cdot \boldsymbol{H} = 0$.

The Maxwell differential operator can be shown to be Hermitian [5] providing that ϵ is independent of the frequency ω of the radiation (non-dispersive dielectric). It is straightforward to show that those eigenfunctions of the Maxwell operator for which $\nabla \cdot \boldsymbol{H} \neq 0$ have eigenvalue zero by simply applying the divergence operator to the equation (3.7).

Eq. (3.7) can be also expressed in terms of the electric field $\boldsymbol{E}$:

$$\nabla \times \frac{1}{\mu_0}\nabla \times \boldsymbol{E} = \omega^2\epsilon_0\epsilon\boldsymbol{E}. \tag{3.8}$$

In the present work we will use mainly this formulation, since the electric field is directly related to the Drude-Lorentz model used for representing the permittivities.

3.2.1 Scaling Properties

An important property of Maxwell's equation, that will be widely used in the numerical implementation of this problem, is the scaling invariance. The problem (3.7), and the ones derived from it in the following sections, are invariant under the change of variables

$$\begin{aligned} \boldsymbol{r}' &= \frac{\boldsymbol{r}}{a}, \\ \omega' &= \sqrt{a}\omega. \end{aligned} \tag{3.9}$$

The usual procedure is to choose a length a, called *normalization length*, and perform the following change of variables:

$$\begin{aligned} \boldsymbol{r}^N &= \frac{\boldsymbol{r}}{a}, \\ \omega^N &= \omega\frac{a}{2\pi c}, \end{aligned} \tag{3.10}$$

where c is the speed of light. The distances $\boldsymbol{r}^N$ and frequencies ω^N are now dimensionless quantities, and, once the eigenproblem is solved and the eigenfrequencies computed, the results can be applied to a real structure by applying the inverse change of variables.

3.2.2 Polarization and 2D Problems

The theory presented naturally fits the three dimensions of the physical space. However, an important simplification can be made if the problem is independent of one of the three spatial coordinates, for instance z. In this case, the problem is two dimensional (in the x-y plane), all the partial derivatives in the z direction are null, and the Maxwell's equations can be separated in two sets of scalar equations: the first set contains the components E_x, E_y and H_z, while the second set contains H_x, H_y and E_z:

$$\begin{array}{ll} \text{Transverse Electric:} & \text{Transverse Magnetic:} \\ \nabla \times \left(\boldsymbol{E} \times \hat{k} \right) = -\mu_0 \frac{\partial H_z}{\partial t} \hat{k} & \nabla \times \left(\boldsymbol{H} \times \hat{k} \right) = -\mu_0 \frac{\partial E_z}{\partial t} \hat{k} \\ \nabla \times \left(H_z \hat{k} \right) = \epsilon_0 \frac{\partial}{\partial t} \left(\boldsymbol{E} \times \hat{k} \right) & \nabla \times \left(E_z \hat{k} \right) = \epsilon_0 \frac{\partial}{\partial t} \left(\boldsymbol{H} \times \hat{k} \right) \end{array} \tag{3.11}$$

The first set (with the in-plane electric field) is called *Transverse Electric* polarization (TE), while the second (with in-plane magnetic field) *Transverse Magnetic* (TM). The 3D problem is therefore converted into two 2D problems that can be solved separately.

3.3 Dispersive Media

Let us now consider the case of a media subject to temporal dispersion, in which the dielectric constant ϵ is (in the frequency domain) a function of ω. In this case the eigenvalue problem (3.7) is non-linear and its solution by numerical means is more complicated. Metals are a prime example of significantly dispersive materials in the infrared and optical frequencies. To study analytically this problem one can introduce theoretical models to describe the behavior of the electrons under the effect of an electromagnetic field. In particular, we will focus on the Drude and Lorentz models [44]. In the former, the electron dynamics in a lossy metal is described by the equation:

$$\dot{\boldsymbol{p}} = -\frac{1}{\tau} \boldsymbol{p} + \boldsymbol{f}, \tag{3.12}$$

in which $\boldsymbol{p}$ is the electron momentum, τ is the relaxation time for the metal and $\boldsymbol{f}$ is the force acting on the single electron. When an electromagnetic field is applied, the Lorentz force could be used:

$$\boldsymbol{f} = e \left(\boldsymbol{E} + \dot{\boldsymbol{x}} \times \boldsymbol{B} \right), \tag{3.13}$$

but, as a first order approximation, one can just revert to using just the force due to the electric field:

$$\boldsymbol{f} = e\boldsymbol{E}. \tag{3.14}$$

By defining an electron density n, one can write an equation for the polarization field $\boldsymbol{P} = en\boldsymbol{x}$:

$$\ddot{\boldsymbol{P}} + \frac{1}{\tau}\dot{\boldsymbol{P}} = n\boldsymbol{f} = n\frac{e^2}{m}\boldsymbol{E} = \omega_p^2\epsilon_0\boldsymbol{E}, \tag{3.15}$$

where $\omega_p^2 = \frac{e^2 n}{\epsilon_0 m}$ is the electron plasma frequency and is a characteristic frequency for the electron motion in the Drude model. Eq. (3.15) can be rewritten by taking the Fourier transform:

$$\boldsymbol{P} = \frac{\omega_p^2}{-\omega^2 - \frac{1}{\tau}i\omega}\boldsymbol{E}, \tag{3.16}$$

that leads to a complex dielectric permittivity which is frequency dependent:

$$\epsilon(\omega) = 1 - \frac{\omega_p^2}{\omega^2 + \frac{1}{\tau}i\omega}. \tag{3.17}$$

In the ideal case of a lossless metal, we can make the assumption that, in the Drude picture, the electron are not affected by collisions with ions and therefore take the limit $\tau \to \infty$. In this case the dielectric permittivity is real:

$$\epsilon(\omega) = 1 - \frac{\omega_p^2}{\omega^2}. \tag{3.18}$$

This model adequately describes the properties of noble metals such as gold, silver and copper in the optical region.

The Lorentz model can describe the behavior of many metals that have strong absorption in the ultraviolet region of the spectrum. This phenomenon is caused by the optical excitation of electronic transition, but can be modeled as well with a mechanical picture. Given a certain absorption frequency ω_0, the Lorentz model uses a damped harmonic oscillator dynamics for the electrons:

$$\ddot{\boldsymbol{x}} + \gamma\dot{\boldsymbol{x}} + \omega_0^2\boldsymbol{x} = \frac{e}{m}\boldsymbol{E}, \tag{3.19}$$

where γ is a damping coefficient that plays a role similar to the one of $1/\tau$ in the previous model. By defining the polarization and the plasma frequency as done above, one obtains the equation for the dynamics of the polarization:

$$\ddot{\boldsymbol{P}} + \gamma\dot{\boldsymbol{P}} + \omega_0^2\boldsymbol{P} = \omega_p^2\epsilon_0\boldsymbol{E}. \tag{3.20}$$

In this model, the dielectric permittivity is:

$$\epsilon(\omega) = 1 + \frac{\omega_p^2}{\omega_0^2 - \omega^2 - \gamma i\omega}. \tag{3.21}$$

In general, the optical properties of a metal in the visible part of the spectrum can be described by using a combination of the Drude model and N Lorentz oscillators:

$$\epsilon(\omega) = \frac{\omega_{p,\,\mathrm{D}}^2}{-\omega^2 - \frac{1}{\tau}i\omega} + \sum_{j=1}^{N}\left(1 + \frac{\omega_{p,j}^2}{\omega_{0,j}^2 - \omega^2 - \gamma_j i\omega}\right). \tag{3.22}$$

3.4 Eigenvalue Problem for Dispersive Media

3.4.1 Auxiliary Fields Description

Using auxiliary mechanical fields it is possible to formulate an Hermitian eigenvalue problem equivalent to Maxwell's equations in a medium obeying Drude and/or Lorentz model [45]. First we introduce the polarization velocity field $\boldsymbol{V}$:

$$\boldsymbol{V} = \dot{\boldsymbol{P}} \tag{3.23}$$

and recall the inhomogeneous Maxwell's equations in a non-magnetic medium in absence of free sources:

$$\begin{aligned} \nabla \times \boldsymbol{E} &= \mu_0 \frac{\partial \boldsymbol{H}}{\partial t}, \\ \nabla \times \boldsymbol{H} &= \frac{\partial \boldsymbol{D}}{\partial t}. \end{aligned} \tag{3.24}$$

From the constitutive relation $\boldsymbol{D} = \epsilon_0 \boldsymbol{E} + \boldsymbol{P}$, Eq. (3.24) becomes:

$$\begin{aligned} \nabla \times \boldsymbol{E} &= \mu_0 \frac{\partial \boldsymbol{H}}{\partial t}, \\ \nabla \times \boldsymbol{H} &= \epsilon_0 \frac{\partial \boldsymbol{E}}{\partial t} + \boldsymbol{V}. \end{aligned} \tag{3.25}$$

Adding Eq. (3.20) for the polarization dynamics and Eq. (3.23), one obtains the following system of equations:

$$\begin{aligned} \nabla \times \boldsymbol{E} &= -\mu_0 \frac{\partial \boldsymbol{H}}{\partial t}, \\ \nabla \times \boldsymbol{H} &= \epsilon_0 \frac{\partial \boldsymbol{E}}{\partial t} + \boldsymbol{V}, \\ \boldsymbol{V} &= \frac{\partial \boldsymbol{P}}{\partial t}, \\ \omega_p^2 \epsilon_0 \boldsymbol{E} - \omega_0^2 \boldsymbol{P} - \gamma \boldsymbol{V} &= \frac{\partial \boldsymbol{V}}{\partial t}. \end{aligned} \tag{3.26}$$

Assuming an oscillating time-dependence of the fields in the form $\exp(-i\omega t)$, one can rewrite Eqs. (3.26) in matrix form:

$$\omega \begin{bmatrix} \boldsymbol{H} \\ \boldsymbol{E} \\ \boldsymbol{P} \\ \boldsymbol{V} \end{bmatrix} = \begin{bmatrix} 0 & \frac{i}{\mu_0}\nabla\times & 0 & 0 \\ -\frac{i}{\epsilon_0}\nabla\times & 0 & 0 & \frac{i}{\epsilon_0} \\ 0 & 0 & 0 & -i \\ 0 & -i\omega_p^2 & i\omega_0^2 & i\gamma \end{bmatrix} \begin{bmatrix} \boldsymbol{H} \\ \boldsymbol{E} \\ \boldsymbol{P} \\ \boldsymbol{V} \end{bmatrix}. \tag{3.27}$$

The (in general, complex) eigenvalues of these equations are the generalized frequencies in the structure, while the eigenfunctions are the electromagnetic and mechanical fields that solve the curl Maxwell's equations for the

problem. We remind that the true solutions must satisfy both the problem (3.27) and the divergence Maxwell's equations:

$$\begin{aligned} \nabla \cdot \boldsymbol{H} &= 0, \\ \nabla \cdot (\epsilon_0 \boldsymbol{E} + \boldsymbol{P}) &= 0. \end{aligned} \tag{3.28}$$

3.4.2 Two-fields Description for the Lossless Case

Starting from the same equations (3.26) it is possible to formulate the problem in the lossless case ($\gamma = 0$) in terms of only two fields, one accounting for the behavior of the electromagnetic field and one describing the electron dynamics. In terms of the $\boldsymbol{E}$ and $\boldsymbol{P}$ fields, we can write:

$$\omega^2 \begin{bmatrix} \boldsymbol{E} \\ \boldsymbol{P} \end{bmatrix} = \begin{bmatrix} \frac{1}{\epsilon_0}\nabla \times \frac{1}{\mu_0}\nabla \times \bullet + \omega_p^2 \bullet & -\frac{\omega_0^2}{\epsilon_0}\bullet \\ -\omega_p^2 \epsilon_0 \bullet & \omega_0^2 \bullet \end{bmatrix} \begin{bmatrix} \boldsymbol{E} \\ \boldsymbol{P} \end{bmatrix}, \tag{3.29}$$

where $\bullet$ are placeholders for the operators. The transversality condition can be written as a matrix equation as well:

$$\begin{bmatrix} \epsilon_0 \nabla \cdot \bullet & \nabla \cdot \bullet \end{bmatrix} \begin{bmatrix} \boldsymbol{E} \\ \boldsymbol{P} \end{bmatrix} = 0. \tag{3.30}$$

The differential operator in (3.29) can be recast as an Hermitian operator by a simple change of scale, as in [45]: by defining the matrix $S = diag(\epsilon_0, \frac{\omega_0^2}{\omega_p^2 \epsilon_0})$, one can write:

$$\omega^2 \begin{bmatrix} \sqrt{\epsilon_0}\boldsymbol{E} \\ \frac{\omega_0}{\omega_p \sqrt{\epsilon_0}}\boldsymbol{P} \end{bmatrix} = \begin{bmatrix} \frac{1}{\sqrt{\epsilon_0}}\nabla \times \frac{1}{\mu_0}\nabla \times \left(\frac{1}{\sqrt{\epsilon_0}}\bullet\right) + \omega_p^2 \bullet & -\omega_p \omega_0 \bullet \\ -\omega_p \omega_0 \bullet & \omega_0^2 \bullet \end{bmatrix} \begin{bmatrix} \sqrt{\epsilon_0}\boldsymbol{E} \\ \frac{\omega_0}{\omega}{}_p \sqrt{\epsilon_0}\boldsymbol{P} \end{bmatrix}. \tag{3.31}$$

The matrix operator $\hat{\Phi}$

$$\hat{\Phi} = \begin{bmatrix} \frac{1}{\sqrt{\epsilon_0}}\nabla \times \frac{1}{\mu_0}\nabla \times \left(\frac{1}{\sqrt{\epsilon_0}}\bullet\right) + \omega_p^2 \bullet & -\omega_p \omega_0 \bullet \\ -\omega_p \omega_0 \bullet & \omega_0^2 \bullet \end{bmatrix} \tag{3.32}$$

is Hermitian. From this formulation one can obtain some of the previous problem as particular cases. By taking, for instance, $\omega_0 \to +\infty$ and $\omega_p \to 0$ in Eq. (3.29), one can model the behavior of a non-dispersive media with $\epsilon_r = 1$ (free space). In this case, there are two classes of solutions: one with $\omega = \omega_p$ and one with $\boldsymbol{P} = 0$. In the second class, the $\boldsymbol{E}$ field is solution of the problem

$$\omega^2 \boldsymbol{E} = \frac{1}{\epsilon_0}\nabla \times \frac{1}{\mu_0}\nabla \times \boldsymbol{E}. \tag{3.33}$$

As a second, more important, particular case one can try to use the formulation (3.31) for the Drude model seen as a Lorentz model with $\omega_0 \to 0$. In this case, the electric field is not coupled to the polarization but only with its

derivative $\boldsymbol{V}$, that in the frequency domain is directly proportional to the electric field:

$$\boldsymbol{V} = \epsilon_0 \frac{\omega_p^2}{\omega^2} \boldsymbol{E}. \tag{3.34}$$

The solutions of the problem for a Drude metal are therefore simply the solutions of the problem

$$\omega^2 \boldsymbol{E} = \frac{1}{\epsilon_0} \nabla \times \frac{1}{\mu_0} \nabla \times \boldsymbol{E} + \omega_p^2 \boldsymbol{E}. \tag{3.35}$$

3.5 Periodic Structures

In this section we will show how to formulate and solve Maxwell's equation in a periodic structure. A n-dimensional periodic structure can be described with a permittivity and permeability that follow the relation:

$$\begin{aligned} \epsilon(\boldsymbol{x} + \boldsymbol{R}) &= \epsilon(\boldsymbol{x}), \\ \mu(\boldsymbol{x} + \boldsymbol{R}) &= \mu(\boldsymbol{x}), \end{aligned} \tag{3.36}$$

with

$$\boldsymbol{R} = \sum_{j=1}^{n} c_j \boldsymbol{a}_j, \tag{3.37}$$

in which $\boldsymbol{a}_j$ are n linearly independent vectors called *lattice vectors* and define the periodicity of the structure. The discrete spatial periodicity of the structure greatly affects the behavior of the electromagnetic field, that, in this case, is closely related to the description of the behavior of a single electron (from the quantum-mechanical point of view) in a periodic potential. In fact, we have the Hermitian operator (3.7) with discrete translational symmetry whose eigenfunctions (subjected to the transversality constraint) are the field configurations allowed in the structure, a problem very similar to the one posed by Schroedinger's Equation in a periodic potential. This analogy is the reason for the name *Photonic Crystal*, commonly used to address these structures.

3.5.1 Optical Bloch Theorem

The results from Bloch's Theorem, originally formulated for the Hamiltonian operator, can still be applied for the Maxwell's operator. We will look for eigenfunctions in the form:

$$\boldsymbol{H}_{\boldsymbol{k}}(\boldsymbol{x}) = e^{i\boldsymbol{k}\cdot\boldsymbol{x}} \boldsymbol{u}_{\boldsymbol{k}}(\boldsymbol{x}), \tag{3.38}$$

where $\boldsymbol{u}$ is a periodic function with the periodicity of the structure and $\boldsymbol{k}$ is a vector called *wave vector*. The $\boldsymbol{k}$-vector could be expressed as linear combination of the reciprocal lattice vectors that define the reciprocal lattice and the Brillouin zone. In general, for a certain value of the $\boldsymbol{k}$-vector one obtains different eigenvalues ω. By labeling each

eigenvalue with an increasing integer index n we obtain a set of functions $\omega_n = \omega_n(\boldsymbol{k})$ called *dispersion relations* for the structure, which express the allowed configurations of the electromagnetic field (in terms of their wave vector and frequency) that can exist in the structure. The integer n is called band index, and the set of allowed frequencies is called *photonic bands* (in analogy to the electronic bands). We emphasize that unlike the electronic bands, which are obtained with a single-electron approximation, the photonic bands are obtained from the solutions of Maxwell's equations and therefore describe the exact behavior of the electromagnetic field in the structure (under the assumptions of classical electromagnetism).

3.5.2 Photonic Bands

The knowledge of the photonic bands of a periodic structure offers deep insight to its optical properties. Particular features in the band diagram are strictly related with physical phenomena that occur in the medium. If there exist a frequency range in which no solutions of Maxwell's equation exist for a certain direction of $\boldsymbol{k}$, then the structure is said to possess a *Photonic Band Gap* in that frequency range and in that direction. A band gap extending in every direction is called a *complete* band gap, and indicates that no radiation in that range of frequencies can propagate inside the structure. A well-known example of a structure possessing a photonic band gap is a dielectric mirror [5]: the one-dimensional-periodic structure possess a band gap in the periodicity direction, that forbids the propagation of the light in a certain frequency range. For real mirrors, with limited length, the propagation is not forbidden but a high reflectivity is obtained instead. We point out here for future reference that free-space can be considered a periodic medium of arbitrary periodicity, and it is straightforward to show that the wave vector introduced in this section coincides with the usual wave vector of the electromagnetic radiation $k = \frac{2\pi}{\lambda}$, and that free space modes obey the dispersion relation $\omega = kc$.

3.5.3 Waveguides

Structures exhibiting a periodicity in less dimensions than the embedding space (e.g. a chain of spheres in a three-dimensional space) can, under certain conditions, behave like waveguides. The eigenmodes of the electromagnetic radiation can be classified either as guided modes, that are confined in proximity of the structure and decay exponentially in non-periodic directions, or radiating modes, that are not confined in the structure. The discrimination between the two types is given by their dispersion relation. In order to propagate in free-space, an eigenmode must obey the free-space dispersion relation $\omega = kc$. In this particular case, the wavevector $\boldsymbol{k}$ can be decomposed in its component along the directions of periodicity, $\boldsymbol{k}_p$, and the orthogonal component $\boldsymbol{k}_n p$. For a given value of $\boldsymbol{k}_p$, all

the values of $\boldsymbol{k}_{np}$ for which

$$\boldsymbol{k} = \boldsymbol{k}_p + \boldsymbol{k}_{np} = \frac{\omega}{c} \tag{3.39}$$

are allowed, and the corresponding modes are radiative. Thus the band diagram exhibit a continuum of radiative states in the region $\omega \geq k_{np}c$ (called *light cone*) and a discrete set of guided states for $\omega < k_{np}c$. The delimiting line $\omega = k_{np}c$ is called *light line*.

3.6 Plasmons

In the Drude picture of the physics of an electron gas, expressed by Eqs. (3.15) and (3.18), by taking into account the electric field generated by inhomogeneities of the electron density and its effects on the density itself, one can predict the presence of oscillations of the electron density and the electromagnetic field inside the medium. Those oscillations are called *plasmons*[1] and, in the long-wavelength limit, have a characteristic frequency called *plasma frequency* ω_p.

A simple theory of plasmons can be formulated from the assumptions of the free electron model. Starting from the equation of motion of the single electron in an electric field without losses,

$$m\ddot{\boldsymbol{x}} = -e\boldsymbol{E}, \tag{3.40}$$

one can obtain the permittivity of the free electron gas, as done in Sect. 3.3:

$$\epsilon(\omega) = 1 - \frac{\omega_p^2}{\omega^2}. \tag{3.41}$$

From this result it is possible to formulate a dispersion relation for the electromagnetic waves traveling in the metal. The propagation of the radiation is seriously affected by the presence of the electron gas, and is substantially different from the propagation in a dielectric (non-dispersive) medium. The dispersion relation for the electromagnetic waves in a linear medium with permittivity $\epsilon(\omega)$ is [46]:

$$\epsilon(\omega)\frac{\omega^2}{c^2} = k^2, \tag{3.42}$$

where k is the magnitude of the wavevector, supposing a spatial depencence $exp(i\boldsymbol{k}\cdot\boldsymbol{r})$. Using the permittivity from Eq. (3.41), the dispersion relation is

$$\omega^2 - \omega_p^2 = c^2k^2. \tag{3.43}$$

There are three kinds of solutions of this equation:

[1] The correct definition of Plasmon is a *quantized* plasma oscillation [46, 47], but we will follow here the custom [42, 44] of referring to (classical) collective plasma oscillations with the same term.

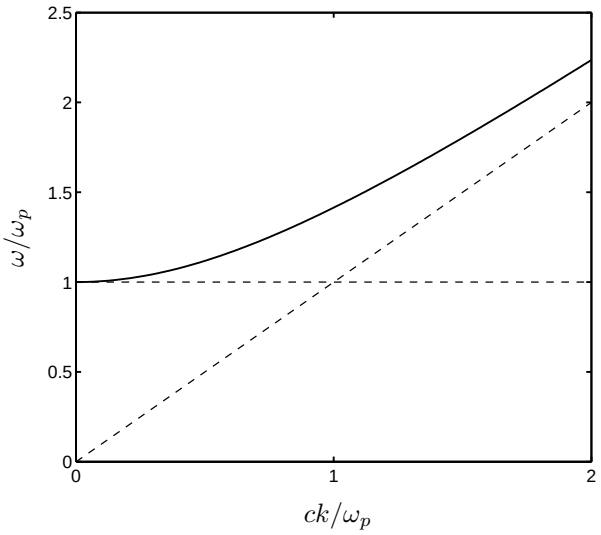

Figure 3.1: Dispersion relation of electromagnetic waves for the free electron gas model. The frequency is ω_p in the long wavelength limit and approaches the free-space dispersion relation $\omega = ck$ for $k \to +\infty$

- $\omega = \omega_p$. In this case free oscillations of the electromagnetic field occur, supported by the electron gas, with $k = 0$ (standing waves).
- $\omega > \omega_p$, that gives a real k. These are transversal oscillations of the electromagnetic field, and they correspond to waves propagating in the metal.
- $\omega < \omega_p$, that gives an imaginary k. The electromagnetic field is evanescent in the metal (decays exponentially) and therefore these oscillations do not propagate.

The dispersion relation for the free electron gas is plotted in Fig. 3.1. The graph shows that, under the assumption of this model, electromagnetic radiation can propagate in a metal for frequencies greater than ω_p; the propagation is forbidden at lower frequencies and there are free oscillations at $\omega = \omega_p$ for all the values of k.

3.7 Surface Plasmon Polaritons

In the previous section we gave a description of plasma oscillations in a bulk metal. A related, but substantially different, type of oscillations occur at the interfaces between a positive-ϵ and a negative-ϵ material, such as a dielectric and metal. The interface behaves as a waveguide, confining the mode in the direction transversal to the

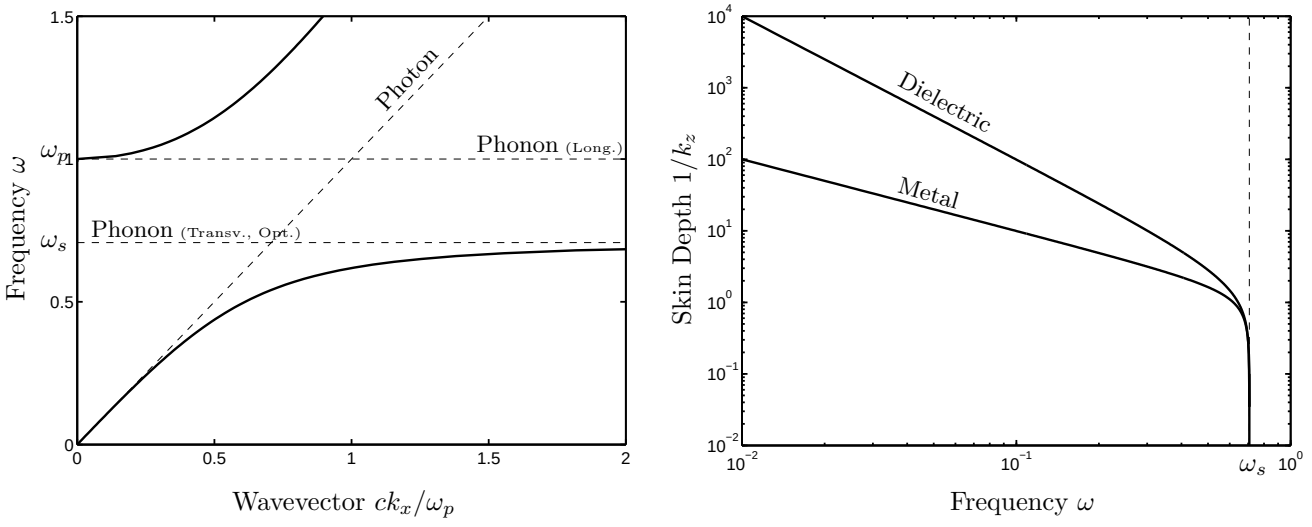

(a) (b)

Figure 3.2: (a) Theoretical dispersion relation for surface plasmon polaritons obtained with the Free Electron Gas model, for a metal-air interface ($\epsilon_d = 1$). The dashed lines represent the photon ($\omega = ck$, light cone) and the phonon (electronic density oscillation) dispersion relations. (b) Double Logarithmic plot of $1/k_z$ (proportional to the skin depth) as a function of the frequency. The graph shows that as the frequency of the SPP approaches the limit value ω_s, the skin depth reduces and the electromagnetic field is more and more concentrated at the interface.

surface, with the electromagnetic field amplitude decaying exponentially as the distance from the interface increases. Those oscillations are called *Surface Plasmons* (SP) [48], and when coupled to propagating e.m. waves that take the name of *Surface Plasmon Polaritons* (SPP).

In the free electron model, the oscillations occur at frequencies below ω_p, laying in the forbidden region of the bulk metal dispersion relation, and therefore cannot be coupled to modes propagating inside the metal. The surface modes laying under the light cone cannot propagate in the dielectric either, and remain confined at the interface.

We will begin with presenting the features of SPP on a metal-dielectric interface, following [48]. The metal is described by a free electron gas model, with the permittivity (3.41), while the dielectric has a constant ϵ_d. The interface lays in the x-y plane, with the metal region for $z < 0$ and the dielectric region for $z > 0$, and we will consider SP propagating in the x direction. The surface plasmons are solution of Maxwell's Equation with the form

$$\boldsymbol{E} = \begin{cases} \boldsymbol{E}_0^m e^{ik_x x} e^{k_z^m z} & \text{for } z < 0 \text{ (metal)}, \\ \boldsymbol{E}_0^d e^{ik_x x} e^{k_z^d z} & \text{for } z > 0 \text{ (dielectric)}. \end{cases} \tag{3.44}$$

Imposing the interface conditions on $\boldsymbol{E}$ and $\boldsymbol{D}$, one obtains the following relations:

$$k_x^2 c^2 = \omega^2 \epsilon_d \frac{1-\frac{\omega_p^2}{\omega^2}}{\epsilon_d+1-\frac{\omega_p^2}{\omega^2}}, \tag{3.45}$$

$$(k_z^d)^2 c^2 = -\omega^2 \epsilon_d^2 \frac{1}{\epsilon_d+1-\frac{\omega_p^2}{\omega^2}}, \tag{3.46}$$

$$(k_z^m)^2 c^2 = \omega^2 \frac{1-\frac{\omega_p^2}{\omega^2}}{\epsilon_d+1-\frac{\omega_p^2}{\omega^2}}. \tag{3.47}$$

Eq. (3.45) is the SPP dispersion relation, and is plotted in Fig. 3.2a, consisting in two branches. The lower one resembles the dispersion relation of photons ($\omega = ck$) in the long wavelength limit, while for shorter wavelength it approaches the transversal plasma frequency on the surface. In the middle frequency range, where the photon-phonon coupling is more significant, the dispersion relation has a different behavior.

From Eqs. (3.46) and (3.47) the penetration length of the surface plasmon (*skin depth*, proportional to $1/k_z$) can be computed. The plot of $1/k_z$ versus the frequency ω, presented in Fig. 3.2b, shows how as the frequency of the SPP approaches ω_s (and the wavelength becomes shorter) the e.m. field is more confined at the surface.

Particularly interesting are the cases of surface plasmons on infinite cylinders (a two-dimensional problem) and spheres (three-dimensional) embedded in a dielectric, because of their relevance in the applications. The symmetry of the interfaces imposes periodicity of the solutions along the angular coordinates. A consequence of this is that the resonance frequencies are discretized, and can be assigned a mode order n [49]. For a cylindrical geometry, only the oscillations in the x-y plane are subjected to this condition. Therefore, when dealing with 2D problems, the TE polarization must be considered in order to investigate the resonances.

An analytical description of these SP can be carried with the aid of Bessel's functions (cylindrical harmonics, see for example [50]) and spherical harmonics. The main results from the theory are:

- as the mode order n increase, the electromagnetic field is more and more concentrated at the interface;
- in the limit $n \to +\infty$, the plasmon resonance frequency approaches $\omega_p/\sqrt{1+\epsilon_b}$, where ϵ_b is the relative permittivity of the dielectric (for vacuum or air, the plasmon resonance frequency is therefore $\omega_p/\sqrt{2}$.

For more general geometries, the analytic solution may not exist, but these rules are still valid.

Chapter 4

Numerical Methods

4.1 Introduction

In this chapter we will address the numerical methods used to discretize the differential problems presented in Chap. 3, in order to compute approximated solutions by numerical means. The eigenvalue problem we want to discretize is the Drude-model based equation, as presented in Eqs. (3.35) and (3.8):

$$\nabla \times \frac{1}{\mu_0} \nabla \times \boldsymbol{E} + \omega_p^2 \boldsymbol{E} = \omega^2 \epsilon_0 \epsilon \boldsymbol{E}, \tag{4.1}$$

with the condition that for each point in space, either $\omega_p \neq 0$ (the point is in a metallic region), or $\epsilon \neq 1$ (the point is in a dielectric region), but not both. The condition $\omega_p = 0$ and $\epsilon = 1$ correspond to a point in a free-space (or air) region. We point out here that in the following, the values of physical constants, where possible, will be set to 1, for simplicity. Therefore,

$$\begin{aligned} \epsilon_0 &= 1, \\ \mu_0 &= 1, \end{aligned} \tag{4.2}$$

and consequently

$$c = 1. \tag{4.3}$$

Introducing a normalization length, indicated by a, and remembering the scaling properties of Maxwell's equations presented in Sect. 3.2.1, all the physical quantities involved can be normalized to dimensionless numbers, according

to the rules:

$$\begin{aligned} &\text{Lengths:} \quad l^N = \frac{l}{a} \\ &\text{Wavelengths:} \quad \lambda^N = \frac{\lambda}{a}, \\ &\text{Frequencies:} \quad \omega^N = \omega \frac{a}{2\pi c} \end{aligned} \tag{4.4}$$

Since the one presented is an eigenvalue problem, in which the eigenfunctions ω must be determined, this is a *Frequency Domain* approach. To discretize the spatial derivatives in Eq. (4.1) we used separately the Finite-Difference Method (FDM) and the Finite-Elements Method (FEM). In the following sections we describe these schemes.

4.2 Finite-Difference Method

The FDM approach is based on the substitution of spatial partial derivatives in Eq. (4.1) with difference quotients over a finite distance h. The unknowns (electric fields configurations) are converted from complex vector-valued functions to arrays of complex numbers, each element of which correspond to the value of a certain component of the electric field at a certain point in space. The differential operators are converted into finite-dimensional matrices, and the (generalized) eigenvalues of the operators are approximated by the (generalized) eigenvalues of the matrices. The discrete problems obtained from (4.1) is therefore:

$$M_{ij} e_j + \omega_{p,i}^2 e_i = \omega^2 F_{ij} e_j, \tag{4.5}$$

in which the implicit summation convention is used and $\omega_{p,i}$ is the plasma frequency at the point of evaluation of e_i. The problem is said to be *consistent* if, by taking the limit $h \to 0$, the generalized eigenvalues of M and F converge to the eigenfrequencies and the discretized electric fields e converge to interpolations of the actual eigenfunctions $\boldsymbol{E}$. The first step of the FDM approach is to define a suitable discretization of space, that is, to identify the points in which compute the components of the electric field. In this work, we used a rectangular grid based on the Yee grid, commonly used in computational electromagnetics.

4.2.1 Space Discretization

Kane Yee [51] proposed in 1966 a staggered grid suitable for electromagnetic problems. Given a rectangular unit cell in 3D, each component of the magnetic and electric fields is evaluated at a different point in space. The electric field x, y and z components are evaluated at the midpoint of the corresponding edges, while the magnetic field

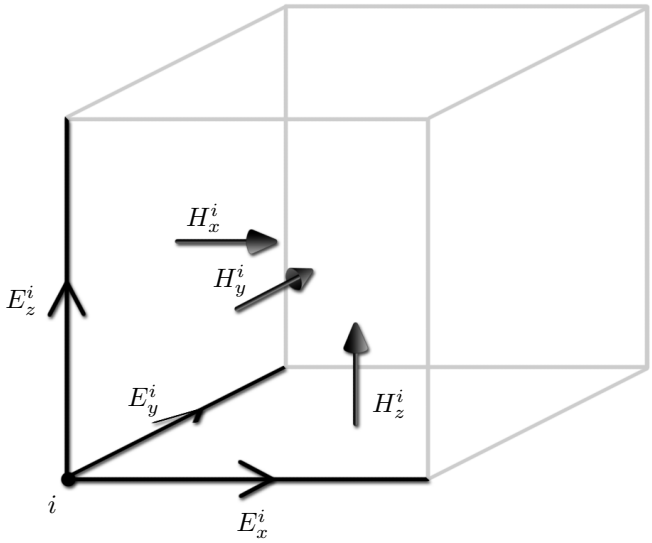

Figure 4.1: Unit cell and vector components evaluation positions for a cubic Yee grid.

components are evaluated in the middle of the faces orthogonal to the corresponding components. Fig. 4.1 presents the 3D unit cell for a Yee grid. This grid can be used also for two-dimensional problem, for TE and TM polarization (see Sect. 3.2.2), by considering a rectangular unit cell, in which the in-plane field component (respectively, $\boldsymbol{E}$ and $\boldsymbol{H}$) are evaluated along the sides of the rectangle, while the orthogonal field component (H_z and E_z) is evaluated in the middle of the cell. In the following, we will call *E-grid* and *H-grid* the collection of points in which, respectively, the $\boldsymbol{E}$ and $\boldsymbol{H}$ fields are evaluated.

This disposition of the field components simplify the evaluation of the curls in the Maxwell's equations. Fig. 4.2 shows the computation procedure for the curl of the electric field. The magnitude of the curl depends on the values of the $\boldsymbol{E}$ field components along the edges, while the direction and point of evaluation are the same as the $\boldsymbol{H}$ field component in the middle of the face. Another advantage of the Yee grid is that the boundary and interface conditions for the electromagnetic fields are easily implemented. Typically, at a dielectric-dielectric interface, the continuity of $\boldsymbol{H} \cdot \hat{n}$ and $\boldsymbol{E} \times \hat{n}$ is requires. This can be easily imposed on a Yee grid by taking the interface lying along a face. For our problem (Eq. (4.1)), the magnetic field $\boldsymbol{H}$ is not evaluated and stored separately. Instead, first we compute the curl of the electric field, and immediately after (after the multiplication by $1/\mu_0$) we compute the curl of the result. The spatial discretization therefore involves only the electric field, whose components are evaluated, as usual, along the edges of the cubic cells.

A few words must be spent regarding the ordering of the unknown values. To obtain a square matrix, we must assign a progressive number to each unknown and order a collection of points in a three-dimensional domain into a

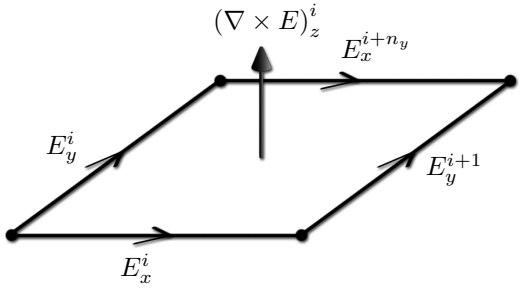

Figure 4.2: Computation of curl on a 2D rectangular grid.

one-dimensional array. We chose to order the points along the y direction first, then along x and z, consistently with `MATLAB`'s `reshape` function. A single vector is built concatenating the vectors containing the three field components. For a volume divided in $n_x \times n_y \times n_z$ grid points, the unknown vector size (before applying boundary conditions) is $N = 3 \cdot n_x \cdot n_y \cdot n_z$.

4.2.2 Problem Discretization

In order to obtain a matrix M that discretizes the differential operator in Eq. (4.1), we first write the discretized curl for a vector field defined on the E-grid, that is evaluated on the H-grid, in the form of a matrix C^e; successively, we write the discretized curl for a vector field defined on the H-grid, evaluated on the E-grid, obtaining a matrix C^h. The matrix M will then be obtained multiplying the two curl matrices:

$$M = C^h C^e, \tag{4.6}$$

where the normalization expressed in (4.2) has been used. To obtain the curl matrices, we recall the expression of the curl in Cartesian coordinates:

$$\nabla \times \boldsymbol{V} = \hat{\imath}\left(\frac{\partial V_z}{\partial y} - \frac{\partial V_y}{\partial z}\right) + \quad \hat{\jmath}\left(\frac{\partial V_x}{\partial z} - \frac{\partial V_z}{\partial x}\right) + \quad \hat{k}\left(\frac{\partial V_y}{\partial x} - \frac{\partial V_x}{\partial y}\right). \tag{4.7}$$

Using the point ordering presented in the previous section, it is clear that the curl matrices can be obtained by simply arranging the matrices obtained discretizing the partial derivatives in Cartesian coordinates:

$$C = \begin{bmatrix} 0 & -D_z & D_y \\ D_z & 0 & -D_x \\ -D_y & D_x & 0 \end{bmatrix}. \tag{4.8}$$

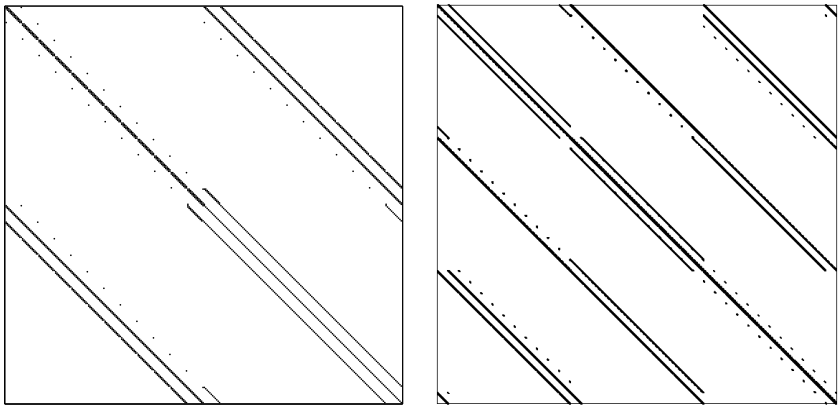

Figure 4.3: An example of the sparsity pattern of the matrices obtained discretizing a 2D (left) and 3D (right) problem with the FDM, with Bloch boundary conditions applied.

Finally, we present the formulae used to build the discretized partial derivative matrices in Cartesian coordinates on the E-grid. Starting from the finite-difference discretization of partial derivatives,

$$\begin{aligned}\left(\frac{\partial V_x}{\partial x}\right)_i &= \frac{V_{x,i+n_y} - V_{x,i}}{h_x},\\ \left(\frac{\partial V_y}{\partial y}\right)_i &= \frac{V_{y,i+1} - V_{y,i}}{h_y},\\ \left(\frac{\partial V_z}{\partial z}\right)_i &= \frac{V_{z,i+n_x \cdot n_y} - V_{z,i}}{h_z},\end{aligned} \tag{4.9}$$

the following construction scheme for the partial derivative matrices can be obtained:

$$D^e_{x,ij} = \begin{cases} -\frac{1}{h_x}, & j = i \\ \frac{1}{h_x}, & j = i + n_y \end{cases} \quad D^e_{y,ij} = \begin{cases} -\frac{1}{h_y}, & j = i \\ \frac{1}{h_y}, & j = i + 1 \end{cases} \quad D^e_{z,ij} = \begin{cases} -\frac{1}{h_x}, & j = i \\ \frac{1}{h_x}, & j = i + n_x \cdot n_y \end{cases} \tag{4.10}$$

The matrices for the H-grid, with the used ordering, are obtained simply by taking the transposes of the matrices for the E-grid, with the sign changed:

$$D^h_{x,ij} = -D^e_{x,ji}, \quad D^h_{y,ij} = -D^e_{y,ji}, \quad D^h_{z,ij} = -D^e_{z,ji}. \tag{4.11}$$

The matrix M obtained with this discretization scheme is real symmetric. Fig. 4.3 presents some examples of the sparsity pattern of the matrices involved.

The matrix F is simply the diagonal matrix of the relative dielectric permittivities:

$$F_{ij} = \begin{cases} \epsilon_i & i = j, \\ 0 & i \neq j, \end{cases} \tag{4.12}$$

where ϵ_i is the (possibly space-averaged) relative dielectric permittivity at the point of evaluation of e_i.

4.2.3 Boundary Conditions

After building the FDM matrices M and F, suitable boundary conditions must be applied. The two types of boundary conditions used in this work are Perfect Electric Conductor (PEC) and Bloch-Periodic. Rather than directly acting on the elements of the matrix M in order to enforce these conditions, we used a conceptually simpler approach, based on a multiplication by a reduction matrix, that eliminates the redundant degrees of freedom.

For a PEC boundary conditions, the tangential component of the electric field along the boundary must be set to zero. If the boundary lies along a face of the grid, the PEC condition simply reduces to setting to zero (removing from the matrix) the electric field components on the edges of that face. We build a reduction matrix R starting from the identity matrix of size $3 \cdot n_x \cdot n_y \cdot n_z \times 3 \cdot n_x \cdot n_y \cdot n_z$, and removing the columns corresponding to the boundary edges. The conditions are then enforced by performing the following matrix multiplication:

$$\begin{aligned} M_b &= R^T M R, \\ F_b &= R^T F R. \end{aligned} \tag{4.13}$$

M_b and F_b are square matrices with a reduced number of degrees of freedom.

For Bloch-Periodic boundary conditions, we must set the value of the electric field tangential components on a boundary equal to the value of the field on the opposite boundary multiplied by a phase factor, dependent from $\boldsymbol{k}$ and the distance between them. To build the reduction matrix, a few steps are required:

- for each pair of corresponding opposite boundaries, one is chosen as the *source*, and the other as the *destination*;
- a square matrix R^s of size $3 \cdot n_x \cdot n_y \cdot n_z \times 3 \cdot n_x \cdot n_y \cdot n_z$ is built according to the following rule:

$$R^s_{ij} = \begin{cases} 1, & i = j, \\ exp\left(-i\boldsymbol{k} \cdot \boldsymbol{r_{ij}}\right), & i \text{ on source, } j \text{ corresponding to } i \text{ on destination,} \\ & \text{with orientation,} \end{cases} \tag{4.14}$$

  where $\boldsymbol{r_{ij}}$ is the distance between the two evaluation points i and j;
- the reduction matrix R is obtained removing the columns of R^s corresponding to points on the source boundary.

4.2.4 Divergence Constraint

As to be explained in Chap. 5, the eigensolver algorithm `LOBPCG` must be provided with a matrix D that discretizes the divergence Maxwell's equations (the divergence constraint), Eq. (3.30). We chose to evaluate the divergence of $\boldsymbol{E}$ (a scalar field) on the vertices of the grid cell (the grid nodes). For the construction of the matrix D, as done before with the curl, we recall the expression of the divergence of a vector field in Cartesian coordinates:

$$\nabla \cdot \boldsymbol{V} = \frac{\partial V_x}{\partial x} + \frac{\partial V_y}{\partial y} + \frac{\partial V_z}{\partial z}. \tag{4.15}$$

The matrix D can therefore be constructed in the following way:

$$D = [D_x \; D_y \; D_z] \, F. \tag{4.16}$$

Boundary conditions can be applied using the reduction matrix method:

$$D_b = DR. \tag{4.17}$$

4.3 Finite-Element Method

The approach we used for the FEM formulation is from Jianming Jin's book *The Finite Elements Method in Electromagnetics* [52]. The differential problem (4.1) can be written as

$$\begin{aligned} &\text{Find } \boldsymbol{E} \in \boldsymbol{H}^1(\text{curl}; \Omega) \text{ and } \omega \in \mathbb{R} \text{ such that} \\ &\hat{\Phi}\boldsymbol{E} = \omega^2 \epsilon_0 \epsilon \boldsymbol{E}, \end{aligned} \tag{4.18}$$

where $\hat{\Phi}$ is the Hermitian operator whose (generalized) eigenvalues we want to compute, defined as

$$\hat{\Phi} = \nabla \times \frac{1}{\mu_0} \nabla \times \bullet + \omega_p^2 \bullet . \tag{4.19}$$

The space of the solutions of the Problem (4.18) is defined as

$$\boldsymbol{H}^1(\text{curl}; \Omega) = \left\{ \boldsymbol{v} \; : \; \int_\Omega |\boldsymbol{v}|^2 < +\infty \quad \text{and} \int_\Omega |\nabla \times \boldsymbol{v}|^2 < +\infty \right\}. \tag{4.20}$$

The approach we chose to deal with this problem is the *Galerkin method*. It defines the solution of the problem as the function whose residual is orthogonal to a subspace V^h of $\boldsymbol{H}^1(\text{curl}; \Omega)$. A detailed explanation follows.

Given an arbitrary function $\tilde{\boldsymbol{E}} \in \boldsymbol{H}^1(\text{curl}; \Omega)$, we define the *residual* as:

$$\boldsymbol{r} = \hat{\Phi}\tilde{\boldsymbol{E}} + \omega_p^2 \tilde{\boldsymbol{E}} - \omega^2 \epsilon_0 \epsilon \tilde{\boldsymbol{E}}. \tag{4.21}$$

It is obvious that if $r = 0$ then $\tilde{\boldsymbol{E}}$ is the solution of the problem. We then chose a finite-dimensional subspace V^h of $\boldsymbol{H}^1(\mathrm{curl};\Omega)$, dependent on a real parameter h called *discretization step*, in such a way that for $h \to 0$, V^h is dense in $\boldsymbol{H}^1(\mathrm{curl};\Omega)$. Calling $\boldsymbol{W}_i$ the basis functions of V^h, a function $\boldsymbol{E} \in \boldsymbol{H}^1(\mathrm{curl};\Omega)$ can be written as:

$$\boldsymbol{E} = \sum_{i=1}^{N} e_i \boldsymbol{W}_i + \boldsymbol{R} \tag{4.22}$$

where R is the component of $\boldsymbol{E}$ orthogonal to V^h (that cannot be expressed as linear combination of $\boldsymbol{W}_i$). According to Galerkin's method, the approximated solution we are looking for is the function in V^h that minimizes the distance to the actual solution in $\boldsymbol{H}^1(\mathrm{curl};\Omega)$; in other terms, the residual must be orthogonal to V^h, and therefore

$$\boldsymbol{R} = \boldsymbol{r}. \tag{4.23}$$

From here follows that the scalar product of r with each basis function of V^h is zero:

$$(\boldsymbol{W}_i, \boldsymbol{r})^2 = \int_\Omega \boldsymbol{W}_i \cdot \boldsymbol{r} = 0 \quad \text{for } i = 1, \ldots, N. \tag{4.24}$$

Substituting Eq. (4.21) in Eq. (4.24), and recalling that we are looking for a solution $\boldsymbol{E}^h \in V^h$, we obtain

$$\sum_{j=1}^{N} \int_\Omega \Big(\boldsymbol{W}_i \cdot \hat{\Phi} \boldsymbol{W}_j + \omega_p^2 \boldsymbol{W}_i \cdot \boldsymbol{W}_j \Big) e_j = \sum_{j=1}^{N} \int_\Omega \big(\omega^2 \epsilon_0 \epsilon \boldsymbol{W}_i \cdot \boldsymbol{W}_j \big) e_j. \tag{4.25}$$

The vector of complex coefficients e_i is the unknown of the numerical method. In matrix form:

$$M_{ij}\ e_j + OP_{ij}\ e_j = \omega^2 F_{ij}\ e_j, \tag{4.26}$$

where the implicit summation convention is used (with j running from 1 to N), and

$$\begin{aligned} M_{ij} &= \int_\Omega \left(\frac{1}{\epsilon_0} \nabla \times \boldsymbol{W}_i \cdot \frac{1}{\mu_0} \nabla \times \boldsymbol{W}_j \right), \\ OP_{ij} &= \int_\Omega \omega_p^2 \, (\boldsymbol{W}_i \cdot \boldsymbol{W}_j), \\ F_{ij} &= \int_\Omega (\epsilon_0 \epsilon \boldsymbol{W}_i \cdot \boldsymbol{W}_j) \end{aligned} \tag{4.27}$$

The problem has been converted to a common generalized eigenvalue problem for the matrices $(M + OP)$ and F. The OP and F matrices are Hermitian positive-definite, since they are obtained from scalar products, while M is Hermitian positive-semidefinite if $\hat{\Phi}$ is an Hermitian (self-adjoint) operator, as (in our case) indeed it is. Once the eigensolutions e_i have been determined, the Galerkin's solution (in V^h) can be retrieved using the basis of V^h:

$$\boldsymbol{E}^h = \sum_{i=1}^{N} e_i \boldsymbol{W}_i. \tag{4.28}$$

A suitable choice of the basis functions can give physical meanings to the coefficients e_i. The usual procedure is to subdivide the domain Ω in a finite collection, called *mesh*, of subdomains Ω^k, that entirely cover the domain without overlap. Therefore, the integrals in (4.27) can be split in sums of the integrals over each mesh elements. In the most common implementation of the FEM, a finite collection of N points in Ω is constructed (the *mesh nodes*). The subspace V^h is $3N$-dimensional, and the $3N$ basis functions are chosen as

$$\boldsymbol{W}_i^k = f_i \hat{e}_k, \quad \text{for } i = 1, \ldots, N \quad \text{and } k = x, y \text{ or } z \tag{4.29}$$

where f_i is a scalar function with unitary value on the i-th node and null value on the other nodes, and $\hat{e}_k$, with $k = x, y$ or z, is the unit vector in the x, y or z direction, respectively. In this case, the coefficient e_i^k has the physical meaning of being the value of the k-component of the electric field on the i-th node of the mesh. This approach (the *Nodal elements*) is very useful and extensively employed in many applications, but suffers of some issues in the case of electromagnetic problems, such as the introduction of spurious modes. The approach we chose is the *Edge Elements* method, in which the e_i coefficients have the physical meaning of value of the component of the electric field on the i-th edge in tangential direction. The basis functions, therefore, must be chosen such that $\boldsymbol{W}_i$ has constant tangential component along the i-th edge and no tangential component along all the other edges. The advantages of this choice of basis elements are the following [52]:

- no spurious modes are introduced in the solution;
- interface conditions between dielectric (continuity of $\boldsymbol{E} \times \hat{n}$) are automatically satisfied providing that the interface is lying along an edge or face;
- PEC boundary conditions ($\boldsymbol{E} \times \hat{n} = 0$) are easily implemented simply removing the corresponding coefficients e_i from the discrete problem.

According to the theory presented, for a number N of edges (and an N-dimensional subspace V^h) only N basis function are needed. However, since the integrals in Eqs. (4.27) can be split in sums of integrations over each mesh element, the *elemental matrices* can be introduced,

$$\begin{aligned} M_{ij}^k &= \int_{\Omega^k} \left(\frac{1}{\epsilon_0} \nabla \times \boldsymbol{W}_i \cdot \frac{1}{\mu_0} \nabla \times \boldsymbol{W}_j \right), \\ OP_{ij}^k &= \int_{\Omega^k} \omega_p^2 \, (\boldsymbol{W}_i \cdot \boldsymbol{W}_j), \\ F_{ij}^k &= \int_{\Omega^k} (\boldsymbol{W}_i \cdot \boldsymbol{W}_j), \end{aligned} \tag{4.30}$$

and the original matrices M_{ij}, OP_{ij} and F_{ij} can be recovered by summation over all the elements Ω^k. The matrices obtained are very sparse, as the element ij is nonzero only if the edges i and j belong to the same element. The

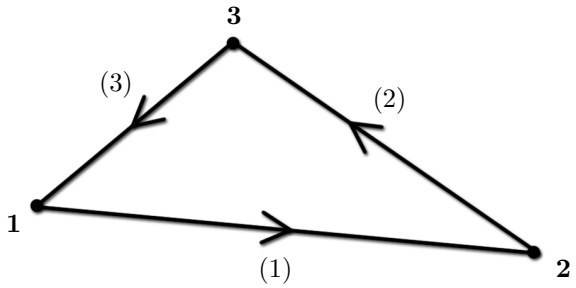

Figure 4.4: Vertices and edge numbering for a triangular 2D element.

evaluation of the matrices depends on the problem and the choice of basis functions. Our implementation focuses on triangular (2D) and tetrahedral (3D) meshes. The following two subsections cover the discretization procedure for the two cases.

4.3.1 Two-Dimensional Problems

In a Two-Dimensional problem, the domain is subdivided into a collection of N_t triangles that cover it entirely, without overlapping, and with the condition that each edge must belong at most to two triangles. The vertices are ordered counterclockwise, as in Fig. 4.4; the area of the triangle can therefore be computed as a determinant:

$$A^e = \frac{1}{2}\begin{vmatrix} 1 & x_1 & y_1 \\ 1 & x_2 & y_2 \\ 1 & x_3 & y_3 \end{vmatrix}, \tag{4.31}$$

where (x_i, y_i) are the coordinates of the i-th node.

To define the basis functions for the triangular edge elements, we first define the linear interpolation functions L_i within a triangle. These function have unitary value in the vertex i of the triangle, and null value on the other vertices. They can be used as basis function for a node-based FEM, but we will use them to construct the basis for the edge-element approach. The function $L_i(\boldsymbol{x})$ is defined as the area of the triangle obtained taking $\boldsymbol{x}$ instead of the node $\boldsymbol{x}_i$, if $\boldsymbol{x}$ is inside the element, and zero otherwise. More specifically, remembering Eq. (4.31), one can write

$$L_1(x,y) = \begin{cases} \frac{1}{2}\begin{vmatrix} 1 & x & y \\ 1 & x_2 & y_2 \\ 1 & x_3 & y_3 \end{vmatrix}, & \text{if } \boldsymbol{x} \text{ inside the triangle} \\ 0, & \text{otherwise,} \end{cases} \tag{4.32}$$

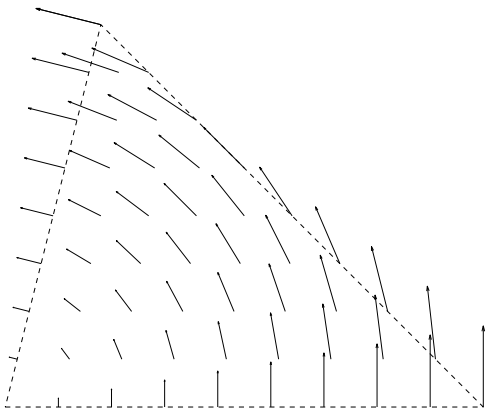

Figure 4.5: Vectorial basis element relative to the top right edge. The vectorial function has constant tangential component on that edge and is orthogonal to the other two.

and similarly for L_2 and L_3.

From the linear interpolation function we can construct the vector basis functions for the triangular edge element. The requirements for the basis function $\boldsymbol{W}_{ij}$ (relative to the i-j edge) are:

- the tangential component along the i-j edge must be constant;
- the tangential component along the other edges must be null.

The basis vector functions used are:

$$\boldsymbol{W}_{ij} = L_i \nabla L_j - L_j \nabla L_i, \tag{4.33}$$

an example of which is represented in Fig. 4.5, that have the following properties:

- the tangential component on the i-j edge is $1/l_{ij}$, where l_{ij} is the length of the edge;
- the orthogonal component on the i-j edge is null on the foot of the altitude relative to that edge;
- is orthogonal to the other edges;
- is null on the vertex not belonging to the i-j edge.

These functions are therefore suitable basis functions for the triangular edge elements. Furthermore, they can be normalized according to:

$$\boldsymbol{N}_{ij} = l_{ij} \boldsymbol{W}_{ij}. \tag{4.34}$$

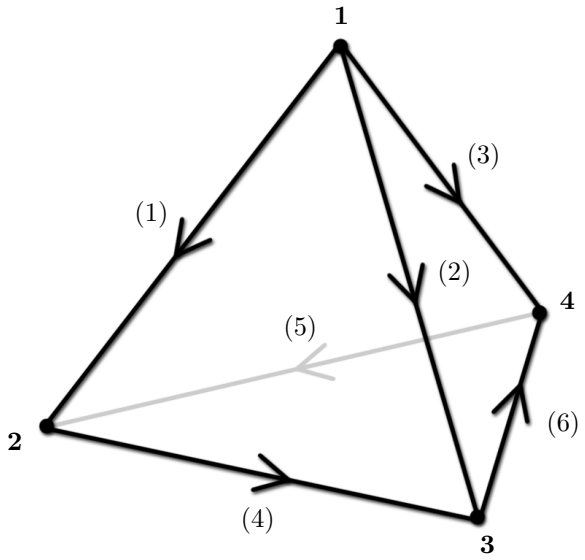

Figure 4.6: Vertices and edge numbering for a tetrahedral 3D element.

Once the basis functions have been defined, the elemental matrices can be evaluated. Using the basis functions (4.33), the integrals in Eqs. (4.30) can be evaluated analytically. The matrices M, OP and F are obtained by summation over each element, taking into account the relative edge orientations. Since each edge is at most shared by two triangles, we expect each row and column of the matrices to have at most 5 nonzero elements.

4.3.2 Three-Dimensional Problems

For Three-Dimensional problem, we employed tetrahedral elements. The node and edge numbering follows the scheme presented in Fig. 4.6. The volume of the tetrahedron can be computed as a determinant as well:

$$V^e = \frac{1}{6}\begin{vmatrix} 1 & x_1 & y_1 & z_1 \\ 1 & x_2 & y_2 & z_2 \\ 1 & x_3 & y_3 & z_3 \\ 1 & x_4 & y_4 & z_4 \end{vmatrix}. \tag{4.35}$$

The construction of the basis function for the tetrahedral element follows the one for the triangular element. We therefore define the linear interpolation function $L_i(\boldsymbol{x})$ as the volume of the tetrahedron defined by substituting the i-th vertex with $\boldsymbol{x}$ in the original element, if $\boldsymbol{x}$ is in the element, and 0 otherwise, and the vectorial basis function $\boldsymbol{W}_{ij}$ as in Eq. (4.33). In this case, the basis function have the following properties:

- the component tangential to the i-j edge is constant and equal to $1/l_{ij}$;

- the component orthogonal to the i-j edge is zero on the point of minimal distance from the opposite edge;
- is null on the opposite edge;
- is orthogonal to all the other edges.

As in the two-dimensional case, the evaluation of the elemental matrices can be done analytically with this choice of basis function. The matrices M, OP and F can be computed by summing on all the elements Ω^k, taking into account the edge orientations. The number of nonzero elements of the resulting matrices cannot be predicted, as the number of tetrahedra sharing each edges is unknown, but in general the matrices obtained for 3D problems are more populated than the 2D ones, requiring an increased computational effort for the solution.

4.3.3 Boundary Conditions

To enforce boundary conditions for the FEM we will follow a reduction matrix approach, as done for the FDM in Sect. 4.2.3. The two types of boundary conditions implemented are Perfect Electric Conductor (PC) and Bloch-periodicity. The construction and the application of the reduction matrix R is identical to the one presented in Sect. 4.2.3.

4.3.4 Divergence Constraint

A discrete Divergence matrix can in principle be obtained for a Galerkin's formulation of the problem, i.e. expanding the divergence constraint on the basis of V^h. However, we here follow another approach, presented in [53]. The functions we are considering for our problem belong to $\boldsymbol{H}^1(\mathrm{curl};\Omega)$. We consider the divergence and gradient operators:

$$\begin{aligned} \nabla\cdot\bullet \ &: \ \boldsymbol{H}^1(\mathrm{curl};\Omega)\rightarrow H^1(\Omega), \\ \nabla\bullet \ &: \ H^1(\Omega)\rightarrow \boldsymbol{H}^1(\mathrm{curl};\Omega), \end{aligned} \tag{4.36}$$

The space $H^1(\Omega)$ can be regarded as the space of the electrostatic scalar potentials ϕ. We chose V^h, that is, the n_e-dimensional space of edge-valued vector fields on a mesh, as a discretization of $\boldsymbol{H}^1(\mathrm{curl};\Omega)$; a natural discretization of the $H^1(\Omega)$ space is therefore the n_n-dimensional space of nodal-valued scalar fields on the same mesh, that we call N^h. In this case, the discrete gradient operator $G \ : \ N^h \rightarrow V^h$ is easily defined as the $n_e \times n_n$ matrix that computes the gradient along each edges, given the value of the potential at each node. The k-th row of G (relative

to the k-th edge, defined by the nodes i and j) is:

$$\begin{aligned} G_{ki} &= -l_k \\ G_{kj} &= l_k \end{aligned} \tag{4.37}$$

where $l_k = |\boldsymbol{x}_j - \boldsymbol{x}_i|$ is the length of the edge. The columns of the gradient matrix G span a subspace of V^h that is the *Range* of G, in other words, the functions of V^h that can be written as a linear combination of the columns of G can be regarded as the gradient of some scalar (electrostatic) potential ϕ. Since the divergent modes that we want to eliminate correspond to eigenfrequencies of 0 (in free-space) or ω_p (in the metal region), and remembering the vector identity

$$\nabla \times \nabla\phi = 0 \iff \text{Range}(\nabla\bullet) = \text{Kernel}(\nabla \times \bullet), \tag{4.38}$$

it is clear that the columns of G span the subspace of divergent modes that we want to eliminate (we emphasize that the number of linearly independent columns in G is the same of the number of the free nodes in the mesh citevenkatarayalu, therefore *all* the divergent modes are in the subspace spanned by the columns of G). The non-divergent modes must then be orthogonal to the range of G, that is:

$$G_{ij}F_{jk}e_k = 0, \tag{4.39}$$

where the implicit summation convention is used. The sought constraint matrix D is obtained simply as:

$$D = G^T F. \tag{4.40}$$

We point out that D is not the discrete divergence matrix, that is, the matrix obtained discretizing the divergence operator on V^h. The fundamental point is that the columns of D span the range of the discrete divergence operator, and therefore can be used to enforce the divergence constraint.

The matrix D must be subjected to the boundary conditions, for example using the reduction matrix method:

$$D_b = DR \tag{4.41}$$

4.4 Implementation

In this work, the numerical method presented in the previous sections have been implemented in `MATLAB`, to take advantage of the sparse matrix functions and tools provided by this environment. In this section we will briefly discuss some aspects of the implementation relevant to this work.

4.4.1 Mesh Construction

For the design of the two- and three-dimensional meshes required for the two- and three-dimensional problems, the `COMSOL` Multiphysics software package has been used. The meshes designed are then exported to a text file (with extension `.mphtxt`), that is successively imported in `MATLAB` using a custom function. The edge-focused nature of the method require a careful treatment of the edges: the information about the points, the bounded triangles or tetrahedra and the orientations must be stored for each edge.

4.4.2 Interpolation and Postprocessing

The vectors of complex values e_i represent the magnitude of the electric field along each edge. To graphically visualize the shape of the fields, a process of interpolation must be performed.

For two-dimensional problems (with TE polarization), the value of the z component of the magnetic field H_z is commonly used when plotting. For each triangle, in order to compute an approximation of H_z, we used Stokes' Theorem,

$$\int_{\partial\Omega^k} (\boldsymbol{E} \cdot d\boldsymbol{l}) = \int_{\Omega^k} (\nabla \times \boldsymbol{E} \cdot \hat{n}); \tag{4.42}$$

one of Maxwell's equations in the frequency domain,

$$i\omega \boldsymbol{H} = \frac{1}{\mu_0} \nabla \times \boldsymbol{E}, \tag{4.43}$$

recalling that the tangential component of each vector basis function has the constant value $1/l_j$ along the j-th edge; and assumed H_z constant in the k-th triangle; obtaining the following formula:

$$H_z^k = -i \frac{1}{A^k \omega \mu_0} \sum_{j=\text{edges}} e_j l_j \tag{4.44}$$

where the sum is carried over the three edges, with the correct orientation. The factor $-i$ only contributes with a phase shift, while the factor $\frac{1}{\omega\mu_0}$ can be disregarded if only the shape of the field is of interest (as it commonly is). A matrix can be constructed from Eq. (4.44) to compute the value of H_z for each triangle, and `MATLAB`'s built in functions (from the `PDE` toolbox) can be used to plot the result.

For three-dimensional problems, a custom interpolation function has been implemented. Given a collection of points of interest $\{\boldsymbol{x}_i\}$ (for instance, a rectangular grid), for each point $\boldsymbol{x}_i$ the function identifies the tetrahedron containing it, and the value of the electric field is computed interpolating the values on the edges of the tetrahedron with the vector basis functions $\boldsymbol{W}_j$:

$$\boldsymbol{E}(\boldsymbol{x}_i) = \sum_{j=\text{edges}} e_j \boldsymbol{W}_j(\boldsymbol{x}_i). \tag{4.45}$$

The result of this process is a collection of the values $\{\boldsymbol{E}_i\}$ of the electric field on the points $\{\boldsymbol{x}_i\}$, that can be plotted with `MATLAB`'s functions for 3D plots, such as `slice`.

Chapter 5

Eigensolvers

5.1 Introduction

In Chap. 3 we formulated the physical problems we want to solve. In Chap. 4 we presented the discretization schemes that we used to convert a differential problem into a matrix problem. In the present chapter, we will discuss the an essential, somewhat standalone part of the solving process, that is the algorithms for calculating the eigenvalues of a matrix problem. We will start by explaining and discussing the eigensolver algorithms in the following section.

5.2 Eigensolvers

An eigensolver is an algorithm whose purpose is to find approximations $(\tilde{\lambda}, \tilde{x})$ of the eigenpairs (λ, x) solutions of the generalized eigenvalue problem

$$Mx = \lambda Fx, \tag{5.1}$$

where M and F are two finite-dimensional square matrices, within a specified tolerance ϵ, such as

$$\left| M\tilde{x} - \tilde{\lambda} F\tilde{x} \right| \leq \epsilon. \tag{5.2}$$

In this work, the matrices M and F have always the following characteristics:

- For the **FiniteDifference Method**, M is sparse, Hermitian positive-semidefinite, since it is produced from the discretization of an Hermitian differential operator and its eigenvalues (ω^2) are positive or null; while F

is the identity matrix. In addition, since the discretization is carried on a regular (rectangular) grid, the M matrix has a known sparsity pattern.

- For the **Finite-Element Method** method, M is sparse, Hermitian positive-semidefinite, but its sparsity pattern is dependent on the mesh, and it is therefore different for each problem. The F matrix is sparse and Hermitian positive-definite as well.

In the scope of the present work, we will focus on algorithms suited to these characteristics (sparse, Hermitian matrices). We analyzed two different algorithms for the solution of the generalized eigenvalue problem, `ARPACK` and `LOBPCG`, based on two different mathematical approaches.

5.2.1 ARPACK

`ARPACK` (ARnoldi PACKage) [54–57] is a collection of Fortran77 subroutines designed to solve large scale eigenvalue problems. The user is required to supply interface functions that provide communication with these libraries. Mathematically, they are based on the Arnoldi algorithm [55], that we present here in its simplest form. Given a matrix M and an arbitrary starting vector v, we consider the succession of vectors

$$\begin{aligned} x_0 &= v, \\ x_n &= M x_{n-1} \end{aligned} \tag{5.3}$$

that span a subspace called *Krylov subspace*. For numerical implementations, due to stability issue, the vectors in the succession are orthonormalized (for instance using the Gram-Schmidt process). The succession can be computed until the n-th orthonormalized vector is null or has a norm smaller than the assigned tolerance; in this case, the $(n-1)$-th vector is (an approximation of) an eigenvector, the one corresponding to the largest magnitude eigenvalue. An extension of the algorithm is to construct a matrix H_k that is the orthogonal projection of M over a k-dimensional Krylov subspace (dependent on the choice of the starting vector), with the transformation matrix obtained from the orthonormal Krylov vectors, and then computing the eigenvalues of H_k, that are called *Ritz approximations* of the eigenvalues of M, using QR factorization. A more specific description of the algorithm can be found in the references [55, 57] and is beyond the scope of this work. For Hermitian matrices (as in our case), the Arnoldi algorithm reduces to the Lanczos algorithm [55], that produces a tridiagonal matrix T_k instead of H_k.

The `ARPACK` package is built on the Arnoldi algorithm, and thus naturally computes the largest magnitude eigenvalues. Unfortunately, when computing the photonic band structure of a periodic metamaterial, the eigenfrequencies of interest are usually the ones around zero. Moreover, as explained in Sects. 3.2 and 5.2, the failure in

implementing the divergence Maxwell's equations in the discetization procedure introduces a large number (dependent on problem size) of eigenvalues equal to zero and ω_p, while the eigenfrequencies required lie between these two values. To compute the eigenvalues around the frequency of interest σ, a method called *Shift-and-Invert* is used, that consist in solving a different eigenvalue problem:

$$(M - \sigma F)^{-1} Fx = \nu x, \quad \text{where } \nu = 1/(\lambda - \sigma). \tag{5.4}$$

The advantage of this transformation is that for the problem (5.4) the eigenvectors corresponding to the eigenvalues ν of largest magnitude are also eigenvectors for the original problem (5.1), and correspond to the eigenvalues λ closer to the target frequency σ. The drawback of this method is that in this case the `ARPACK` packages requires a routine to solve the linear system

$$(M - \sigma F)\, x = b, \tag{5.5}$$

either by matrix factorization, or using an iterative method. For instance, in the `MATLAB` implementation of the `ARPACK` interface (that has been extensively used in this work), a LU factorization is performed, using massive amount of memory and thus hindering the possibility of using built-in `MATLAB` functions to solve large problems. Another problem of this approach is that the target frequency σ and the number of eigenvalues desired must be chosen very carefully, in order to avoid the unnecessary (and time-consuming) computation of the eigenvalues at 0 or ω_p. An obvious solution for this problem would be a custom implementation of an `ARPACK` interface, using an iterative solver for (5.5), such as the `PARDISO` sparse solver [58, 59], and enforcing the divergence-free Maxwell's equations as explained in Sect. 5.3. Due to the Hermitian nature of the problem, however, we chose an alternative method to obtain the eigenvalues of (5.1), as presented in the following subsection.

5.2.2 `LOBPCG`

`LOBPCG` (Locally Optimized Block Preconditioned Conjugate Gradient) is an eigensolver algorithm designed by Andrew Knyazev [60, 61]. It is an implementation of a Conjugate Gradient minimization of the Rayleigh quotient of the problem (5.1). The underlying mathematics is presented in the following. Given two Hermitian matrices M and F, with F in addition positive-definite, and the generalized eigenvalue problem

$$Mx = \lambda Fx, \tag{5.6}$$

the smallest magnitude eigenvalue λ_1 that solves (5.1) minimizes the *generalized Rayleigh quotient* of the two matrices M and F, for each vector x:

$$\lambda_1 \leq \frac{(x, Mx)}{(x, Fx)}, \quad \forall x, \tag{5.7}$$

with the equal sign valid in the case $x = x_1$ is the eigenvector corresponding to λ_1. Remembering that the generalized eigenvectors of an Hermitian matrix are F-orthogonal, it can be easily proved that the n-th smallest eigenvalue λ_n satisfies

$$\lambda_n \leq \frac{(x, Mx)}{(x, Fx)}, \quad \forall x \perp x_1, x_2, \dots x_{n-1}. \tag{5.8}$$

It is therefore possible to compute a *block* of eigenvalues and eigenvector at once, by minimizing each Rayleigh quotient while maintaning orthogonality among the considered vectors. This, from a computational point of view, is an advantage, as explained later. The minimization procedure itself is carried with a Conjugate Gradient method, that finds the minimum of a function searching in the matrix-conjugated directions.

As presented in Sect. 3.2 and further in Sect. 5.2, the eigenproblems we are dealing with in this work have a great number of eigenvalues at zero frequency. To obtain the true (physical) frequencies, it is necessary to enforce the divergence-free condition on the eigenvectors. This can be done in `LOBPCG` by maintaining the vectors in the block F-orthogonal to a suitable divergence matrix D, whose construction is described in Sect. 4.2.4 and Sect. 4.3.4. At every iteration of the Conjugate Gradient method, the block of vector is reorthogonalized, ensuring that the algorithm finds the smallest eigenvalues for the eigenvectors in the F-orthogonal complement of the subspace spanned by the columns of the matrix D.

The `LOBPCG` algorithm supports the use of a preconditioner, that is, given a positive-definite matrix T of the same size of M, it solves the equivalent eigenvalue problem:

$$TMx = \lambda TFx. \tag{5.9}$$

The aim of this procedure is to improve the condition number of the problem, thus reducing the number of iterations needed, at the cost of slightly increased number of operations for each iteration (because a multiplication by T must be performed) as well as some additional storage requirements. The preconditioner construction is presented and discussed in Sect 5.4.

5.3 Divergence Constraint

For both the FDM and the FEM approach, the matrices M and F are obtained by discretizing the curl Maxwell's equations. To avoid nonphysical modes with non-null divergence, the solutions must obey also the divergence Maxwell's equations. These can be discretized as a matrix D which is used to enforce the condition

$$DFx = 0 \tag{5.10}$$

for each vector x. The eigenvector found in this way will have null discrete divergence and will be therefore a valid discretization of the sought eigenfunctions. In our work, we applied the divergence constraint only when using the `LOBPCG` solver, while with `ARPACK` a careful choice of the target frequency σ allows the computation of the desired eigenvalues without enforcing the condition. The number of nonphysical modes with $\omega = 0$ is equal to the number of free nodes in air or dielectric regions [53]; therefore, the number of columns of D must be matched accordingly. We also enforced the divergence-free condition on the free nodes in the metal region, eliminating the eigenvalues at ω_p and slightly speeding up the convergence by restricting the subspace in which the eigenvectors must be looked for.

5.4 Preconditioning

A suitable preconditioning technique can dramatically improve the convergence rate of an iterative algorithm, by improving the condition number of the problem. A preconditioner T is a matrix, of the same size of M, that approximates in a certain sense the inverse M^{-1}. In this work we used a preconditioning technique called `FSPAI` (Factorized Sparse Approximate Inverse) [62]. The idea behind this algorithm is to find a matrix L_T, of given sparsity pattern, that minimizes $\|L_T L_M - I\|$, where L_M is a Cholesky factor of M, I is the identity matrix and the norm involved is the Frobenius norm:

$$\|A\| = \sqrt{\sum_i \sum_j a_{ij}^2}. \tag{5.11}$$

In practice, given the sparsity of L_T, the algorithm consists solving a least-square problem for the nonzero elements of each column of L_T; since both L_M and L_T are very sparse, this in turn consists in solving a number of small linear systems equal to the number of columns in the matrices. The size of those linear systems depend on the number of nonzero elements in each column of L_T, and therefore on the sparsity pattern chosen.

The FSPAI algorithm can be used in an adaptive way, by determining the elements of L_T that will most affect the Frobenius norm using a 1D-minimization on the elements of each column, and adding them to the sparsity pattern, in an iterative fashion, until the norm is below a given tolerance. However, in our implementation we determined that good results can be obtained even with a fixed sparsity pattern (for example, the pattern of M), saving some computation time.

Once L_T is obtained, the preconditioner is computed by taking $T = L_T L_T'$. The advantages of the `FSPAI` algorithm can be summarized as follows:

- the preconditioning matrix T obtained is definite-positive, and can be used with `LOBPCG`,

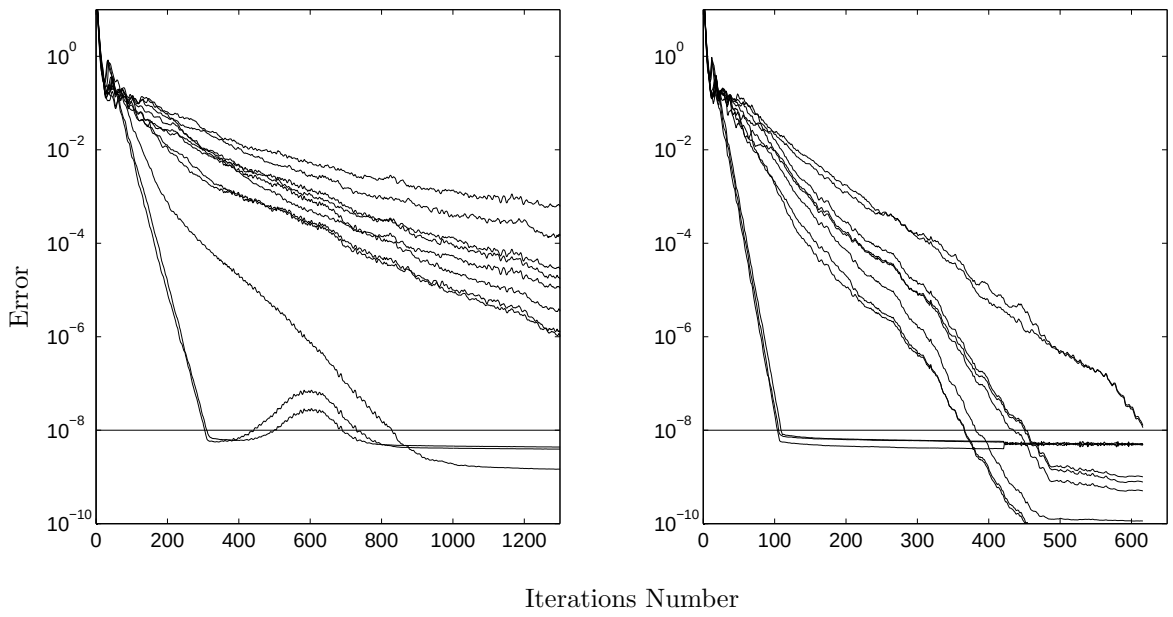

Figure 5.1: Convergence result for a block of 11 eigenvalues using the `LOBPCG` algorithm without (left) and with (right) preconditioning. The preconditioning clearly improves the convergence rate of the algorithm.

- the algorithm can be used even if M is positive-semidefinite, as in our case, and a conventional inverse M^{-1} does not exist. In this case, the aim of the preconditioner is to bring the eigenvalues of the product matrix TM as close to 1 as possible, rather than approximating the inverse,
- the possibility of using an arbitrary sparsity pattern allows to choose the amount of computation effort to put into the construction of the preconditioner.

Figure 5.1 presents an example of the effect of preconditioning.

Chapter 6

Simulation Results and Discussion

6.1 Introduction

In this chapter we will present some simulation results obtained with the numerical methods developed according to the previous chapters. We will compute the photonic band diagrams and the electromagnetic field distribution for some benchmark structures, and compare them with those obtained with other numerical or analytical methods. The aim of this chapter is to analyze the possibilities and potentialities of the method we developed; we will show how our results are in very good accordance with those obtained with other methods, opening the way to future applications of the algorithm to new and more complex structures. In the following sections, we will analyze first the FDM formulation,, presented in Sect. 4.2, for 2D problems. We will discuss the main issues that affect the effectiveness of this formulation, which in fact motivated us to the development of another numerical method. We will then analyze the FEM with Edge Elements, presented in Sect 4.3, both in the 2D and 3D formulation, and make comparisons with published results.

6.2 Finite-Difference Method

In this section, we will discuss the results obtained with the FDM formulation. This method presents a serious issue, to be discussed in Sect. 6.2.4, that limits its applicability in most of the cases of interest. No three-dimensional FDM simulations have been performed in the present work, since our focus was soon diverted to the FEM formulation instead.

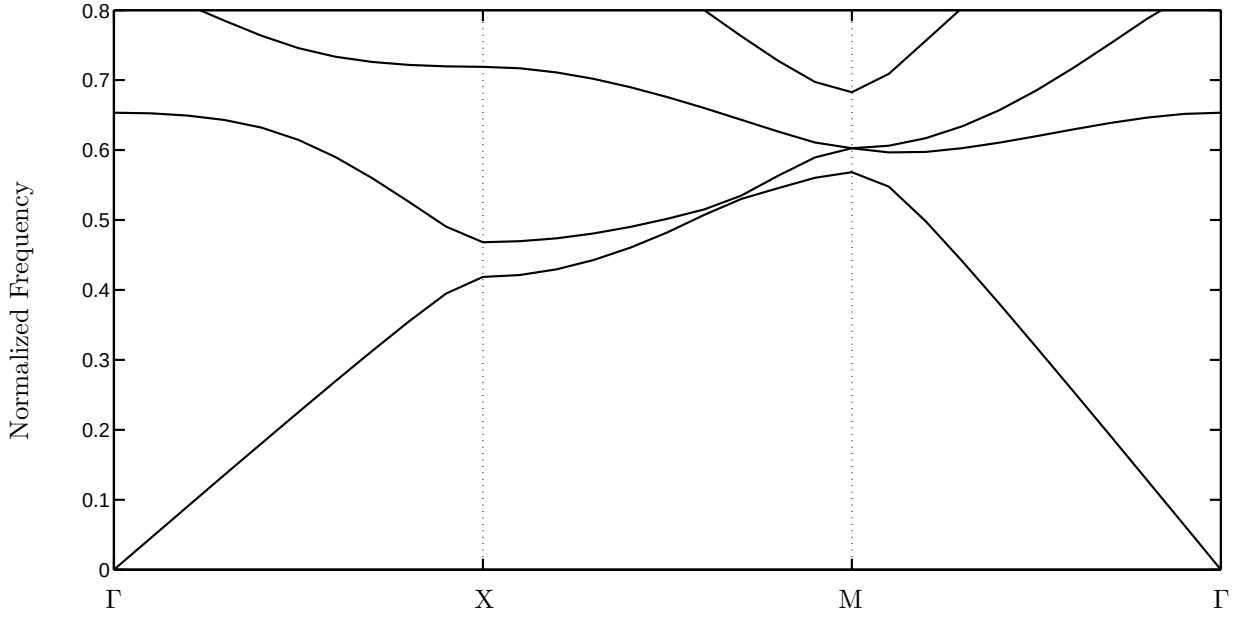

Figure 6.1: Photonic band diagram for a 2D square lattice of dielectric cylindrical rods, TE polarization, with $r = 0.2a$, $\epsilon = 8.9$ and grid size 50×50.

6.2.1 Dielectric Photonic Crystal

As first case, we compute the band structure of a periodic structure realized only with dielectric materials, in order to compare the result to the ones obtained with a freely available Frequency-Domain software, MPB (MIT Photonic Bands, [63, 64]), based on a Plane Wave Expansion method. The simulation parameters are:

- Relative Dielectric Permittivity: $\epsilon_r = 8.9$ (alumina);
- Cylinder radius: $r = 0.2a$;
- Spatial discretization: $n_x = n_y = 50$;
- Polarization: TE.

The complete photonic band diagram (Γ - X - M - Γ) is plotted in Fig. 6.1 and can be compared directly to the one in [5], page 68. This result is indeed a verification of how the method can simulate conventional dielectric photonic crystals as well.

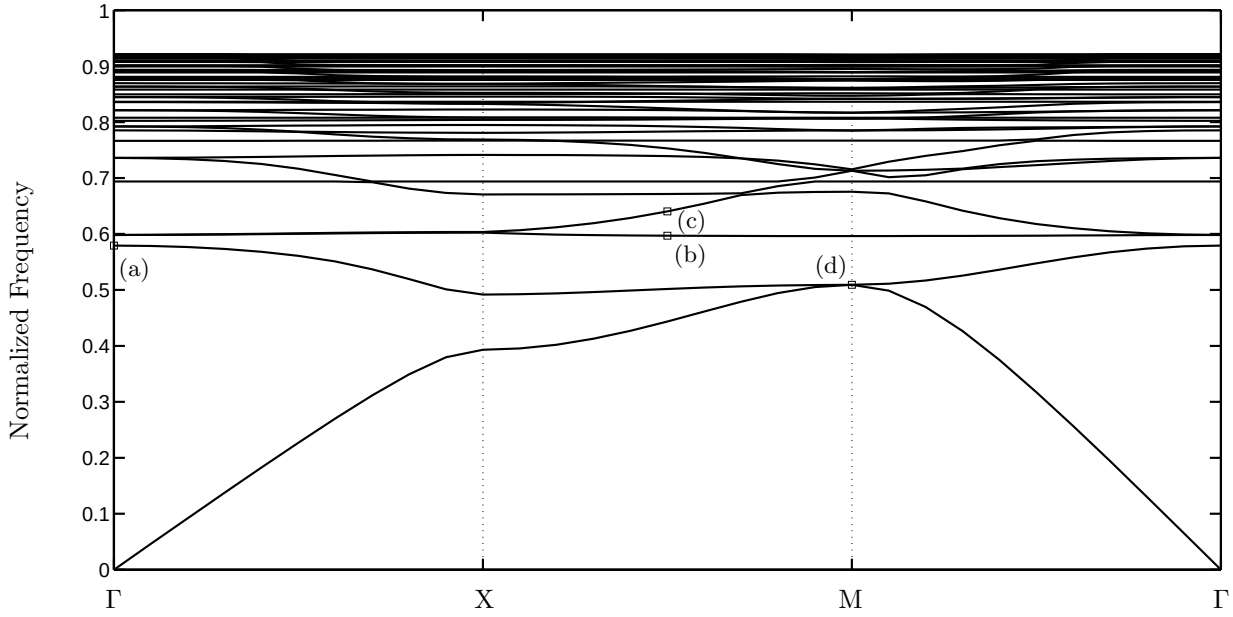

Figure 6.2: Photonic band diagram for a 2D square lattice of metallic square rods, TE polarization, with $r = 0.3a$, $\omega_p^N = 1$ and grid size 50×50. Fig. 6.3 presents the field plots for the modes marked with the letters a-d.

6.2.2 Square Lattice of Square Rods

We applied the FDM algorithm to the problem of determining the band structure of a square lattice of square rods. The simulation parameters are the following:

- Normalized Plasma Frequency: $\omega_p^N = 1$;
- Rod Side length: $r = 0.3a$;
- Spatial discretization: $n_x = n_y = 50$;
- Polarization: TE.

The band structure is presented in Fig. 6.2. A characteristic feature of the band diagrams obtained with Auxiliary Fields Formulation is immediately evident: the great number of flat bands that populate the frequency range above $\omega_p/\sqrt{2} = 0.71$. This is to be discussed in detail in Sect. 6.4.1. Fig. 6.3 is the plot of the real part of the H_z component of the magnetic field.

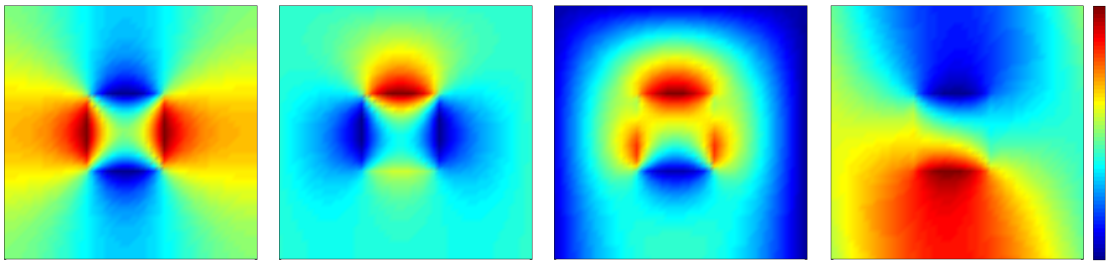

(a) (b) (c) (d)

Figure 6.3: Plots of the normalized H_z field for the modes marked in Fig. 6.2.

6.2.3 Square Lattice of Cylinders

We simulated a square lattice of cylindrical rods, with simulation parameters:

- Normalized Plasma Frequency: $\omega_p^N = 1$;
- Cylinder radius: $r = 0.2a$;
- Spatial discretization: $n_x = n_y = 50$;
- Polarization: TE.

The corresponding band diagram is presented in Fig. 6.4. We compared the band diagram with results obtained with a FDTD method, published in [50]. Although the dispersion relation for lower-frequency bands agree and the modes present the symmetries expected (Fig. 6.5a-b present some examples), the band diagram is polluted by flat, "fictitious" bands noticeably below $\omega_p/\sqrt{2} \simeq 0.71$. With FDM, the circular shape of the rod must be approximated on the rectangular grid with a staircase; by examining the field plot for the flat bands, it is evident that most of those modes are localized in the grid squares adjacent to the staircases. These fictitious modes not only give rise to nonphysical flat band, but also couple with the physical bands structure when the symmetry allows, polluting the results. Fig. 6.5c-d present two example of these fictitious modes. This issue is to be discussed in more detail in the next Section.

6.2.4 Fictitious Modes

In the results of our simulations using FDM we found a great number of flat bands that are not confirmed by other simulation methods. The flatness of the bands (independence from the $\boldsymbol{k}$ vector) indicates that the corresponding

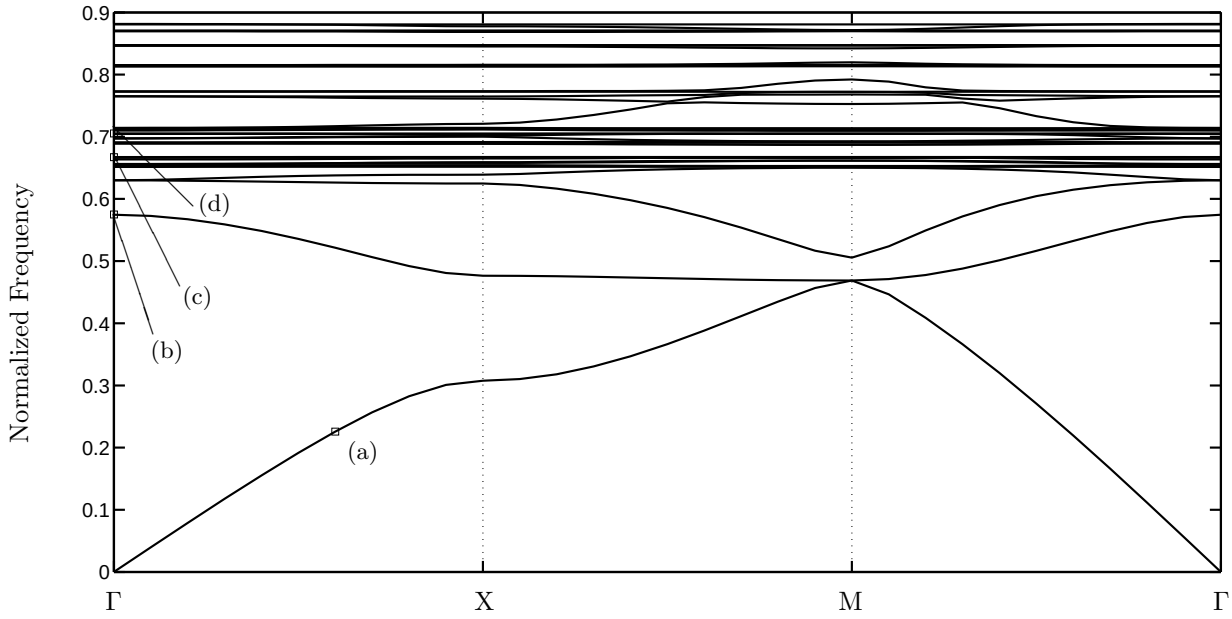

Figure 6.4: Photonic band diagram for a 2D square lattice of metallic cylindrical rods, TE polarization, with $r = 0.3a$, $\omega_p^N = 1$ and grid size 50×50. Fig. 6.5 presents the field plots for the modes marked with the letters a-d. The normalized frequency region around 0.7 is polluted with numerous "fictitious" flat bands (Figs. 6.5c-d).

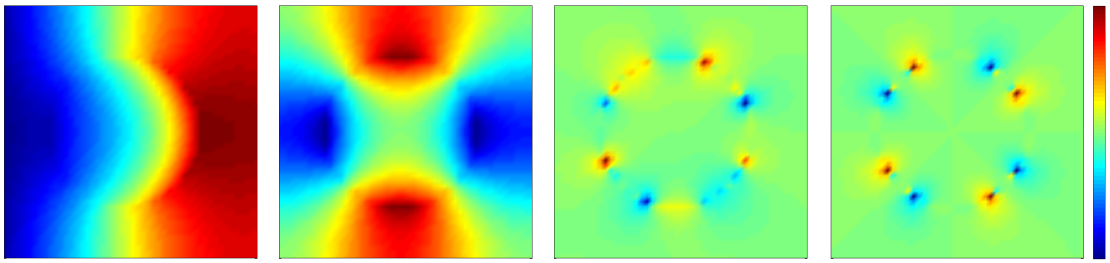

(a) (b) (c) (d)

Figure 6.5: Plot of the normalized H_z field for the modes marked in Fig. 6.4. (a)-(b) present two example of lower order modes, correctly computed. (c)-(d) are examples of the "fictitious" modes occurring in FDM simulations, discussed in Sect. 6.2.4

modes are highly localized and not coupled across the unit cell. Inspection of the field plots confirmed this assumption, showing that those modes are strongly localized on the metal-dielectric interface, in most case restricted to few grid cells, regardless of the resolution (an example is presented in Fig. 6.5c-d). Further simulations with different shapes and coordinate systems have been carried, in order to obtain an interpretation of this behavior. We determined that these localized modes are supported by those grid cells on the interface in which more than one but less than all the four edges are chosen as metallic grid points (in which $\omega_p \neq 0$). This naturally occurs when dealing with non-squared shapes (for example, with the cylindrical rods presented in Sect. 6.2.3) that require a staircase approximation in order to be simulated on a rectangular grid.

6.3 Finite-Element Method with Edge Elements

In this section we will present and discuss the results obtained with the Finite-Element Method, presented in Sect. 4.3. The main motivation that led us into developing this method is the limitation posed on the effectiveness of the FDM approach, namely the fictitious mode problem, exposed in Sect. 6.2.3 and commented in Sect. 6.2.4. We will show how the FEM is not affected by this issue and can indeed be used to simulate even complex structures and shapes.

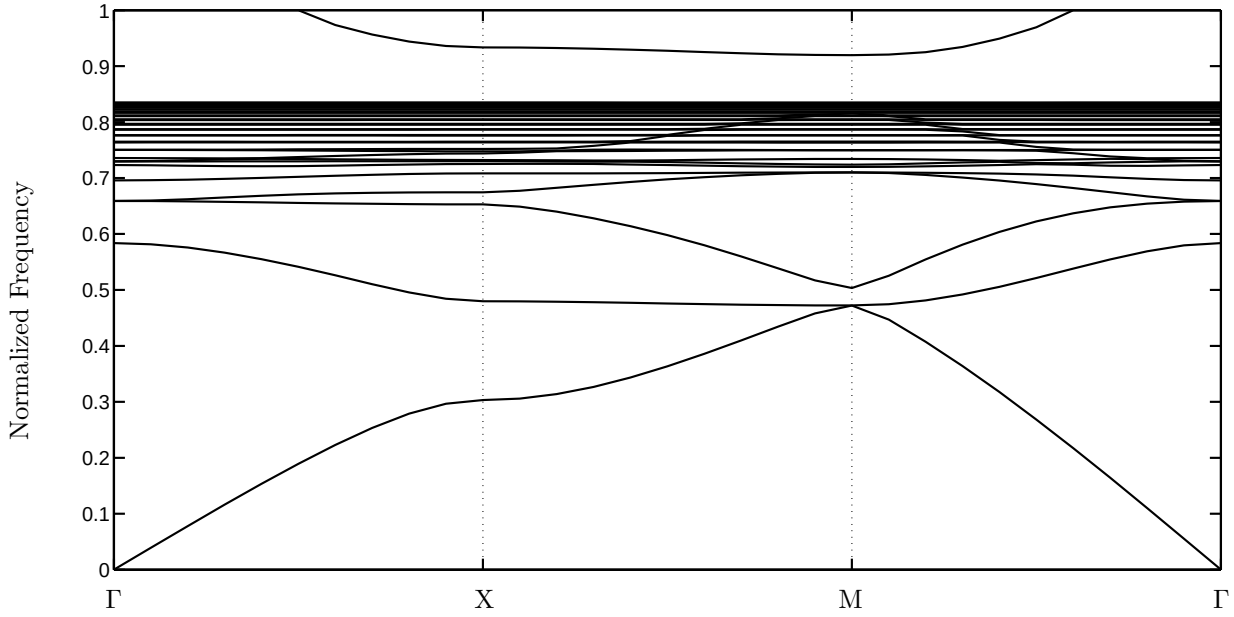

Figure 6.6: Photonic band diagram for a 2D square lattice of metallic cylindrical rods, TE polarization, with $r = 0.3a$, $\omega_p^N = 1$, obtained with the FEM.

6.3.1 Square Lattice of Cylinders

To verify the better performance of the FEM method, we will simulate the same structure in Sect. 6.2.3, that gave problems with the FDM formulation, and show that the results can be compared with FDTD simulations in [50] for higher frequency modes as well. The simulation parameters are:

- Normalized Plasma Frequency: $\omega_p^N = 1$;
- Cylinder radius: $r = 0.2a$;
- Spatial discretization: $n_x = n_y = 50$;
- Polarization: TE.

The photonic band diagram is presented in Fig. 6.6. The fictitious modes that populated the photonic band diagram obtained with FDM around $\omega_p/\sqrt{2} \simeq 0.71$ are absent in this case.

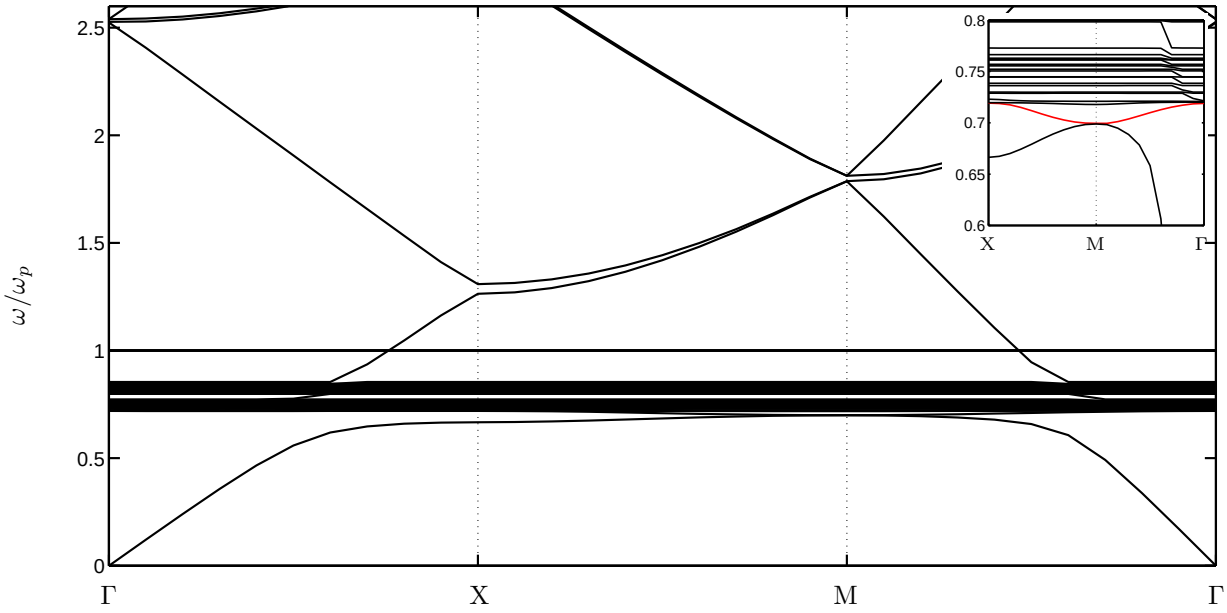

Figure 6.7: Photonic band diagram for a 2D square lattice of metallic cylindrical rods, TE polarization, with $r = 0.12a$, $\omega_p^N = 0.3963$. Due to the small filling factor of the structure, the modes can be classified in free-space-like (radiative) and surface modes (almost dispersionless). Inset: a closeup of normalized frequency range 0.6 – 0.8, that shows the correct computation of the dispersion relations at the M point.

6.3.2 Diluted Structure

In this section we will present the results of the simulation of a "diluted" structure, with metal/air filling factor of 0.041. The simulation parameters are:

- Normalized Plasma Frequency: $\omega_p^N = 0.3963$ (Silver);
- Cylinder radius: $r = 0.12a$;
- Polarization: TE.

Fig. 6.7 presents the complete photonic band diagram. Unlike the previous simulation, because of the low filing factor in this structure the modes can be easily classified in two categories: radiative free-space-like modes and almost-dispersionless surface modes. These results can be directly compared with the ones published in [65], obtained with FDTD methods. In particular, the dispersion relations of the lower order surface modes (as shown in the inset) are correctly simulated in the degeneracy at the M point, unlike in [65].

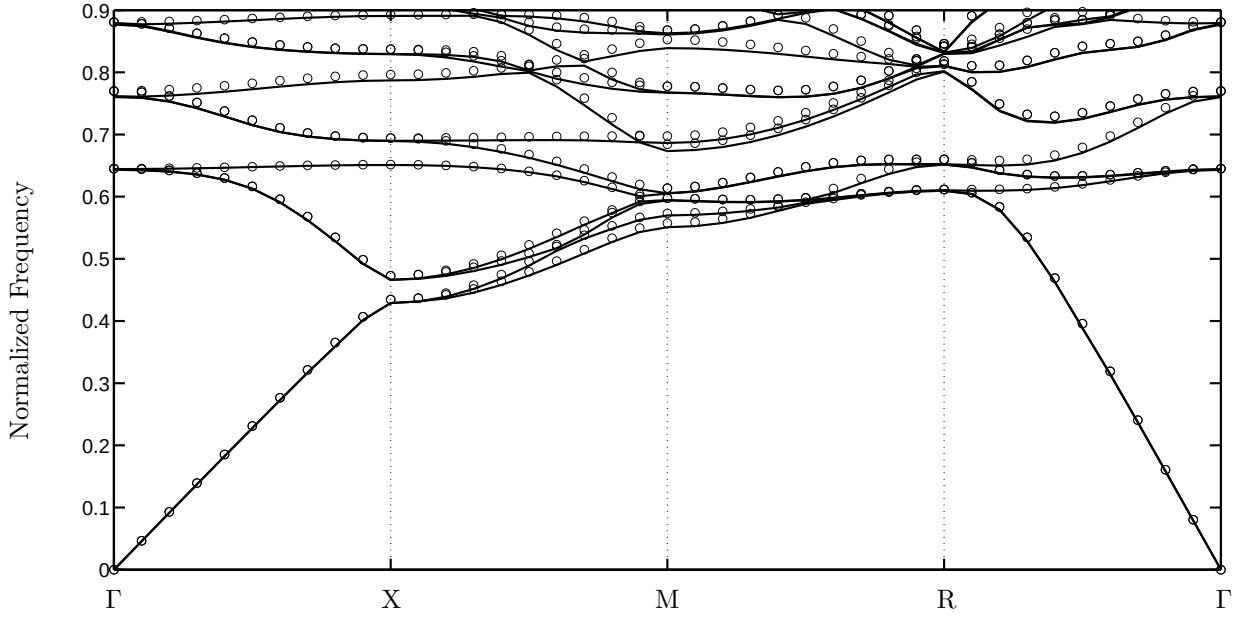

Figure 6.8: Photonic band diagram for a simple cubic lattice of dielectric spheres, with $r = 0.2a$ and $\epsilon_r = 9$. Solid lines: band diagram obtained with FEM. Circles: band diagram obtained with MPB.

6.3.3 3D Dielectric Photonic Crystal

As done with FDM, to verify the correct behavior of the 3D formulation we will start with computing the band structure of a three-dimensional dielectric photonic crystal and comparing our results with the ones obtained with MPB. The structure is a simple cubic lattice of spheres, with simulation parameters:

- Relative Dielectric Permittivity: $\epsilon_r = 9$;
- Sphere radius: $r = 0.25a$;
- Spatial discretization: 6463 nodes, 74088 edges;

The corresponding band diagram is plotted in Fig. 6.8, in which the results from FEM (solid line) and MPB (circles) can be directly compared, showing good accordance. The grid resolution used for MPB is $42 \times 42 \times 42$.

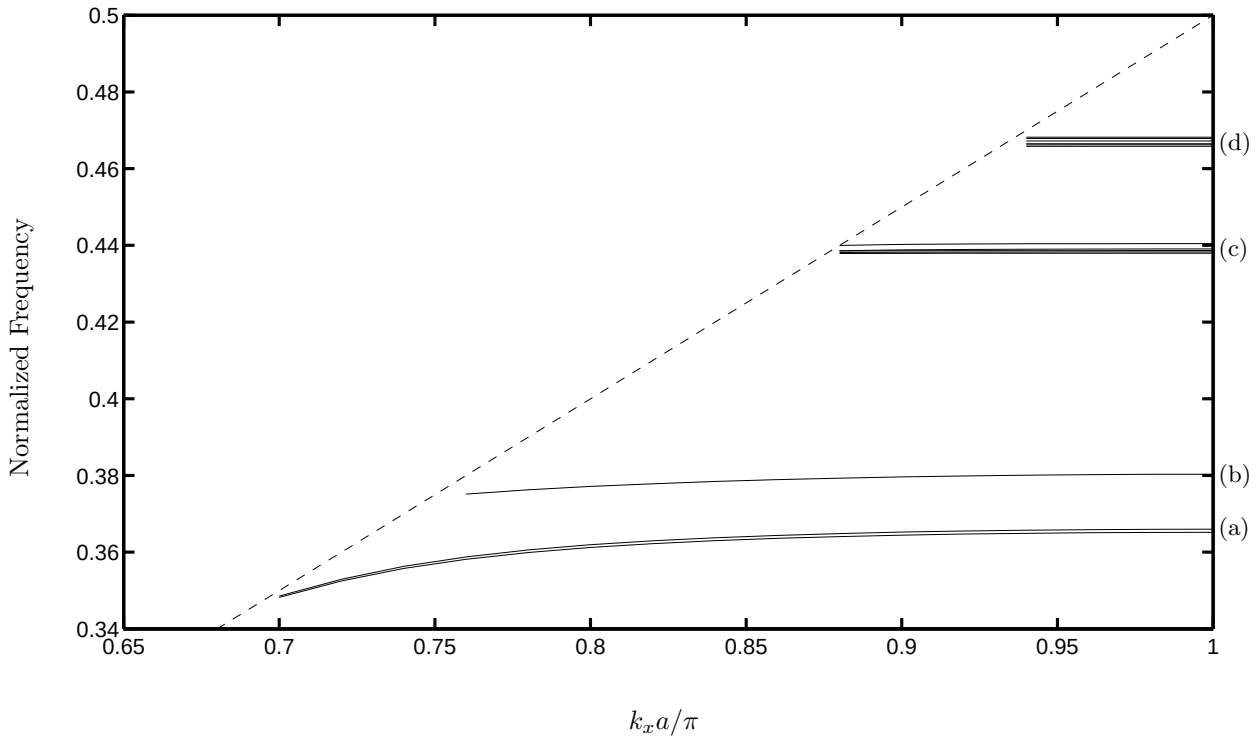

Figure 6.9: Dispersion relations for a chain of silver spheres with diameter 50 nm, spaced by 75 nm (Normalized parameters: $r \simeq 0.1852a$, $\omega_p^N = 0.672908$). The dashed line is the light cone, and only the guided modes are plotted. (a) Transverse dipolar excitation. (b) Longitudinal dipolar excitation. (c)-(d) Higher order multipolar excitations.

6.3.4 Linear Chain of Spheres

To simulate a linear chain of spheres (along the x direction), with one-dimensional periodicity, the problem of boundary conditions arise. Since our current implementation only allows two types of conditions (PC and Bloch-periodic), we chose a unit cell whose y and z dimensions are four times as large as the sphere spacing along x. The Bloch-periodic boundary condition are applied to the boundaries orthogonal to $\hat{x}$, while the PC conditions are enforced on the remaining boundaries. As explained in Sect. 3.7, SPP are localized at the surface of the metal and the field amplitude decays exponentially in the y and z directions. Therefore, we expect that the PC conditions will only marginally affect the SPP guided modes that propagate along the sphere chain, that are the modes we are interested in. The 3D mesh used in this simulation is adapted to the problem, being denser in the sphere and around it, to achieve a better precision in the description of the surface mode, while being coarser near the edges of the unit cell, to keep low the number of degrees of freedom. The mesh presented has a total number of 7528 nodes

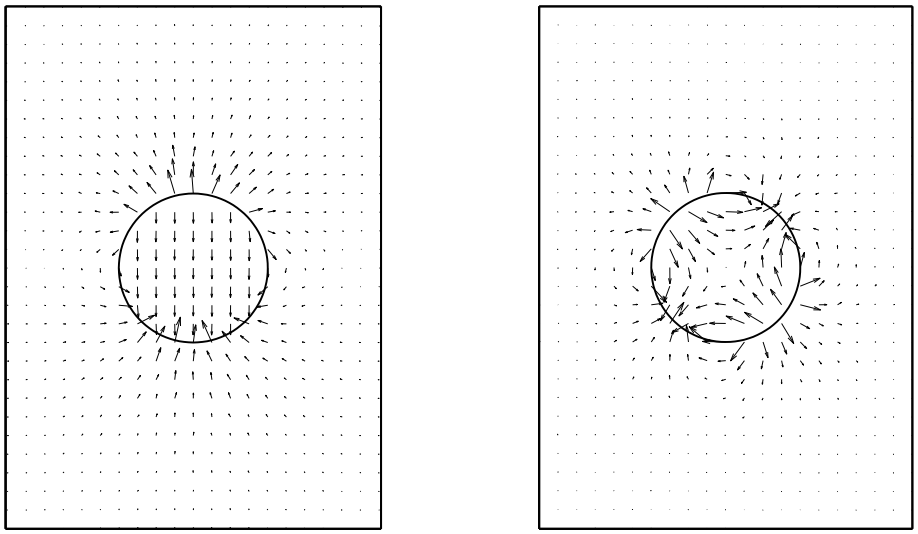

Figure 6.10: Vector plot for the electric field $\boldsymbol{E}$ along the slice $z = 0$, for a dipolar transverse excitation (left) and a quadrupolar excitation (right), corresponding respectively to the frequencies (a) and (c) in Figure 6.9.

and 49952 edges, reduced to 47769 after applying the boundary conditions.

Figure 6.9 shows the band diagram for the guided modes, below the light cone. The lowest frequency bands correspond to propagation along the chain by means of coupled dipolar excitation. The two almost degenerate modes, indicated by (a), correspond to transversal excitation, while the mode marked by (b) is longitudinal propagation. The bands at higher frequencies correspond to higher multipolar excitations. Fig. 6.10 is the vector plot of the electric field for the dipolar excitation. These results can be successfully confronted with an analytic analysis of the propagation via dipolar excitation, published in [66]. We emphasize that our results are obtained modeling the sphere as a metallic object with finite diameter, and not just as an electric dipole.

6.4 Discussion

6.4.1 Flat Bands and Surface Modes

According to the theory of SPP [49, 50], as said in Sect. 3.7, as the mode order increase the resonance frequency should converge to the plasmon resonance frequency $\omega_p/\sqrt{1+\epsilon_b}$ ($\omega_p/\sqrt{2}$ for metal in air). However, in both the FDM and FEM simulations, the higher order modes populate the frequency region over $\omega_p/\sqrt{2}$, up to the plasma frequency. A similar phenomenon is also observed with other numerical methods, such as FDTD [65, 67].

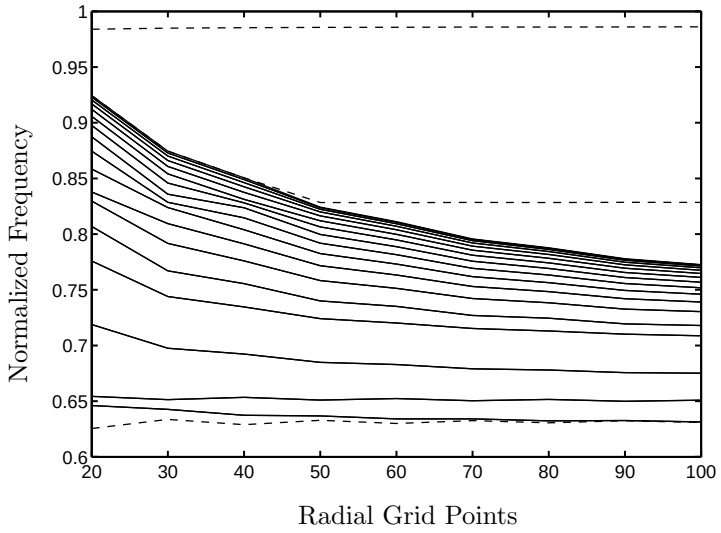

Figure 6.11: FDM convergence results for modes supported by a metallic rod in air, with $r/R = 0.3$ and $\omega_p^N = 1$, where r is the rod radius and R is the radius of the computation domain. The angular discretization is fixed at 32 points, while the radial resolution is increased. The dashed lines correspond to air-confined modes.

Our explanation is the following: The maximum mode order (related to the number of lobes) is fixed by the discretization length (the method cannot simulate SP with lobes smaller than the grid size. As the mode order increase, the electromagnetic field is more and more concentrated in a small region on the metal-dielectric interface, and therefore are more affected by the spatial discretization. Increasing the resolution, the eigenfrequencies should converge to the theoretical value, but at the same time new modes with even higher order are computed as a consequence of the decreased discretization length, and will suffer of numerical errors as well. As a consequence, it is not generally possible to avoid high order modes in the frequency region above the plasmon resonance frequency; however, it can be done for particular geometries. To verify our explanation, we computed the resonance frequencies for a cylindrical rod (a 2D problem) in Polar coordinates. The simulation domain is circular, with PEC conditions imposed on the boundary. Since we will investigate the eigenfrequencies of the higher order modes, we expect the electromagnetic field to be vanishing far from the metal-air interface, and therefore to be negligibly affected by the PEC. In this case, the maximum number of lobes (and therefore the maximum mode order) is fixed by the angular discretization, while the radial resolution can be increased arbitrarily without adding new surface modes to the band diagram. Fig. 6.11 shows the convergence of the eigenvalues at the theoretical value of $\omega_p/\sqrt{2} \simeq 0.71$ with increasing radial resolution. We point out that the convergence rate is not optimal because only one of the two grid discretization lengths is actually reduced, but the graph shows indeed how the error on the eigenfrequencies is dependent from the spatial discretization.

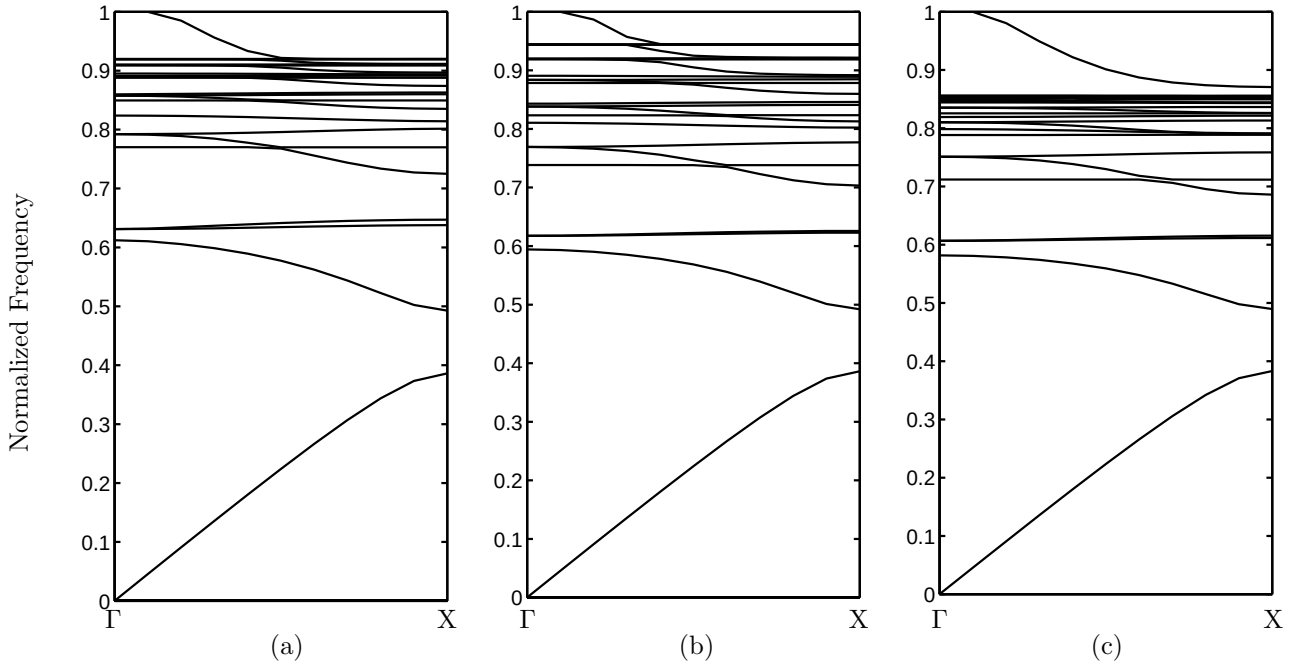

Figure 6.12: Partial band diagram for a 2D square lattice of metallic square rods, computed with FDM (a), FEM with rectangular elements (b), FEM with triangular elements on a square grid (c).

6.4.2 Comparison between FDM and FEM

As explained in the previous sections, the advantage of a FEM formulation over FDM is the absence of fictitious modes in the band diagram. Another advantage is the use of a triangular grid instead of a rectangular one, that gives better convergence results with the same number of degrees of freedom [52]. We noted that in all the FDM simulations, the high order modes (discussed in Sect. 6.4.1) populate the frequency range approximatively from $\omega_p/\sqrt{2}$ to $0.91\omega_p$ (for metal in air), while using FEM the flat bands appear only up to approximately $0.85\omega_p$ (see, e.g., Fig. 6.6). To investigate this behavior, we implemented a FEM with rectangular edge elements, in order to determine if the numerical error on the higher order modes is due to the formulation (FEM or FDM) or to the mesh geometry (triangular or rectangular). Fig. 6.12 present the band diagrams from Γ to X computed using FDM (a), with grid resolution on 20×20; FEM with rectangular elements (b), with the same grid resolution of 20×20; and FEM with triangular elements (c), with a mesh obtained from the grid used in (a) and (b) by dividing each rectangle in two triangles. It appears that the FEM formulation is more accurate with the same number of degrees of freedom (for example, in the degeneracy of the band in the range 0.6-0.7), and that the numerical error suffered by the higher order modes is ultimately due to the element geometry, being less serious for triangular meshes.

Chapter 7

Conclusions

In this work we presented two numerical implementations of the recently proposed Auxiliary Fields formulation for computing the electromagnetic eigenfrequencies of dispersive periodic structures, focusing in particular on metamaterials with metallic components. The first implementation is realized with a Finite-Difference Method (FDM). The FDM is successful in the computation of the low-frequency modes, but suffers from a critical issue that seriously hinders the possibility of a general use: the method tends to create strongly localized "fictitious" modes on the metal-dielectric interfaces. Inherent from the staircase approximation of the geometry, these modes can mix with the physical modes, and therefore pollute the obtained band diagram. Thus we concluded that the FDM approach, although widely used in computational electromagnetics, in this case is not effective for numerical solutions of the problem.

In the second implementation, we used a Finite Elements Method (FEM) in order to solve the issues associated with the FDM approach. We chose an Edge Element basis for the finite element space to avoid the introduction of fictitious modes, and successfully reproduced some two-dimensional results obtained with other numerical methods (in particular, Time Domain methods). We then extended the algorithm to 3D problems and showed the applicability of the formulation by computing the dispersion relation and the electric field distribution for a plasmonic waveguide consisting of a chain of spheres, that, until now, has only been investigated analytically under the approximation of dipolar excitation.

In both the FDM and FEM approaches, the Auxiliary Fields formulation proved to be able to compute a great number of modes that is limited only by the spatial discretization. Hence the formulation has the potential to compute all the existing eigenfrequencies for a structure, given a fixed discretization. We notice that highest order surface modes suffer from consistent numerical errors. This error is due mainly to the spatial discretization

and cannot be solved completely by an increment of the resolution. The above argument has been proved with a convergence study under particular conditions. We also determined that the extent of the numerical error is dependent on the mesh geometry, being smaller with triangular elements.

In conclusion, we have implemented the Auxiliary Field method for computing the photonic bands of dispersive periodic structures with both a Finite-Element Method and a Finite-Difference Method. In particular, we identified that the edge-element based FEM can be an efficient numerical tool for the design and investigation of metamaterials with any complex geometry.

Chapter 8

Bibliography

[1] J. B. Pendry, A. J. Holden, D. J. Robbins, and W. J. Stewart. Magnetism from conductors and enhanced nonlinear phenomena. *Microwave Theory and Techniques, IEEE Transactions on* **47**, 11 (2075–2084), 2002.

[2] D. Schurig, J. J. Mock, B. J. Justice, S. A. Cummer, J. B. Pendry, A. F. Starr, and D. R. Smith. Metamaterial Electromagnetic Cloak at Microwave Frequencies. *Science* **314**, 5801 (977–980), 2006.

[3] J. Valentine, J. Li, T. Zentgraf, G. Bartal, and X. Zhang. An optical cloak made of dielectrics. *Nature Materials* **8**, 7 (568–571), 2009.

[4] N. I. Landy, S. Sajuyigbe, J. J. Mock, D. R. Smith, and W. J. Padilla. Perfect metamaterial absorber. *Phys. Rev. Lett.* **100**, 20 (207402), 2008.

[5] J. D. Joannopoulos, S. G. Johnson, J. N. Winn, and R. D. Meade. *Photonic Crystals: Molding the Flow of Light*. Princeton University Press, second edition, 2008.

[6] J. W. Strutt, Lord Rayleigh. On the remarkable phenomenon of crystalline reflexion described by Prof. Stokes. *Phil. Mag.* **26** (256–265), 1888.

[7] E. Yablonovitch. Inhibited spontaneous emission in solid-state physics and electronics. *Phys. Rev. Lett.* **58**, 20 (2059–2062), 1987.

[8] S. John. Strong localization of photons in certain disordered dielectric superlattices. *Phys. Rev. Lett.* **58**, 23 (2486–2489), 1987.

[9] S. Noda, A. Chutinan, and M. Imada. Trapping and emission of photons by a single defect in a photonic bandgap structure. *Nature* **407**, 6804 (608–610), 2000.

[10] S. G. Johnson, S. Fan, P. R. Villeneuve, J. D. Joannopoulos, and L. A. Kolodziejski. Guided modes in photonic crystal slabs. *Phys. Rev. B* **60**, 8 (5751–5758), 1999.

[11] Y. Akahane, T. Asano, B. S. Song, and S. Noda. High-q photonic nanocavity in a two-dimensional photonic crystal. *Nature* **425**, 6961 (944–947), 2003.

[12] T. Tanabe, M. Notomi, S. Mitsugi, A. Shinya, and E. Kuramochi. All-optical switches on a silicon chip realized using photonic crystal nanocavities. *Applied Physics Letters* **87**, 15 (151112), 2005.

[13] H. Altug, D. Englund, and J. Vuckovic. Ultrafast photonic crystal nanocavity laser. *Nat. Phys.* **2** (484–488), 2006.

[14] B. S. Song, S. Noda, and T. Asano. Photonic devices based on in-plane hetero photonic crystals. *Science* **300**, 5625 (1537), 2003.

[15] S. G. Johnson, P. R. Villeneuve, S. Fan, and J. D. Joannopoulos. Linear waveguides in photonic-crystal slabs. *Phys. Rev. B* **62**, 12 (8212–8222), 2000.

[16] A. Mekis, J. C. Chen, I. Kurland, S. Fan, P. R. Villeneuve, and J. D. Joannopoulos. High transmission through sharp bends in photonic crystal waveguides. *Phys. Rev. Lett.* **77**, 18 (3787–3790), 1996.

[17] H. Gersen, T. J. Karle, R. J. P. Engelen, W. Bogaerts, J. P. Korterik, N. F. van Hulst, T. F. Krauss, and L. Kuipers. Real-space observation of ultraslow light in photonic crystal waveguides. *Phys. Rev. Lett.* **94**, 7 (073903), 2005.

[18] S. Fan, P. Villeneuve, J. Joannopoulos, and H. Haus. Channel drop filters in photonic crystals. *Opt. Express* **3**, 1 (4–11), 1998.

[19] Z. Zhang and M. Qiu. Compact in-plane channel drop filter design using a single cavity with two degenerate modes in 2d photonic crystal slabs. *Opt. Express* **13**, 7 (2596–2604), 2005.

[20] P. Russell. Photonic Crystal Fibers. *Science* **299**, 5605 (358–362), 2003.

[21] J. C. Knight. Photonic crystal fibres. *Nature* **424** (847–851), 2003.

[22] J. C. Knight, J. Broeng, T. A. Birks, and P. S. J. Russell. Photonic Band Gap Guidance in Optical Fibers. *Science* **282**, 5393 (1476–1478), 1998.

[23] P. Roberts, F. Couny, H. Sabert, B. Mangan, D. Williams, L. Farr, M. Mason, A. Tomlinson, T. Birks, J. Knight, and P. S. J. Russell. Ultimate low loss of hollow-core photonic crystal fibres. *Opt. Express* **13**, 1 (236–244), 2005.

[24] F. Benabid, F. Couny, J. C. Knight, T. A. Birks, and P. S. J. Russell. Compact, stable and efficient all-fibre gas cells using hollow-core photonic crystal fibres. *Nature* **434** (488–491), 2005.

[25] J. C. Knight, T. A. Birks, P. S. J. Russell, and J. P. de Sandro. Properties of photonic crystal fiber and the effective index model. *J. Opt. Soc. Am. A* **15**, 3 (748–752), 1998.

[26] T. A. Birks, J. C. Knight, and P. S. Russell. Endlessly single-mode photonic crystal fiber. *Opt. Lett.* **22**, 13 (961–963), 1997.

[27] J. K. Ranka, R. S. Windeler, and A. J. Stentz. Visible continuum generation in air-silica microstructure optical fibers with anomalous dispersion at 800 nm. *Opt. Lett.* **25**, 1 (25–27), 2000.

[28] W. Wadsworth, J. Knight, W. Reeves, P. Russell, and J. Arriaga. Yb^{3+}-doped photonic crystal fibre laser. *Electronics Letters* **36**, 17 (1452–1454), 2000.

[29] J. Limpert, T. Schreiber, S. Nolte, H. Zellmer, T. Tunnermann, R. Iliew, F. Lederer, J. Broeng, G. Vienne, A. Petersson, and C. Jakobsen. High-power air-clad large-mode-area photonic crystal fiber laser. *Opt. Express* **11**, 7 (818–823), 2003.

[30] A. Ortigosa-Blanch, J. C. Knight, W. J. Wadsworth, J. Arriaga, B. J. Mangan, T. A. Birks, and P. S. J. Russell. Highly birefringent photonic crystal fibers. *Opt. Lett.* **25**, 18 (1325–1327), 2000.

[31] P. Roberts, B. Mangan, H. Sabert, F. Couny, T. Birks, J. Knight, and P. Russell. Control of dispersion in photonic crystal fibers. *Journal of Optical and Fiber Communications Research* **2** (435–461), 2005.

[32] E. Cubukcu, K. Aydin, E. Ozbay, S. Foteinopoulou, and C. M. Soukoulis. Electromagnetic waves: Negative refraction by photonic crystals. *Nature* **423** (604–605), 2003.

[33] C. Luo, S. G. Johnson, J. D. Joannopoulos, and J. B. Pendry. All-angle negative refraction without negative effective index. *Phys. Rev. B* **65**, 20 (201104), 2002.

[34] M. Notomi. Theory of light propagation in strongly modulated photonic crystals: Refractionlike behavior in the vicinity of the photonic band gap. *Phys. Rev. B* **62**, 16 (10696–10705), 2000.

[35] P. V. Parimi, W. T. Lu, P. Vodo, and S. Sridhar. Photonic crystals: imaging by flat lens using negative refraction. *Nature* **426**, 6965 (404), 2003.

[36] V. G. Veselago. The electrodynamics of substances with simultaneously negative values of ϵ and μ. *Soviet Physics Uspekhi* **10**, 4 (509–514), 1968.

[37] D. R. Smith and N. Kroll. Negative refractive index in left-handed materials. *Phys. Rev. Lett.* **85**, 14 (2933–2936), 2000.

[38] D. R. Smith, W. J. Padilla, D. C. Vier, S. C. Nemat-Nasser, and S. Schultz. Composite medium with simultaneously negative permeability and permittivity. *Phys. Rev. Lett.* **84**, 18 (4184–4187), 2000.

[39] G. Shvets. Photonic approach to making a material with a negative index of refraction. *Phys. Rev. B* **67**, 3 (035109), 2003.

[40] S. Zhang, W. Fan, N. C. Panoiu, K. J. Malloy, R. M. Osgood, and S. R. J. Brueck. Experimental demonstration of near-infrared negative-index metamaterials. *Phys. Rev. Lett.* **95**, 13 (137404), 2005.

[41] J. Valentine, S. Zhang, T. Zentgraf, E. Ulin-Avila, D. A. Genov, G. Bartal, and X. Zhang. Three-dimensional optical metamaterial with a negative refractive index. *Nature* **455**, 7211 (376–379), 2008.

[42] J. B. Pendry, A. J. Holden, W. J. Stewart, and I. Youngs. Extremely low frequency plasmons in metallic mesostructures. *Phys. Rev. Lett.* **76**, 25 (4773–4776), 1996.

[43] J. D. Jackson. *Classical Electrodynamics*, volume 2010. 1998.

[44] N. W. Ashcroft and D. N. Mermin. *Solid State Physics*. Thomson Learning, Toronto, 1 edition, 1976.

[45] A. Raman and S. Fan. Photonic band structure of dispersive metamaterials formulated as a hermitian eigenvalue problem. *Phys. Rev. Lett.* **104**, 8 (087401), 2010.

[46] C. Kittel. *Introduction to Solid State Physics*, volume 2010. 1995.

[47] D. Bohm and D. Pines. A collective description of electron interactions: Iii. coulomb interactions in a degenerate electron gas. *Phys. Rev.* **92**, 3 (609–625), 1953.

[48] E. A. Stern and R. A. Ferrell. Surface plasma oscillations of a degenerate electron gas. *Phys. Rev.* **120**, 1 (130–136), 1960.

[49] J. M. Pitarke, V. M. Silkin, E. V. Chulkov, and P. M. Echenique. Theory of surface plasmons and surface-plasmon polaritons. *Reports on Progress in Physics* **70**, 1 (1), 2007.

[50] T. Ito and K. Sakoda. Photonic bands of metallic systems. ii. features of surface plasmon polaritons. *Phys. Rev. B* **64**, 4 (045117), 2001.

[51] K. Yee. Numerical solution of inital boundary value problems involving maxwell's equations in isotropic media. *IEEE Transactions on Antennas and Propagation* **14** (302–307), 1966.

[52] J. Jin. *The Finite Element Method in Electromagnetics*. Wiley, second edition, 2002.

[53] N. Venkatarayalu and J.-F. Lee. *IEEE Transactions on Microwave Theory and Techniques* **54**, 2006.

[54] ARPACK - Arnoldi Package. `http://www.caam.rice.edu/software/ARPACK/`.

[55] R. Lehoucq and D. Sorensen. Deflation techniques for an implicitly re-started arnoldi iteration. *SIAM J. Matrix Analysis and Applications* **17** (789–821), 1996.

[56] R. Lehoucq, D. Sorensen, and C. Yang. *ARPACK Users' Guide: Solution of Large-Scale Eigenvalue Problems with Implicitly Restarted Arnoldi Methods*. Philadelphia, 1998.

[57] D. Sorensen. Implicit application of polynomial filters in a k-step arnoldi method. *SIAM J. Matrix Analysis and Applications* **13** (357–385), 1992.

[58] PARDISO - Parallel Sparse Direct Solver. `http://www.pardiso-project.org/`.

[59] O. Schenk and K. Gärtner. Solving unsymmetric sparse systems of linear equations with PARDISO. *Journal of Future Generation Computer Systems* **20** (475–487), 2004.

[60] LOBPCG - Locally Optimized Block Preconditioned Conjugate Gradient. `http://math.ucdenver.edu/~aknyazev/software/CG/`.

[61] A. V. Knyazev. Toward the optimal preconditioned eigensolver: Locally optimal block preconditioned conjugate gradient method. *SIAM J. Sci. Comput* **23** (517–541), 2000.

[62] T. Huckle. Factorized sparse approximate inverses for preconditioning. *The Journal of Supercomputing* **25** (109–117), 2003. 10.1023/A:1023988426844.

[63] MPB - MIT Photonic Bands. `http://ab-initio.mit.edu/wiki/index.php/MIT_Photonic_Bands/`.

[64] S. Johnson and J. Joannopoulos. Block-iterative frequency-domain methods for maxwell's equations in a planewave basis. *Opt. Express* **8**, 3 (173–190), 2001.

[65] G. Veronis, R. W. Dutton, and S. Fan. Metallic photonic crystals with strong broadband absorption at optical frequencies over wide angular range. *Journal of Applied Physics* **97**, 9 (093104), 2005.

[66] W. H. Weber and G. W. Ford. Propagation of optical excitations by dipolar interactions in metal nanoparticle chains. *Phys. Rev. B* **70**, 12 (125429), 2004.

[67] V. Kuzmiak, A. A. Maradudin, and F. Pincemin. Photonic band structures of two-dimensional systems containing metallic components. *Phys. Rev. B* **50**, 23 (16835–16844), 1994.

Appendix A

Plasmonic Bands of Metallic Photonic Crystals: a Re-examination with Auxiliary-Fields Formulation (Paper submitted to Physics Review B, August 24, 2010)

Plasmonic Bands of Metallic Photonic Crystals: a Re-examination with Auxiliary-Fields Formulation

Andrea Ferrario[1,2],* Min Yan[1],† and Min Qiu[1]
[1] *Laboratory of Photonics and Microwave Engineering, School of Information and Communication Technology Royal Institute of Technology (KTH), Electrum 229, 16440 Kista, Sweden*
[2] *Department of Physics, Politecnico di Milano p.zza Leonardo da Vinci 32, 20133 Milan, Italy*
(Dated: August 24, 2010)

The optical properties of periodic metamaterials with metallic inclusions are characterized by the photonic bands that are essentially surface plasmon polaritons in nature. An accurate derivation of these plasmonic bands is vital for designing as well as for understanding this class of materials. We start from the recently proposed Hermitian eigen-formulation for lossless dispersive media [Phys. Rev. Lett. 104, 087401 (2010)] in a finite-difference scheme to address the importance of an accurate numerical representation of metal-dielectric interfaces. An inadequate meshing can lead to highly localized fictitious modes at the interface, contaminating the physical plasmonic bands. The convergence of plasmonic bands and the emergence of new surface-mode bands with the increase of grid resolution for a rod-in-air system is then discussed with a formulation in cylindrical polar coordinates. Finally we demonstrate band structures derived with a more versatile implementation based on the finite-element method, which is able to eliminate the fictitious surface modes for metamaterials with any curved interfaces.

PACS numbers: 78.67.Pt, 78.20.Bh, 42.70.Qs

I. INTRODUCTION

The optical properties of periodic metamaterials, including photonic crystals (PCs), are strictly related to their photonic band structures. The spatial periodicity significantly affects the dispersion relation of the electromagnetic waves and causes peculiar phenomena, such as the presence of photonic band gaps. The problem of determining the photonic bands of a periodic metamaterial has been intensively investigated in the past two decades and a number of methods have been developed to deal with these structures. For a PC containing materials whose dielectric permittivities can be regarded as constants with respect to the frequency, Maxwell's Equations can be rewritten as an Hermitian eigenvalue problem [1], that can be solved numerically with standard eigenvalue algorithms.

Recently, metamaterials containing metallic components have attracted a great amount of interest, primarily for producing media with an effective permittivity or permeability at any desired value. Ever since the first experimental demonstration of such engineered material at the microwave frequency [2], research teams have kept reducing the unit size of metamaterials. Some of the fabricated samples are already functioning at the optical frequency [3]. In most cases, optical metamaterials involving noble metals are operating at a frequency slightly below the metals' plasmon resonance frequency. In this frequency range, photons can be strongly coupled through metal-dielectric interfaces to the electrons in the metal elements in the form of surface plasmon polaritons (SPPs) [4]. We refer to the dispersion curves of such modes across the Brillouin zone as *plasmonic bands*. From the characteristics of these plasmonic bands one can potentially determine the effective optical properties of various periodic systems, such as the negative refraction phenomenon in the fish-net metamaterial [3], the phase and group velocity information of the plasmonic waveguide based on nano-scaled metallic spheres [5], and even the absorption properties of a plasmonic absorber [6], etc. Obtaining the band structure of a metamaterial provides a much more complete solution than various simplified approaches, such as the retrieval of effective material parameters based on the scattering matrix [2] or the Maxwell-Garnett approximations, in telling its electromagnetic properties.

For metamaterials whose metallic inclusions have a cylindrical or spherical symmetry, the multipole expansion method can be used to efficiently obtain the band structures. The approach works particularly well with structures formed by small interacting metallic particles, such as a chain of metallic spheres [5, 7]. For metamaterials with more complex metallic inclusions, full-numerical approaches are usually advantageous. The finite-difference time-domain method (FDTD) [8] is formulated directly from the Maxwell's equations by using a constitutive relation $\boldsymbol{J} = \sigma \boldsymbol{E}$. The FDTD approach however heavily relies on the simulation setup and post signal processing; therefore it can hardly generate the complete band structure in a consistent manner. We ob-

*Electronic address: ferrario@kth.se
†Electronic address: miya@kth.se

serve that there has been a lack of detailed discussion on the behaviors of the plasmonic bands, partly owing to the difficulty in obtaining the complete band structure of a periodic dispersive media.

In this paper, we will use a frequency-domain approach based on the introduction of auxiliary mechanical fields [9] to model the metal response to an electromagnetic field. An eigenvalue problem is formulated from a set of differential equations which consists of the Maxwell's equations coupled with the equation of motion governing the mechanical fields. Two numerical schemes, a finite-difference formulation on a rectangular grid and a finite-element formulation based on edge elements, are implemented separately. The band structures resulting from the two algorithms are analyzed and discussed. The simulation results obtained are compared closely against the previous results in the literature over common model structures. Our results confirm some of the previous findings and more importantly resolve some ambiguities found in the literature. We emphasize that in order to accurately capture the plasmonic bands, one has to use an appropriate numerical mesh and pay particular attention to the metal-dielectric interface representation.

II. THEORY

In this section we will formulate the dispersion relation of a lossless periodic metallic structure as an eigenvalue problem. The approach is a variant of the one followed in [9], but in our case with only two vector fields (electric, $\boldsymbol{E}$, and polarization, $\boldsymbol{P}$). The dielectric permittivity of a metal can be described either by the Drude model

$$\epsilon_r(\omega) = 1 - \frac{\omega_p^2}{\omega(\omega - i\gamma)} \tag{1}$$

where ω_p is the plasma frequency of the material and γ is the electron collision frequency, or by the Lorentz model

$$\epsilon_r(\omega) = 1 + \frac{\omega_p^2}{\omega_0^2 - \omega^2 + i\gamma\omega} \tag{2}$$

where ω_0 is the resonance frequency, or by a combination of the two (Lorentz-Drude model). These models are well suited to describe many electromagnetic properties of commonly used metals, such as silver or gold. The Drude and Lorentz models arise from two mechanical pictures of the electron motion inside metals: respectively, free electrons with constant elastic collisions with ion cores and oscillating electrons around cores with damping. A new eigenvalue problem can thus be formulated by adding to the Maxwell's equations the equation of motion for the electrons. To achieve this, one can introduce a mechanical field $\boldsymbol{x}$, or the mean electron displacement, which is proportional to the material polarization field through the relation $\boldsymbol{P} = en\boldsymbol{x}$ with e the electron charge and n the electron density. The equation of motion can consequently be coupled to the Maxwell's equations. For a nonmagnetic medium ($\boldsymbol{M} = 0$), in case of no free charges or currents, the resulting set of equations, in SI units, is

$$\begin{aligned} \nabla \times \boldsymbol{E} &= -\mu_0 \dot{\boldsymbol{H}}, \\ \nabla \times \boldsymbol{H} &= \epsilon_0 \dot{\boldsymbol{E}} + \dot{\boldsymbol{P}}, \\ \omega_p^2 \epsilon_0 \boldsymbol{E} - \omega_0^2 \boldsymbol{P} - \gamma \dot{\boldsymbol{P}} &= \ddot{\boldsymbol{P}}, \end{aligned} \tag{3}$$

where the dots represent time derivatives. The plasma frequency is obtained from the material parameters as $\omega_p^2 = \frac{e^2 n}{\epsilon_0 m}$. These equations must be restricted by the divergence-free condition

$$\begin{aligned} \nabla \cdot (\epsilon_0 \boldsymbol{E} + \boldsymbol{P}) &= 0, \\ \nabla \cdot \boldsymbol{H} &= 0. \end{aligned} \tag{4}$$

Considering the steady state with time dependence $exp(i\omega t)$, we obtain

$$\begin{aligned} \nabla \times \boldsymbol{E} &= i\omega\mu_0 \boldsymbol{H}, \\ \nabla \times \boldsymbol{H} &= -i\omega\epsilon_0 \boldsymbol{E} - i\omega \boldsymbol{P}, \\ \omega_p^2 \epsilon_0 \boldsymbol{E} - \omega_0^2 \boldsymbol{P} + i\omega\gamma \boldsymbol{P} &= -\omega^2 \boldsymbol{P}. \end{aligned} \tag{5}$$

These equations can be reformulated as a linear eigenvalue problem in the lossless case ($\gamma = 0$).

$$\omega^2 \begin{bmatrix} \boldsymbol{E} \\ \boldsymbol{P} \end{bmatrix} = \begin{bmatrix} \frac{1}{\epsilon_0}\nabla \times \frac{1}{\mu_0}\nabla \times \bullet + \omega_p^2 \bullet & -\frac{\omega_0^2}{\epsilon_0}\bullet \\ -\omega_p^2 \epsilon_0 \bullet & \omega_0^2 \bullet \end{bmatrix} \begin{bmatrix} \boldsymbol{E} \\ \boldsymbol{P} \end{bmatrix}. \tag{6}$$

The eigenvalues ω are the oscillation frequencies at which solutions of the system of equations exist. A linear eigenvalue problem can be formulated also in the lossy case by introducing additional vector fields in the system of equations, as in [9]. By applying a scale factor to the fields in Eq. 6, one obtains a Hermitian eigenvalue problem,

$$\omega^2 \boldsymbol{F} = \begin{bmatrix} \frac{1}{\sqrt{\epsilon_0}}\nabla \times \frac{1}{\mu_0}\nabla \times \left(\frac{1}{\sqrt{\epsilon_0}}\bullet\right) + \omega_p^2 \bullet & -\omega_p\omega_0 \bullet \\ -\omega_p\omega_0 \bullet & \omega_0^2 \bullet \end{bmatrix} \boldsymbol{F}, \tag{7}$$

where

$$\boldsymbol{F} = \begin{bmatrix} \sqrt{\epsilon_0}\boldsymbol{E} \\ \frac{\omega_0}{\omega_p\sqrt{\epsilon_0}}\boldsymbol{P} \end{bmatrix}. \tag{8}$$

If one opts for the Drude model, Eq. (6) can be further simplified by setting $\omega_0 \to 0$, as

$$\omega^2 \boldsymbol{E} = \frac{1}{\epsilon_0}\nabla \times \frac{1}{\mu_0}\nabla \times \boldsymbol{E} + \omega_p^2 \boldsymbol{E}. \tag{9}$$

An eigenvalue problem for materials with a Drude-Lorentz model can be formulated by adding more mechanical fields.

III. FINITE-DIFFERENCE APPROACH

Equation (6) can be used for the computation of the electromagnetic properties of structures containing

metallic components after a suitable discretization is applied. In the following, we will present our implementations and simulation results in 2D scenarios. An extension to 3D problems is straightforward. Since we are interested especially in SPP modes (or plasmonic bands as in periodic systems), the transverse-magnetic (TM) polarization is chosen in all case studies. We first use a finite-difference approach to convert the differential operator in Eq. (6) to a matrix, whose eigenvalues correspond to the frequencies of the allowed electromagnetic modes. The electric and polarization fields are discretized using a rectangular grid. More specifically, the discretized $\boldsymbol{E}$ and $\boldsymbol{P}$ field components are evaluated at the same points in space, along the edges of the rectangular grids in 2D. The curl of the electric field is evaluated at the centers of the grids. We refer to this scheme of implementation as the finite-different method (FDM).

The Hermitian formulation of the problem presented in Section II is convenient for the computation of the eigenfrequencies of a general dispersive system. A suitable eigen-solver method such as the conjugate gradient minimization of the Rayleigh quotient can be employed [10] to locate these eigenfrequencies and their corresponding field patterns. The divergence-free condition can be enforced by maintaining the orthogonality of the solutions with respect to the divergence matrix (obtained by discretizing Eq. (4)) during the deflation. With this approach, we have extensively studied metamaterial systems whose metallic elements are characterized by the Drude model (eq. (9)), in which $\omega_p \neq 0$. While previously virtually the same approach was demonstrated viable for calculating the band structure of a dispersive system [9], its validity and conformation to former studies have not been rigorously discussed. It is the objective of this paper to point out that this approach, when misused, can give rise to wrong plasmonic modes. More explicitly, when the finite-difference mesh is not adequately applied, especially in representing metal-dielectric interfaces, fictitious modes localized at the interfaces would appear. In passing, we will also show how surface modes converge as well as how new modes emerge as the numerical mesh resolution increases. Such convergence tests are absent in previous studies. We elaborate these issues separately in detail in the following subsections.

A. Fictitious Surface Modes

Since the unknowns are defined along the edges of the rectangular grids in a finite-difference implementation, ambiguities arise when a metal-dielectric interface passes through a grid unit. Under such a circumstance, one has to decide how many edges of the grid should the $\boldsymbol{P}$ variable be assigned onto. When this issue is not taken care of properly, the unit grid through which the metal-dielectric interface passes will act as a fictitious material layer which neither belongs to the metal nor belongs to the dielectric. Moreover, the fictitious layer supports highly localized modes at frequencies below ω_p, heavily affecting the plasmonic band structure. For rectangular metallic inclusions, this problem can be resolved by choosing a precise grid size such that the interfaces sit exactly on the grid edges, as normally done when one deals with simulation of perfect metals in a FDTD approach [11]. However the problem almost always persists when one deals with metallic inclusions with curved shapes with this method. This issue hinders the accuracy of the finite-difference implementation, and calls for a more general numerical implementation.

The above-mentioned problem is illustrated in Fig. 1 by using a periodic structure with square metallic inclusions. The metal has a normalized plasma frequency $\omega_p^N = \frac{\omega_p a}{2\pi c} = 1$, where a is the period of the metamaterial, and the background medium is air. The square metal inclusions have a side length of $0.3a$. Two possible finite-difference mesh choices are applied to calculate the band structure of the metamaterial along the Γ-X direction. In the first case, the mesh illustrated by Fig. 1(a) is used: for grids containing the metal-dielectric interface, $\boldsymbol{P}$ fields are defined on three edges of the grids. The corresponding band structure obtained is shown in Fig. 1(c). The numerical resolution used is 20×20. The band structure exhibits many flat bands across the frequency range mainly from 0.39 to 0.72. The exact number of flat bands increase with the resolution used. A close inspection of the spatial mode distribution reveals that many of these bands correspond to modes confined in a single-grid layer between the metal and the air region. These highly localized modes emerge as a consequence of the fictitious layer due to inadequate metal-dielectric interface representation. The effect of this fictitious layer is comparable to a structurization (e.g. corrugation or hole drilling) of the surface, that lowers the surface plasmon resonance frequency, as Pendry *et al.* showed in [12]. In the second case, we employ the mesh illustrated in Fig. 1(b). The resulted band structure, again with a numerical resolution of 20×20, is given in Fig. 1(d). It is observed that in this case the flat bands are localized in the frequency range between 0.75 and 0.93; a close inspection of the flat-band modes indicate that they indeed correspond to the SPPs confined by the metal-dielectric interface.

Many simulations have been further carried out on determining to which extent the choice of mesh affects the reliability of the method. We finally concluded that the modes due to the fictitious layer problem occur in grid cells in which more than one but less than four edges are chosen as metallic grid points (i.e. with $\boldsymbol{P}$ assigned). These fictitious surface modes can be observed over a wide range of frequencies (even near to the surface plasmon resonance frequency $\omega_p/\sqrt{2}$). More seriously, when the dispersion curve of a fictitious surface mode tends to pass through a band corresponding to a propagating mode, anti-crossing occurs whenever their symmetries agree. Fictitious surface modes can therefore contaminate and distort the *physical* band structure, leading to wrong interpretation of the metamaterial's properties. It

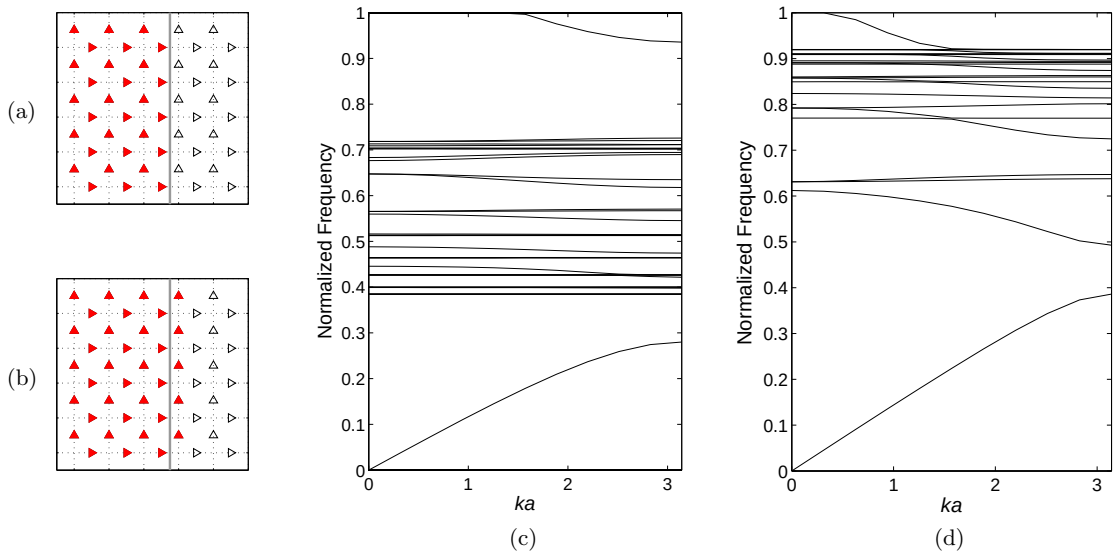

FIG. 1: (a,b) Two finite-difference mesh choices for the discretization of Eq. (9) over a metal-air interface. The right and up arrows represent respectively the discretized x and y components of the $\boldsymbol{E}$ field. The solid red arrows represent the grid points where $\omega_p \neq 0$ (in the metal). (c,d) Band diagrams along the Γ-X direction for a square lattice of square rods, with side $d = 0.3a$ and $\omega_p^N = 1$, obtained with the two mesh choices.

is interesting to point out that similar fictitious surface modes also appear in other numerical formulations, such as the transfer-matrix method used in early photonic band structure calculations [13] when epsilon-averaging is used. The introduction of an averaged layer between the metal and air region creates a number of nonphysical flat bands corresponding to the modes confined in the layer (not shown). In Sect. IV, we will demonstrate that these fictitious surface modes can be eliminated by implementing the formulation on a triangular mesh, i.e. with a finite-element approach. Before that, we shall look into the convergence behavior of flat photonic bands, especially those corresponding to high-order surface-mode resonances.

B. High-Order Surface Modes

It is well-known that for a metal rod with arbitrary cross-section placed in air, there should be infinite number of SPP resonances; in addition, high-order SPP resonances should concentrate at frequencies around $\omega_p/\sqrt{2}$ [14, 15]. With numerical methods, SPP resonances with lobe sizes smaller than a unit grid are not captured; therefore only a limited number of SPP modes would present in the mode spectrum, as shown in Fig. 1(d). Having understood this, one might further raise the question regarding the frequencies of the high-order SPP resonances found in our simulation, which span above $\omega_p/\sqrt{2}$ to ω_p rather than simply being close to $\omega_p/\sqrt{2}$. This phenomenon was also observed with other numerical methods, such as FDTD [16] and the finite-difference method [17]. Our explanation is as follows. With an increasing mode order, the mode field of an SPP resonance becomes more and more concentrated at the metal-dielectric interface and at the same time has a smaller lobe size along the interface. In other words, the numerical mesh can poorly resolute the spatial feature of the mode. Correspondingly the eigen-frequency of the mode tends to suffer from a greater numerical error. By using a mesh with a higher resolution, one expects to see a decrease of the error in eigen-frequency for a fixed surface mode, accompanied by the emergences of new surface modes of even higher orders.

The above argument is best elaborated by computing the resonant modes supported by a single cylindrical rod placed in air in cylindrical polar coordinates. Apart from a different coordinate system, the implementation is otherwise based on the same finite-difference scheme as in the previous subsection. The simulation domain is circular and is terminated with a perfect-electric-conductor (PEC) boundary condition (the usual periodic boundary conditions cannot be imposed in this case because of the inherently circular numerical domain). Due to the fact that the high-order SPP modes are highly evanescent outside the rod, the modes effectively correspond to those belonging the flat-bands in Fig. 1(d). The plasma frequency (normalized against the diameter of the simulation domain $2R$) is set to $\omega_p^N = 1$. By fixing the resolution along the angular coordinate θ (equivalently the maximum surface mode lobe size), one fixes the total number of modes allowed in the system. The effect

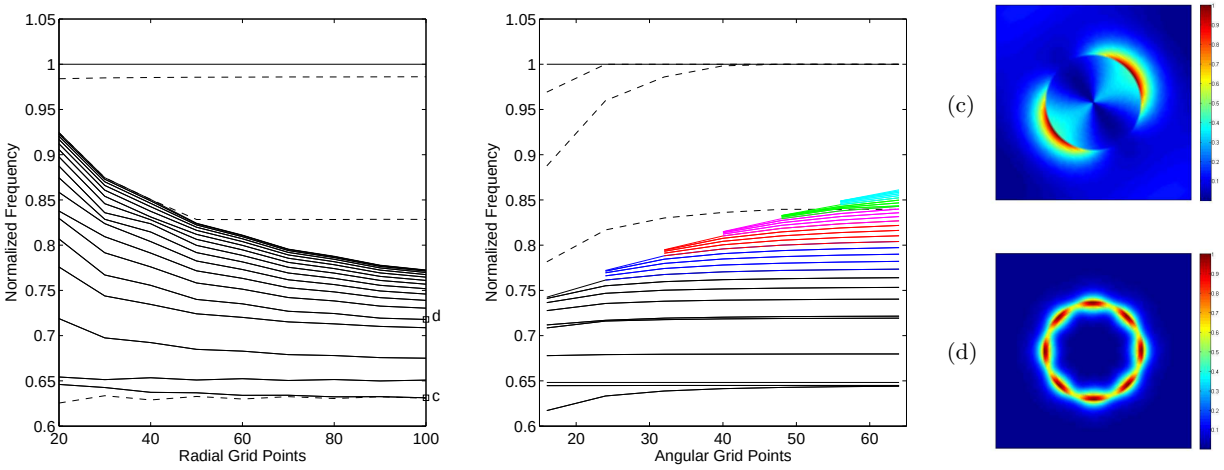

FIG. 2: Convergence results for modes supported by a metallic rod in air, with $r/R = 0.3$ and $\omega_p^N = 1$, where r is the rod radius and R is the radius of the computation domain. (a) Convergence with respect to the radial resolution while the angular discretization is fixed at 32 points. (b) Convergence with respect to the angular resolution while the radial discretization is fixed at 60 points. The dashed lines correspond to air-confined modes. (c,d) Distributions of the normalized $|\boldsymbol{E}|$ for two surface modes as indicated in (a).

of mesh resolution along the radial coordinate is illustrated as in Fig. 2(a). From the figure, one sees that the eigen-frequencies tend to converge, from the upper side, to the expected value of $\omega_p^N/\sqrt{2} \simeq 0.71$ with an increasing radial resolution. The convergence rates are not fast because one has to increase the resolution along the angular direction for achieving better accuracies for these modes. Two representative surface modes are shown in Fig. 2(c) and (d). Particularly Fig. 2(d) shows a tightly confined mode field; therefore the PEC outer-domain termination should have no effect on its frequency.

In Fig. 2(b), we present the eigen-frequency variations as a function of the angular resolution while the radial resolution is fixed. An increase in the angular resolution will allow more higher order modes to appear in the mode spectrum, as indeed demonstrated in Fig. 2(b). With a higher radial resolution, the newly emerged modes appear at frequencies closer to ω_p, due to the fact that the fixed radial resolution becomes relatively poorer to describe these modes; for previously existing modes, an increase in angular resolution does not significantly affect their eigen-frequencies. This indicates that high-order modes suffer from numerical errors mostly due to the poor discretization in the direction orthogonal to the interface.

From the above two studies, the following conclusions can be drawn for numerically deriving the band diagram of a metallic metamaterial: numerical error can't be unlimitedly suppressed by increasing the mesh resolution for all plasmonic bands, especially for those corresponding to high-order SPP resonances; there are always bands missing in the final band diagram for the reason that very-high-order surface-modes are not captured by a mesh of finite resolution.

IV. FINITE-ELEMENTS APPROACH

While the convergence issue discussed in Sect. III B always exists regardless of any numerical implementation, the fictitious-mode issue pointed out in Sect. III A can be mitigated with an improved implementation with an unstructured numerical mesh. In this section, we introduce another implementation for the formulation presented in Sect. II, which is able to completely eliminate the fictitious mode problem. The revised approach is based on a triangular mesh. In this case, an arbitrarily curved metal-dielectric interface can be accurately represented without using a staircase approximation. Particularly, an edge-element based on finite-element method (FEM) is implemented [18]: electric-field unknowns are defined at the midpoints of all triangle edges along their tangential directions; for edges located within or at the boundary of a metal, polarization-field variables are also defined in a similar manner. An implementation based such a triangular mesh can be regarded as a generalization of the one based on a rectangular grid used in Sec. III. The condition for avoiding the fictitious surface modes is thus that each air cell must not be adjacent to more than one metal cells. Effectively the condition ensures either one or all three edges of a triangle cell are assigned with the $\boldsymbol{P}$ variable. Since all field variables are along the edge directions, the continuity condition for the tangential fields across material interfaces is automatically satisfied. In

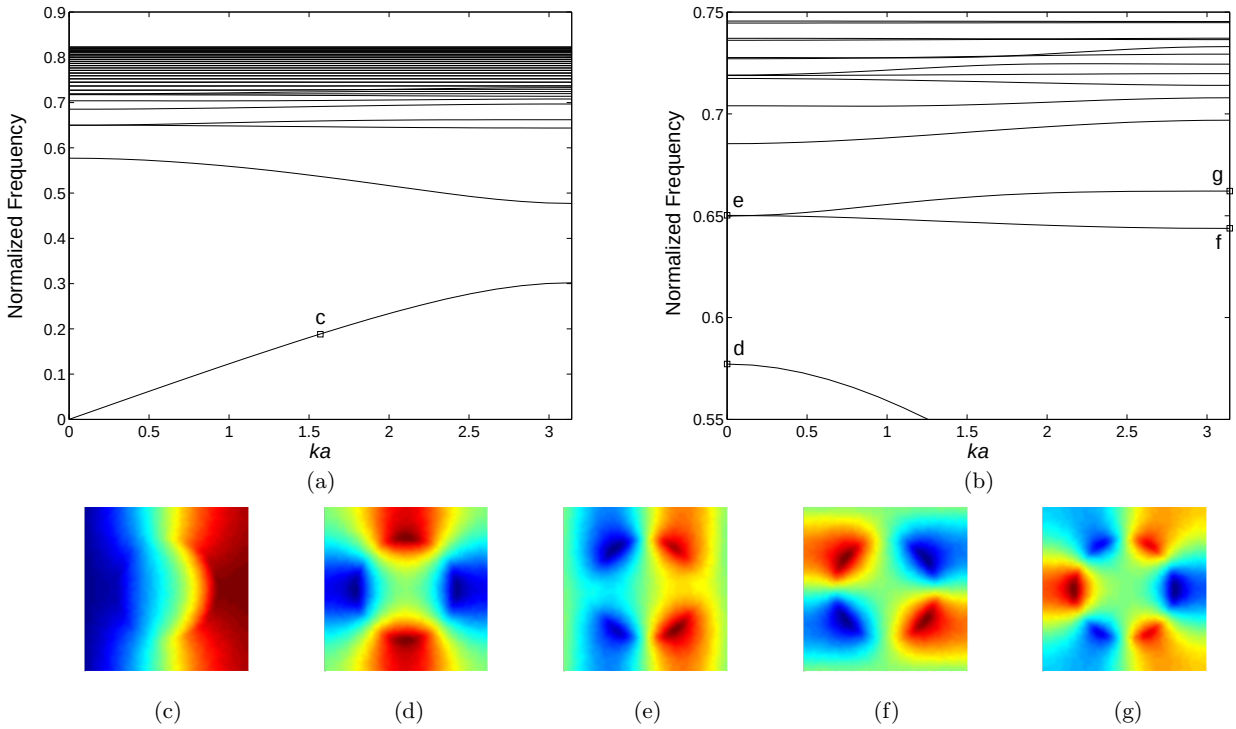

FIG. 3: (a) Photonic band diagram along the $\Gamma - X$ direction obtained with FEM for a square array of cylindrical rods, with $\omega_p^N = 1$ and $r/a = 0.3$. (b) A zoom-in view of the band diagram. (c - g) Plots of the real part of the z component of the magnetic field for some of the eigenmodes as indicated in (a) and (b).

the case of periodic structures, Bloch boundary conditions can be easily enforced on the opposite edges of the unit cell. All the other advantages of an unstructured-mesh approach, such as the possibility of adaptive mesh resolution, are retained.

We have successfully implemented a code by following the standard variational procedure [18]. Simulations with this finite-element implementation showed no fictitious surface modes. Similar to the finite-difference approach, the high-order surface modes still suffer from high numerical errors, and are shifted to higher frequencies from $\omega_p/\sqrt{2}$, as discussed in Sect. III B. The detailed descriptions on numerical studies based on this finite-element approach are presented in the following section, where we also compare our results against those in previously published works.

V. COMPARISON WITH OTHER RESULTS

In this section we present two band structures calculated with the FEM approach discussed in Sect. IV. The results are compared with those obtained with other numerical methods in the literature.

Figure 3(a) shows the band diagram along the Γ-X direction for a square array of metallic cylinders with normalized $\omega_p^N = 1$ and radius $r = 0.3a$, where a is the lattice parameter. The graph shows very good accordance with simulations results for the same structure obtained with a finite-difference time-domain (FDTD) technique[14], even for the flat bands around the surface-plasmon resonance frequency. The H_z field distributions for modes highlighted in Fig. 3(a) - (b) are represented in Figs. 3(c) - (g), which have the expected symmetries as analyzed in [14]. High-order modes accumulate in the frequency region $\omega_p/\sqrt{2} < \omega < \omega_p$, as discussed in Sect. III B. A notable feature of this FEM result compared to that obtained with FDM in Fig. 1(d) is that the surface modes in Fig. 3(a) terminates at a lower frequency (0.82). Such a difference between the two implementations always exists regardless of the structure and resolution used. This might be due to the fact that FEM has a better accuracy for representing the high-order SPP modes.

Figure 4 shows the complete photonic band diagram for a "diluted" silver cylinders in a square lattice, with radius $r = 15$ nm and lattice parameter $a = 130$ nm ($r/a \simeq 0.12$). Because of the small filling ratio ($f = 0.041$) the electromagnetic field is less affected by the presence of the cylinders and thus the modes can be approximately classified in two types: radiative free-space-like modes, which are strongly dispersive, and almost non-dispersive surface

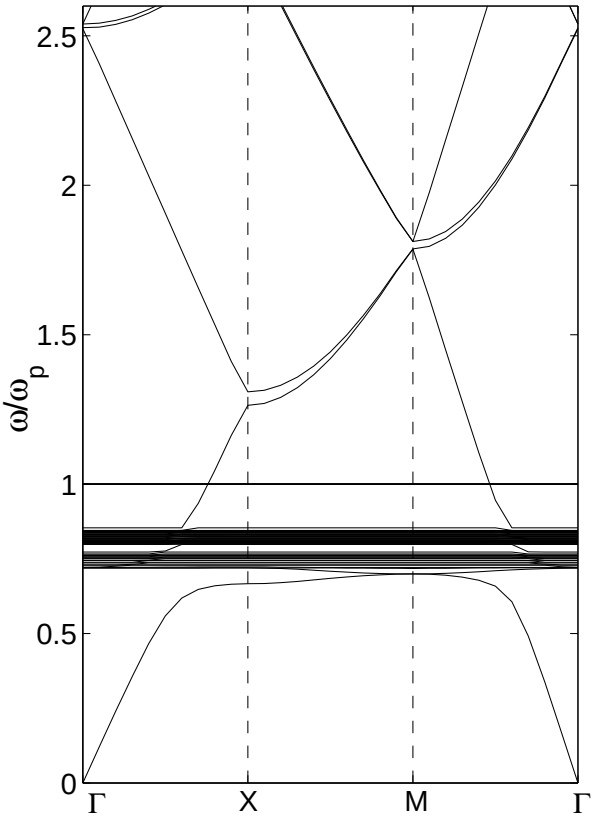

FIG. 4: Photonic band diagram for a square lattice of silver cylinders obtained with FEM. The lattice parameter is $a = 130$ nm and the cylinder radius is $r = 15$ nm. $\omega_p^N = 0.3963$.

modes. Indeed it is seen from the figure that the band structure is formed by the superposition of the free-space dispersion relation and the flat bands corresponding to surface modes in the frequency range $\omega_p/\sqrt{2} < \omega < \omega_p$. The band diagram shows reasonably good accordance to the result obtained with the finite-difference frequency-domain method [17]. The dispersion relations for the lowest order modes show the correct behavior. In particular, we note the expected degeneracy of two modes at the M point of the Brillouin zone for the lowest two bands. Such degeneracy is not observed in [17].

VI. CONCLUSION

In this paper, by expanding the standard Maxwell's eigenvalue problem with the introduction of an auxiliary mechanical field, we theoretically compute the modes in dispersive especially periodic material systems. We paid particular attention to materials with metal components, which support SPP resonances below the metals' plasmon resonance frequencies. With a FDM implementation the calculated photonic band structures exhibit two issues, which are mostly overlooked in the previous literature. When the rectangular finite-difference mesh does not correctly represent metal-dielectric interfaces, especially those with curvatures, fictitious modes are generated due to an averaged material layer created at the interfaces. These highly localized modes lead to non-dispersive flat bands in the photonic band structure, affecting our interpretation of the metamaterial's photonic properties. The other issue which we point out is that a numerical method can never accurately calculate all high-order SPP resonances in a plasmonic medium, even though analytically they should have limited frequency values around $\omega_p/\sqrt{2}$ for air-metal interfaces. This is due to the relatively poor mesh resolution for the high-order SPP modes. We also presented a FEM implementation of the formulation which is able to eliminate the fictitious mode problem owing to its use of an unstructured mesh. By using the FEM approach, we computed the photonic band diagrams for several structures of common interest and compared the results with those obtained with other numerical methods. The case studies confirm that the auxiliary-fields formulation, when implemented in the edge-element FEM approach, is both versatile and accurate. Together with its adaptive-meshing capability, the method can therefore serve as an efficient tool for analyzing band structures of a wide range of plasmonic metamaterials.

Acknowledgments: This work is supported by the Swedish Foundation for Strategic Research (SSF) and the Swedish Research Council (VR). A. Ferrario acknowleges the Erasmus Programme. The authors also would like to thank Prof. Shanhui Fan for his comments on the manuscript.

[1] J. D. Joannopoulos, S. G. Johnson, J. N. Winn, and R. D. Meade, *Photonic Crystals: Molding the Flow of Light* (Princeton University Press, 2008), 2nd ed., URL `http://ab-initio.mit.edu/book`.

[2] D. R. Smith, W. J. Padilla, D. C. Vier, S. C. Nemat-Nasser, and S. Schultz, Phys. Rev. Lett. **84**, 4184 (2000).

[3] J. Valentine, S. Zhang, T. Zentgraf, E. Ulin-Avila, D. A. Genov, G. Bartal, and X. Zhang, Nature **455**, 376 (2008).

[4] C. Kittel, *Introduction to Solid State Physics*, vol. 2010 (1995), ISBN 0-471-11181-3.

[5] W. H. Weber and G. W. Ford, Phys. Rev. B **70**, 125429 (2004).

[6] J. Hao, J. Wang, X. Liu, W. J. Padilla, L. Zhou, and M. Qiu, Applied Physics Letters **96**, 251104 (pages 3) (2010), URL http://link.aip.org/link/?APL/96/251104/1.

[7] M. Quinten, A. Leitner, J. R. Krenn, and F. R. Aussenegg, Opt. Lett. **23**, 1331 (1998), URL http://ol.osa.org/abstract.cfm?URI=ol-23-17-1331.

[8] M. Qiu and S. He, Journal of Applied Physics **87**, 8268 (2000), URL http://link.aip.org/link/?JAP/87/8268/1.

[9] A. Raman and S. Fan, Phys. Rev. Lett. **104**, 087401 (2010).

[10] A. V. Knyazev, SIAM J. Sci. Comput **23**, 517 (2000).

[11] S. Fan, P. R. Villeneuve, and J. D. Joannopoulos, Phys. Rev. B **54**, 11245 (1996).

[12] J. B. Pendry, L. Martin-Moreno, and F. J. Garcia-Vidal, Science **305**, 847 (2004), http://www.sciencemag.org/cgi/reprint/305/5685/847.pdf, URL http://www.sciencemag.org/cgi/content/abstract/305/5685/847.

[13] P. M. Bell, J. B. Pendry, L. M. Moreno, and A. J. Ward, Computer Physics Communications **85**, 306 (1995), ISSN 0010-4655, URL http://www.sciencedirect.com/science/article/B6TJ5-4031RDN-18/2/9ebdd0f0a7b84e2bc4c6f4d75aab325c.

[14] T. Ito and K. Sakoda, Phys. Rev. B **64**, 045117 (2001).

[15] D. A. Barnes, William L. and T. W. Ebbesen, Nature (2003).

[16] V. Kuzmiak, A. A. Maradudin, and F. Pincemin, Phys. Rev. B **50**, 16835 (1994).

[17] G. Veronis, R. W. Dutton, and S. Fan, Journal of Applied Physics **97**, 093104 (2005), URL http://link.aip.org/link/?JAP/97/093104/1.

[18] J. Jin, *The Finite Element Method in Electromagnetics* (Wiley, 2002), 2nd ed.